

AD/A-004 296

INVESTIGATION OF THE TURBULENT PROPERTIES OF THE WAKE BEHIND SELF-PROPELLED, AXISYMMETRIC BODIES

C. C. Chieng, et al

Virginia Polytechnic Institute and State University

Prepared for:

Office of Naval Research
Advanced Research Projects Agency

September 1974

DISTRIBUTED BY:

NTIS

National Technical Information Service
U. S. DEPARTMENT OF COMMERCE
5285 Port Royal Road, Springfield Va. 22151

September 1974

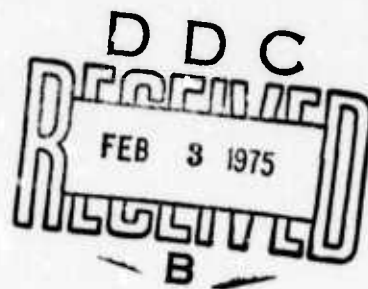
VPI-Aero-025

INVESTIGATION OF THE TURBULENT PROPERTIES OF THE
WAKE BEHIND SELF-PROPELLED, AXISYMMETRIC BODIES

by

C. C. Chieng, A. K. Jakubowski
and J. A. Schetz

Aerospace and Ocean Engineering Department



Approved for public release; distribution unlimited.

The views and conclusions contained in this document are those of the authors and should not be interpreted as necessarily representing the official policies, either expressed or implied, of the Defense Advanced Research Projects Agency or the U.S. Government.

AD/A004296

REPORT DOCUMENTATION PAGE		READ INSTRUCTIONS BEFORE COMPLETING FORM
1. REPORT NUMBER	2. GOVT ACCESSION NO.	3. RECIPIENT'S CATALOG NUMBER
4. TITLE (and Subtitle) INVESTIGATION OF THE TURBULENT PROPERTIES OF THE WAKE BEHIND SELF-PROPELLED, AXISYMMETRIC BODIES		5. TYPE OF REPORT & PERIOD COVERED Final Report
7. AUTHOR(s) C. C. Chieng, A. K. Jakubowski and J. A. Schetz		6. PERFORMING ORG. REPORT NUMBER VPI Aero-025
9. PERFORMING ORGANIZATION NAME AND ADDRESS Aerospace and Ocean Engineering Department Virginia Polytechnic Institute and State University Blacksburg, Virginia 24061		8. CONTRACT OR GRANT NUMBER(s) N00014-72-A-0136-0004
11. CONTROLLING OFFICE NAME AND ADDRESS Advanced Research Projects Agency Arlington, Virginia		10. PROGRAM ELEMENT, PROJECT, TASK AREA & WORK UNIT NUMBERS NR-062-481 ARPA Order No. 1910
14. MONITORING AGENCY NAME & ADDRESS (if different from Controlling Office) Office of Naval Research Arlington, Virginia 22217		12. REPORT DATE September, 1974
		13. NUMBER OF PAGES 134
		15. SECURITY CLASS. (of this report) Unclassified
		15a. DECLASSIFICATION/DOWNGRADING SCHEDULE
16. DISTRIBUTION STATEMENT (of this Report) Approved for public release; distribution unlimited		
17. DISTRIBUTION STATEMENT (of the abstract entered in Block 20, if different from Report) Reproduced by NATIONAL TECHNICAL INFORMATION SERVICE US Department of Commerce Springfield, VA. 22151		
18. SUPPLEMENTARY NOTES PRICES SUBJECT TO CHANGE		
19. KEY WORDS (Continue on reverse side if necessary and identify by block number) Turbulent wakes Self-propelled bodies Turbulence measurements		
20. ABSTRACT (Continue on reverse side if necessary and identify by block number) The turbulent wakes behind a streamlined drag body, a jet-propelled body and a propeller-driven body are studied experimentally in the VPI Stability Wind Tunnel at a nominal free stream velocity of 206 ft/sec. The turbulence properties investigated are axial, radial, and tangential turbulence intensities, and radial and tangential shear stresses. Data was taken at five axial stations downstream of the tail of the body: $X/D = 2, 5, 10, 20,$ and 40 . It is found that the propeller-driven body produces the largest wake		

throughout the axial distance covered by these tests. The jet-propelled body produces the middle sized wake compared to the other two models up to station $X/D = 20$; beyond this station, this wake becomes the smallest. In addition, the two self-propelled bodies produce initially higher radial and tangential turbulence intensities up to $X/D = 20$ and higher radial shear stress up to $X/D = 10$ than the drag body. The decay rates of these quantities for the self-propelled bodies are faster than that of the streamlined body; therefore, these values become lower than that of the drag body at the farther stations. The wake of the propeller driven body has generally the lowest axial turbulence intensity but, up to $X/D = 20$, it has the highest radial and tangential turbulence intensities and also, the highest Reynolds shear stresses near the tail of the body. Because this wake exhibits the fastest decay rate for all the turbulence properties measured it has the lowest values of these properties at the farthest station ($X/D = 40$).

The results are compared with the available data obtained by other researchers. Momentum and energy analyses are used to check the accuracy of the results and to obtain an insight into the flow structure and the mechanism of energy transformation.

TABLE OF CONTENTS

	<u>Page</u>
LIST OF FIGURES	v
LIST OF TABLES	viii
LIST OF SYMBOLS	ix
I. INTRODUCTION.	1
II. WIND TUNNEL AND MODELS	
Wind Tunnel	5
Models	5
Zero Momentum Control	7
III. INSTRUMENTATION	
Comparison of Turbulence Measurement Techniques	9
Hot-Wire Probes	9
Anemometer System	10
Auxiliary Equipment	11
Automatic Traverse	11
IV. EXPERIMENTAL PROCEDURE	
General	12
Axial Turbulence Intensity	12
Reynolds Stress and Turbulence Intensity in Radial and Tangential Directions	12
Calibration Curves	13
Model Alignment	13
Temperature Effects	14
Wire Contamination	15
V. DATA REDUCTION	
Axial Turbulence Intensity	16
Reynolds' Stress and Turbulence Intensity in the Radial and Tangential Directions	17
VI. RESULTS AND DISCUSSION	
Model I: Streamlined Drag Body	20
Model II: Jet-Propelled Body	23
Model III: Propeller-Driven Body	26

TABLE OF CONTENTS
(Cont.)

	<u>Page</u>
Comparison of the Results for Models I, II, and III . . .	29
Momentum Analysis	31
Energy Balance Analysis	35
VI. CONCLUSIONS	43
REFERENCES	47
APPENDIX A - SYMMETRY OF THE WAKE	49
APPENDIX B - TABULATED DATA	52
FIGURES.	68

LIST OF FIGURES

<u>Figure</u>	<u>Page</u>
1. VPI & SU Six Foot Wind Tunnel	68
2. Drag Body Model	69
3. Photograph of the Jet-Propelled Model (Model I)	70
4. Jet-Propelled Model	71
5. Photograph of the Propeller-Driven Model (Model III)	72
6. Single-normal Hot Wire (TSI-1210)	73
7. Single-yawed Hot Wire (TSI-1213)	73
8. Automatic Traverse	74
9. Angle of Attack Nomenclature	75
10. Calibration Curve - Velocity Sensitivity	76
11. Calibration Curve - Angular Sensitivity (S_{v+})	77
12. Calibration Curve - Angular Sensitivity (S_{v-})	78
13. Schematic Illustration of Evaluation of Axial Turbulence Intensity	79
14. Axial Turbulence Intensity Profiles for Model I	80
15. Radial Turbulence Intensity Profiles for Model I	81
16. Tangential Turbulence Intensity Profiles for Model I	82
17. Radial Shear Stress Profiles for Model I	83
18. Tangential Shear Stress Profiles for Model I	84
19a. Comparison of $(\overline{u'v'}/U_e^2)_{\max}$ for Model I and Chevray's Model	85
19b. Comparison of Peak Turbulence Intensities for Model I and Chevray's Model	85
20. Self-similarity Profile of Axial Turbulence Intensity for Model I	86

LIST OF FIGURES (Cont.)

<u>Figure</u>		<u>Page</u>
21.	Self-similarity Profile of Radial Shear Stress for Model I	87
22.	Axial Turbulence Intensity Profiles for Model II	88
23.	Radial Turbulence Intensity Profiles for Model II	89
24.	Tangential Turbulence Intensity Profiles for Model II	90
25.	Radial Shear Stress Profiles for Model II	91
26.	Tangential Shear Stress Profiles for Model II	92
27.	Comparison of the Results for Model II and Naudascher's Model	93
28.	Self-similarity Profile of Radial Shear Stress for Model II	94
29.	Self-similarity Profile of Radial Shear Stress for Model II	95
30.	Axial Turbulence Intensity Profiles for Model III	96
31.	Radial Turbulence Intensity Profiles for Model III	97
32.	Tangential Turbulence Intensity Profiles for Model III	98
33.	Radial Shear Stress Profiles for Model III	99
34.	Tangential Shear Stress Profiles for Model III	100
35.	Comparison of the Results for Model III and Gran's Model	101
36.	Comparison of $(\sqrt{u'^2}/U_e)_{\max}$ for Model I, II and III	102
37.	Comparison of $(\sqrt{v'^2}/U_e)_{\max}$ for Model I, II and III	103
38.	Comparison of $(\sqrt{w'^2}/U_e)_{\max}$ for Model I, II and III	103
39.	Comparison of $(\overline{u'v'}/U_e^2)_{\max}$ for Model I, II and III	104
40.	Comparison of $(\overline{u'w'}/U_e^2)_{\max}$ for Model I, II and III	105

LIST OF FIGURES (Cont.)

<u>Figure</u>		<u>Page</u>
41.	Wake Width	106
42.	Momentum Integrals (Model I)	107
43.	Momentum Integrals (Model II)	108
44.	Momentum Integrals (Model III)	109
45.	Energy Integrals (Model I)	110
46.	Energy Integrals (Model II)	111
47.	Energy Integrals (Model III)	112

LIST OF TABLES

<u>Table</u>	<u>Page</u>
I. Summary of Detailed Measurements of the Main Mixing Region in Turbulent Wakes	2
II. Representative Turbulent Quantities for Present Drag Body and for the Models Studied by Chevray and Burkeev	22
III. Representative Turbulent Quantities for the Present Injection Model (Model II) and for the Disk Model Studied by Naudascher	24
IV. Representative Turbulent Quantities for the Present Propeller-Driven Body (Model III) and for the Model Studied by Gran	27
V. Momentum Integrals: Model I	34
VI. Momentum Integrals: Model II	34
VII. Momentum Integrals: Model III	34
VIII. Energy Integrals: Model I	38
XI. Radial Velocity Estimates for Model II.	39
X. Energy Integrals: Model II	39
XI. Radial Velocity Estimates for Model III	42
XII. Energy Integrals: Model III	42

LIST OF SYMBOLS

AC	alternate current
C_D	drag coefficient
D	maximum diameter of body
\bar{D}	drag
DC	direct current
$\sqrt{e^2}$	RMS voltage output
E	DC voltage output
P_A	ambient pressure
P_O	total pressure
q	dynamic pressure
r	distance from the center of the wake
R	maximum radius of body
\bar{R}	the distance from the center of the wake to the location where the axial turbulence approaches free stream turbulence
R^*	r- distance corresponding to $\sqrt{u'^2} = 1/2(\sqrt{u'^2})_{\max}$
RMS	root mean square
S_u	velocity sensitivity
S_v	angular sensitivity
u	mean velocity in axial direction
U_e	mean velocity at the edge of the wake
$\sqrt{u'^2}$	axial turbulence
$u'v'$	radial Reynolds stress
$u'w'$	tangential shear stress
v	radial mean velocity

x

$\sqrt{v'^2}$

radial turbulence

$\sqrt{w'^2}$

tangential turbulence

X

longitudinal distance from tail of the body

ρ

density of air

I. INTRODUCTION

The turbulent wake behind a body in a fluid stream has been a frequent subject of experimental research because the development of such flow is not fully understood, and the turbulent properties (Reynolds shear stress and turbulence intensity) can only be calculated with the aid of semiempirical assumptions. Several experimental studies have been made at low and high speeds for both axisymmetric and planar geometries. Table I provides a summary of the more important work concerned with subsonic, turbulent wakes. Schlichting [1], Fage and Falker [2], Hall and Hislop [3], and Hill et al [4] measured the mean flow properties in the wake behind cylinders. Townsend [5] obtained some data on the turbulent properties of the cylinder wake. Cooper and Lutzky [6], and Carmody [7] used their disc models and measured both the mean flow and turbulent characteristics. More recently, wake studies have been made for an ellipsoid [8], a square cylinder [9], a spheroid [10], and a streamlined body [11].

During the past few years, turbulent wake flows with near-zero momentum defect have become a topic of increasing interest to researchers. Such flows occur behind many self-propelled vehicles and devices, including submarines, rockets, missiles, etc. An understanding of near-zero momentum (or momentumless) wake flows is necessary in order to approach several practical problems such as submarine detection, pollution dispersion from propulsion units, and wake dissipation. Only very few works dealing with the momentumless wakes of self-propelled bodies have been published, namely those by

TABLE I

Summary of Detailed Measurements of the Main Mixing Region in Turbulent Wakes

Author	Year	Ref. No.	Planar	Axisym- metric	Mean Flow	Turbulent Propor- ties	Momen- tumless	Configura- tion	Re _D
Schlichting	1930	1	x		x			circular cylinder	
Fage & Falck	1932	2	x		x			circular and len- ticular cylinder	1.69x10 ⁴
Hall & Hislop	1938	3		x	x			2:1 cylinder	7.3x10 ⁴
Townsend	1947-56	5	x		x	x		circular cylinder	
Reichardt	1951	15	x		x	x		circular cylinder	
Cooper & Lutzky	1955	6		x	x	x		thin disks	2x10 ³ -1.5x10 ⁴
Ilizarova & Pochkina	1962	16		x	x			6.67:1 body of revolution	
Hill, Schaub & Senoo	1963	4	x		x			bluff cylinder	
Carmody	1964	7		x	x	x		circular disk	7x10 ⁴
Bradbury	1965	17	x		x	x		wing with air jet	very small
Naudascher	1965	12		x	x	x	x	disk with air jet	5.4x10 ⁴
Ginevskii et al	1966	13		x	x	x	x	disk with air jet	
Buchinskaya & Pochina	1966	8		x	x			6:1 ellipsoid	(0.7-3.0)x10 ⁴
Gartshore	1967	9	x		x	x		square cylinder	
Chevray	1968	10		x	x	x		6:1 spheroid	4.6x10 ⁵
Bukreev et al	1972	11		x	x	x		streamlined body	10 ⁴
Hokenson, & Schetz	1972	18		x	x	x		sphere, ellipsoid	1.5x10 ⁵
Gran	1973	14		x	x	x	x	propeller-driven streamlined body	6x10 ⁴

Naudascher [12] Ginevskii et al [13], and Gran [14]. The configuration used by Naudascher and Ginevskii was a circular disk normal to an oncoming fluid stream. A high speed axial jet exhausted from the disc center was applied to enforce a zero net momentum wake. The wind tunnel velocity and Reynolds number in Naudascher's tests were 60 ft/sec, and 5.4×10^4 , respectively, and single and cross hot wires were used to measure the turbulence characteristics. The models used by Naudascher and Ginevskii could not give sufficiently good simulation of most of the cases of practical interest because their models were neither slender nor streamlined as is the usual case of self-propelled bodies. Gran studied the momentumless wake of a slender, propeller-driven body having a Rankine ovoid contour (Ref. 14). His measurements included both the mean flow and turbulent properties of the wake. The Reynolds number was relatively low ($Re_D \approx 6 \times 10^4$) and some difficulties with obtaining symmetrical wakes were encountered. As Table I demonstrates, most of the available information is related to unstreamlined bodies and was obtained under the conditions of low Reynolds numbers. Moreover, only two distinctly different momentumless cases have been investigated thus far.

In view of the scarcity and limitations of the available information on turbulent momentumless wakes it was felt that an experimental investigation was in order that would cover more practical, realistic wakes and possibly high Reynolds number range. The program was conceived to provide a systematic comparison of the turbulent wakes behind three separate, but related, slender bodies: (1) a streamlined

drag body (Model I), (2) jet-propelled body (Model II), and (3) propeller-driven body (Model III). All bodies had identical blunt noses and parallel middle-bodies and all had streamlined, sharp stern sections. The maximum diameter of each of the three models was six inches and the length-to-diameter ratio was 12 for Models I and III and 10.29 for Model II. The experiments were carried out in the VPI&SU Stability Wind Tunnel at a speed of 206 ft/sec. The Reynolds number based on diameter was 6.18×10^5 , i.e., an order of magnitude larger than for previous propeller-driven laboratory tests. For each model, the wake properties were measured at five stations ($X/D = 2, 5, 10, 20, \text{ and } 40$). Mean flow properties were determined with a pitot-static probe, a wedge type directional probe, and a Kiel probe. The following turbulence intensity and Reynolds shear stress values were obtained using single-normal and single-yawed hot-wire probes: $\sqrt{u'^2}$, $\sqrt{v'^2}$, $\sqrt{w'^2}$, $\overline{u'v'}$, and $\overline{u'w'}$. Momentum and energy balance analyses were carried out to verify the measurement accuracies and to obtain some insight into the mechanisms of momentum and energy transformation. In this work only the turbulence data are evaluated in detail and compared with the experimental results of Chevray, Naudascher and Gran. The mean flow data are presented and discussed in Ref. 19.

II. WIND TUNNEL AND MODELS

Wind Tunnel

The experiments were performed in the VPI stability wind tunnel (Fig. 1) at a free stream velocity corresponding to 9.5 in. H₂O dynamic pressure (about 206 ft/sec). The facility has a test section 6 ft x 6 ft, 23 ft long, and the cross section diverges slightly in the downstream direction. The mean velocity at the edge of the wake for the five stations varied less than 6%, and the free stream turbulence intensity outside the wake was measured to be less than 0.1%.

Models

Three separate, but related, models were tested:

(i) Model I - Streamlined Drag Body (Fig. 2)

Model I is a body of continuous slope variation with a parabolic nose made of wood, a 3 ft long section of parallel middle body made of aluminum tube, and a sharp wood tail. The total length of the body is 72 inches.

(ii) Model II - Jet Propelled Body (Figs.3 and 4)

Model II is propelled by a peripheral air-jet. It has a parabolic, plexiglass nose, a parallel aluminum middle section, and a stern which is formed of a plexiglass, tear drop shaped center body supported by four brass vanes spaced 90 degrees apart. Air was injected through a 1 inch peripheral slot at the end of the parallel middle section. The air for injection was supplied by four 150 psi compressors; a control valve was used to adjust the pressure of the injected air (about 112 psia) so that the wake was approximately momentumless.

The air was fed by a 3 in. diameter pipe outside of the test section and a supporting strut (made of seventeen 0.5-in. diameter pipes) into a plenum chamber inside the model. The plenum chamber was vented through a series of coarse and fine screens and exhausted through the slot. The screens were used to minimize nonuniformities and turbulence of the exhausted jet.

(iii) Model III - Propeller-Driven Body (Fig. 5)

The propeller-driven model was actually the drag body model modified so that a propeller and an electric motor could be installed. A model 2M145 Dayton, 1.2 hp, 10,000 rpm, AC/DC motor was fitted inside the model, and a 6-in. diameter propeller was connected to the motor using a 23-3/8 inch long shaft. The rpm was measured by a magnetic pick-up device. The signal produced by the magnetic pick-up was first amplified and then displayed on the oscilloscope screen. The propeller was a three-bladed, plastic model airplane propeller. In order to increase the pitch angle of the blades, they were heated and twisted by using a special tool made for this purpose. The experimental mean diameter pitch of the propeller was about 2.5, and the propeller was operated at an advance ratio $J = 2$ with an apparent efficiency 68%. The detailed performance of the propeller was reported by Swanson [19].

To obtain a momentumless wake, the propeller had to be driven at speeds between 12,000 and 12,500 rpm, i.e., at speeds higher than the motor was designed for. This resulted in some overloading of the motor. In order to prevent excessive temperature rise, the unit required an efficient water cooling system. The latter was provided by a system of coils made of 1/2 in. copper tubing and brazed to the motor

case. A thermocouple was hooked up to monitor the temperature of the motor, and this served to check whether the motor was functioning properly.

Model I and III were suspended from the ceiling of the wind tunnel by a thin strut, made of a 0.5 inch thick steel plate. There were 0.5 in. diameter pipes attached to the leading edge of the plate and they served as conduits for the electrical wiring and/or as channels for the cooling water (Model III). As mentioned above, a special strut made of pipes was used for Model II. The dimensions and the external geometry of the struts for Model I, II, and III were essentially the same.

Zero Momentum Control

For the second and third models, sufficient thrust was required to make the wake momentumless. Therefore, considerable testing was needed to determine the plenum pressure of the injected air (Model II) or the voltage and current of the power supply driving the propeller (Model III), corresponding to a near zero momentum wake. Several traverses in the left, right, and downward (opposite the strut) directions were made in order to find the wake momentum flux and the symmetry of the wake. The drag at a certain plenum pressure for Model II or a certain voltage (the current was maintained constant) for Model III was calculated by the expression:

$$D = 2\pi \int \rho u (u - U_e) r dr \quad (1)$$

The pressure or the voltage that gave the drag closest to zero was chosen as the standard throughout five stations. This primary testing was made at station $X/D = 5$ because of the low degree of swirl and the easily measured mean velocity profiles at this station.

In the second model, the air injection was supplied by four compressors (Ingersoll-Rand Co., 400 hp, 150 psi, 1600 cfm).

A pressure gauge was used to control the amount of the air flow. Care has been taken to keep the pressure constant because the regulator was not too efficient. In addition to the difficulty of controlling the pressure level, there were also other difficulties in controlling the temperature variation of the air jet.

As it was mentioned previously, the propeller of the third model was driven by a motor which had to be overloaded to render the wake momentumless. By using the magnetic pick-up rpm display on the oscilloscope, the speed of the propeller was adjusted by varying the DC voltage supplied to the motor. Usually the propeller ran smoothly and did not need any adjustment; however, occasionally it would run erratically, most probably due to overloading. In addition, it has been found that the DC current was much more suitable than AC current for driving the motor, the reason being that the small fluctuations in rotational speed which were unavoidable during the AC operation seemed to have a strong influence on the turbulence spectrum produced by the propeller.

III. INSTRUMENTATION

Comparison of Turbulence Measurement Techniques

Basically there are three broad classes of techniques for the measurement of a fluctuating field [20] - a) the use of a localized sensing probe such as a hot wire b) the use of tracers and c) the use of some type of integrated measurement, usually optical. The integrated methods cannot be used for many applications because they always rely heavily on some additional assumptions about the statistical nature of the field. The tracer techniques are very tedious and time consuming because they require many samples. For example, a turbulence record of five seconds in flow (with a mean velocity 30 m/sec and a microscale of turbulence of 0.6 centimeters) is equivalent to a total of 25,000 samples. Therefore, such technique is not convenient for a routine work. As for the localized probe techniques, there are dark current discharge anemometers, glow discharge anemometers, streaming potential probes used as anemometers, fluctuating total pressure probes and many others besides hot wire anemometers. The hot-wire anemometer is still considered as generally more suitable than any of the other challengers.

Hot-Wire Probes

It was mentioned earlier that single- and crossed wires were used by other researchers. The crossed wire can measure the turbulence in two perpendicular directions and the directional correlation (Reynolds stress) at the same time by connecting the anemometer with a correlator and an RMS meter [21]. This procedure sounds handy and attractive,

but the effect of asymmetry is unavoidable in the crossed-wire probe and double sets of readings have to be taken by rotating the instrument 180° about the axis of flow direction between different sets. In addition to this, the data reduction which depends on the assumption that the turbulent field can be superposed linearly is not true in general [12]. In this work, only a single channel of the anemometer was available. Therefore, a single-normal probe was used to measure the longitudinal turbulence intensity, and a single 45° yawed probe was used to measure the Reynolds stress in the radial and tangential directions, and radial and tangential turbulence intensity, by rotating the wire 180° about the axis of flow direction. The probes used were single normal (TSI-1210) and single yawed probes (TSI-1213) shown in Figs. 6 and 7. The diameter and length of the sensor were 0.00015 in. and 0.05 in., respectively. The length of the whole probe (Figs. 6 and 7) was 1.875 in. The probes were made of platinum plated tungsten wires having the following characteristics: 1) a high temperature coefficient of resistance 2) an electrical resistance such that it can be easily heated with an electrical current at practical current and voltage levels.

Anemometer System

Turbulence measurement data were obtained by using a TSI (Thermo-System, Inc.) constant temperature anemometer (Model 1050), a DC Doric Integrating Voltmeter (Model DS-100), and a DISA type 55D35 RMS voltmeter. The anemometer has very low noise (less than 0.007% equivalent turbulent intensity), high DC and AC gain (35,000) with

gain curve shaping control, high power output (1.5 amps), and the frequency response is above 500 kHz. The output of the anemometer was not linearized because the mean velocity varied within a relatively small range. The RMS voltmeter had a signals response range of 1 hertz to 400 kilohertz, integrator time constants from 0.1 to 30 seconds, and an accuracy of 0.5% of the full scale deflection.

Auxiliary Equipment

In addition to the anemometer data, mean flow flow information [19] was obtained by using a pitot-static tube (United Sensor USC-A-155) and directional (United Sensor B-1111, w-187) and Kiel probes.[19] The two latter probes were used to measure the inclination angle of the flow and the total pressure, repectively.

Automatic Traverse

All probes were mounted on a traverse especially modified for this investigation (Fig. 8). The probe could be moved upward and downward vertically; left and right horizontally. The position of each probe was controlled by means of variable speed electrical DC motors and was indicated on a x-y recorder. The recorder was calibrated in such a way that one inch movement of the probe in either direction gave an indication of two inches on the x-y recording chart.

IV EXPERIMENTAL PROCEDURE

General

In this work, the main concern is placed on the turbulence characteristics - including axial (first subsection), radial, and tangential turbulence intensities, and tangential and radial shear stress (second subsection). All the mean flow data are given by Swanson [19].

Before making the turbulence measurements at a given station, the center of the wake was determined by using the pitot-static tube and making several slow dynamic pressure scans of the wake in both the horizontal and vertical directions. The wake center was identified as a location of either the maximum or minimum axial velocity.

Axial Turbulence Intensity

In this experiment, the normal hot wire was used to measure the turbulence in the longitudinal direction. The procedure for performing this part of the measurements consisted of adjusting the hot wire perpendicular to the flow direction and taking data at 0.25 inch increments in the radial direction.

Reynolds Stress and Turbulence Intensity in Radial and Tangential Directions

A yawed hot wire was used to measure the shear stresses and turbulence intensity in the radial and tangential directions. The procedure for performing this part of the measurements consisted of adjusting the hot-wire in the vertical radial plane of the flow field

(through the centerline), taking data, then turning the probe 180° about the axis of the probe, and taking data again. This was done at 0.25 inch intervals across the entire wake. Next, the hot-wire was adjusted in the horizontal radial plane of the flow field and the above procedure of taking data was repeated to obtain shear stress and turbulence intensity in the tangential direction.

Calibration Curves

The calibration of the hot-wire probes was made with the aid of a photographic camera tripod mechanism mounted in the wind tunnel test section. The tripod was modified to include a large protractor for defining the inclination of the probe. The velocity sensitivity was determined by taking the DC output at several tunnel q 's and then plotting the DC signal versus air velocity. The angular sensitivity of the yawed-wire probes was obtained by varying both the freestream velocity and the angle of attack of the probe. The angle of attack was varied in the range from -6° to $+6^\circ$ in increments of 2° . A sketch explaining nomenclature is shown in Fig. 9. These calibrations were done numerous times in order to check reproducibility and to obtain calibration curves for a complete range of temperature.

Model Alignment

Before the experiments were started, an attempt was made to align the model with the wind-tunnel stream. In these experiments, all three models were aligned with the same orientation which was assumed to be parallel to the direction of flow within an angle not

exceeding 2 minutes. The reason for the great care needed to attain an angle of attack as close to zero as possible is explained by Buchinskaya [8]. She studied the structure of a vortex wake behind a thin body of revolution at different angles of attack and found that the structure of the vortex wake behind a slender body varied greatly with very small changes in the angle of attack. For our experiments, exact symmetry of the wake was very difficult to achieve. For Model II, the four brass interior vanes had some influence as well, so they were adjusted to have minimum effect. In addition, an imperfect geometry of the tear-drop shape center body could be the most responsible factor for a slight asymmetry of the wake produced by Model II.

Temperature Effects

Since the hot-wire output may be very sensitive to temperature, a particular care in calibration and testing must be exercised. From the calibration curves (Fig. 10-12), it is seen that 1°F temperature difference in the wind tunnel caused an approximate 0.01 volt difference in anemometer DC output which yielded a 4 ft/sec difference in mean velocity determination. For most of the experiments, the free stream temperature variation remained within 5°F. This 5°F temperature difference implies as much as a 20 ft/sec difference in the mean velocity. For this reason, the mean velocity obtained by the hot wire was not used directly, and the edge mean velocity obtained from the pitot-static tube was used to normalize the turbulence readings. The hot wires were used only for defining turbulent properties. This is a standard procedure for hot wire experiments. It is noticed that the

RMS output does not vary much for small temperature difference (e.g., 5°F).

Since Corrsin and Uberoi [24] found that the initial jet temperature had a very great influence on the temperature and velocity variation of jet mixing problems, one must exercise great care in experiments of the type with Model II here. Any temperature variation would change the density of the air and hence the speed of the jet. Therefore, not only the hot wire output readings could be influenced, but the speed of the jet would also vary, so that there was a possibility of having some deviation in the mean velocity and turbulence.

Wire Contamination

In the tests on Model II, there was some oil coming from the compressors, and this might possibly contaminate the air stream and the hot wire. Since the hot wire is sensitive to contamination, the data obtained did not show as good reproducibility (0 - 2% difference for $X/D = 2, 5, 10$; 10 - 17% difference for $X/D = 20, 40$) as for Models I and III.

V. DATA REDUCTION

The method of obtaining the axial turbulence intensity will be described in the first subsection; methods for obtaining the Reynolds stresses and the radial, and tangential turbulence intensities will be described in the second subsection. Basic to turbulence data evaluation were two assumptions: a) the flows approach those of constant temperature and density and b) the hot wires were operated ideally by the electronic circuits, so that problem of frequency response was eliminated.

Axial Turbulence Intensity

The method used for defining the axial turbulence intensity is graphical analysis [22]. It is based on the following assumptions: 1) the positive and negative directions are the same for velocity and voltage because the hot wire anemometer is unable to distinguish the direction of the flow, 2) RMS is distributed symmetrically about DC. At first, the calibration curve has to be set up, so that the velocity is known by the corresponding voltage output (See Fig. 13). The DC output gives the average velocity at the "working" point, and the RMS output gives the velocity fluctuation around the working point. The longitudinal turbulence, $\sqrt{u'^2} = v_u - v_B$, where v_u and v_B are the corresponding velocities at voltage DC + 1/2 RMS and DC - 1/2 RMS, respectively.

Reynolds Stresses and Turbulence Intensity in the Radial and Tangential Directions

i) Radial Shear Stress and Turbulence Intensity

To calculate Reynolds stress and turbulence intensities in another than axial direction, we use the following relations:

$$e^{-2} = \left(\frac{\partial E}{\partial u}\right)^2 \overline{u'^2} + 2 \left(\frac{\partial E}{\partial u}\right) \left(\frac{1}{u} \frac{\partial E}{\partial \psi}\right) \overline{u'v'} + \left(\frac{1}{u} \frac{\partial E}{\partial \psi}\right)^2 \overline{v'^2}$$

$$e^{-2} = S_u^2 \overline{u'^2} + 2S_u S_v \overline{u'v'} + S_v^2 \overline{v'^2} \quad (2)$$

so

$$e_{+}^{-2} = S_{u+}^2 \overline{u'^2} + 2 S_{u+} S_{v+} \overline{u'v'} + S_{v+}^2 \overline{v'^2} \quad (3)$$

$$e_{-}^{-2} = S_{u-}^2 \overline{u'^2} + 2S_{u-} S_{v-} \overline{u'v'} + S_{v-}^2 \overline{v'^2} \quad (4)$$

where $S_u = \partial E / \partial U$ (velocity sensitivity), $S_v = 1/v \partial E / \partial \psi$ (angular sensitivity) obtained from calibration curves (see Experimental Procedures) with respect to velocity and angle.

+ subscripts represent the value obtained for the slanted probe while the long prong is on the top (wire inclined +45°)

- subscripts represent the value obtained for the slanted probe while the short prong is on the top (wire inclined -45°)

The two unknowns ($\sqrt{\overline{v'^2}}$, $\overline{u'v'}$) can be obtained from the equations 3 and 4.

ii) The Tangential Shear Stress and the Turbulence Intensity

These two quantities are obtained by the same method as above except that the + and - subscripts represent the values obtained with

the long prong of the probe at the left and right side facing upstream, respectively, and v in the equations is replaced by w .

VI. RESULTS AND DISCUSSION

As described in the foregoing, three different models were investigated. The first model is a streamlined body, and the flow field behind this body is simpler than the other two. The flow has lower turbulence intensity and Reynolds stress, and the wake is produced by the body only. The wake produced by the second model is a mixing of the air jet and the wake. This involves the characteristics of the air jet and the geometry itself. The wake produced by the third model is more complicated than those of the other two, because the propeller produces velocities in both the tangential and radial directions, and the problem involves the turbulence characteristics of both the propeller and the body wake.

Since all these three models are essentially axisymmetric, the wakes induced should be also axisymmetric provided that the alignment and the construction are perfect. Several mean flow measurements were made to test the symmetry of the wakes and it was found that, in general, the mean flow symmetry was satisfactory [19]. In addition, turbulence measurements in the axial direction at various stations were made to assess the symmetry of the turbulence distribution in the wake of Models I and II (see Appendix A). In the case of Model I, the "turbulence symmetry" was judged satisfactory (cf. Table A-1). For the case of Model II, the wake was fairly close to symmetry except for the outer portion of the wake ($r = 2-3$ in.) at near stations ($X/D = 2$ and 5). Asymmetry at the locations just mentioned might be caused by slight misalignment and asymmetry of the four vanes in the peripheral

slot of Model II. The downward direction (opposite to the strut) was selected for detailed measurements and was taken as representative of other directions.

In this work, the turbulence intensities and Reynolds stresses are the main subject of interest and will be discussed separately for the different models. All the mean flow data are presented and discussed in Ref. 19.

Model I: Streamlined Drag Body

Model I is the only one of the three models, which does not produce a momentumless wake, and as such it serves as a basis for comparison of the self-propelled cases. The turbulence intensity profiles of the wake in the three perpendicular directions are plotted in Figs. 14, 15, and 16. The Reynolds stress profiles are plotted in Figs. 17 and 18.* From these plots, it is apparent that the wake spreads as it moves downstream. The axial turbulence intensity profiles (Fig. 14) show that the peak value increases over a distance ranging from 12 inches ($X/D = 2$) behind the body tail to 60 inches ($X/D = 10$) and then decreases as it moves further downstream. The other two directional turbulence intensities exhibit similar trends; the peak turbulence intensity increases along a distance extending from 12 inches behind the body tail to 30 inches ($X/D = 6$) and then drops as the wake moves further downstream. The major reason for such a behavior lies in the convergence of the wake near the body tail. By comparing the three figures (14, 15 and 16), it can be seen that the longitudinal turbulence intensities are higher than those in the other two directions.

* All data plotted are corrected for background turbulence.

The radial Reynolds stress is twice as high as that in the tangential direction (Fig. 18). The presence of the tangential shear stress may indicate some asymmetry of the wake due to an imperfect alignment. The peak radial Reynolds stress $(\overline{u'v'}/u_e^2)_{\max}$ increases up to station $X/D = 5$ and then decreases downstream.

Now, the results will be compared with those obtained by Chevray and Bukreev [10, 11]. When comparing, one has to realize that the body used by Chevray is somewhat similar to this model (Model I), the main difference being that the tail of this model is sharp while Chevray's is blunt and the ratio of the length to the maximum diameter of his model is 6:1, while for the Model I this ratio is 12:1. The body studied by Bukreev is sharp tailed. Table II and Fig. 19 present the representative values obtained in the three experiments. It can be seen that the results being compared are close to each other in magnitude, and that the longitudinal turbulence intensities are higher than those in the other two directions. In the results obtained by Chevray, the peak turbulence intensities in the radial direction and the peak Reynolds stresses decrease starting from $X/D = 9$. Such phenomena occur due to a complex vortex system formed in the boundary layer of the body, and converging with the flow direction in the near wake [13]. The results obtained in this work are somewhat different which can be explained by the fact that the tail of the two models are different in shape, so that the vortex systems converge differently.

The similarity profile for the axial turbulence intensity is shown in Fig. 20. This profile is formed by normalizing the

TABLE II

Representative Turbulent Quantities for the Present Drag Body (Model I) and for the Models Studied by Chevray [10] and Burkeev [11]

x/D	$\left(\frac{\sqrt{u'^2}}{U_e}\right)_{\max}$		$\left(\frac{\sqrt{v'^2}}{U_e}\right)_{\max}$		$\left(\frac{\sqrt{w'^2}}{U_e}\right)_{\max}$		$\left(\frac{u'v'}{U_e^2}\right)_{\max}$	
	Burkeev	Present	Burkeev	Present	Burkeev	Present	Burkeev	Present
2	0.0490	0.0405	0.0308	0.0275	0.0342	0.0320	0.00069	0.00061
3	0.0500	0.0462	0.0280	0.0280	0.0325	0.0325	0.00088	0.00705
5	0.0500	0.0540	0.0310	0.0308	0.0370	0.0368	0.00079	
6	0.0480	0.0450	0.033	0.0365	0.0300	0.0300	0.00075	
8	0.0550	0.0285	0.0320	0.0300	0.0340	0.0340	0.00055	0.00076
10	0.0420	0.0317	0.0299	0.0299	0.0322	0.0322	0.00055	0.00055
12		0.0285	0.0219	0.0245	0.0290	0.0290	0.00050	0.00035
15		0.0190	0.0100	0.0121				
18	0.0340	0.0445	0.0210	0.0210				
20	0.0230	0.0230						

turbulence intensity and the radial distance with the values of $(\sqrt{u'^2})_{\max}$ and R^* , respectively, where $(\sqrt{u'^2})_{\max}$ is the maximum axial turbulence and R^* is the r-distance corresponding to $\sqrt{u'^2} = \frac{1}{2}(\sqrt{u'^2})_{\max}$. The different distributions form a unique curve in the outside portion of the wake; the scattered data at the center of the wake confirm that the turbulence fluctuations are not self-preserved. The similarity profiles for radial shear stress are shown in Fig. 21. The similarity profile is formed by the scaling factor $(\overline{u'v'})_{\max}$ and R^* . The different distributions of these profiles form a unique curve in both the inner and the outer regions of the wake with some scatter. All these results are similar to the results of Chevray.

Model II : Jet-Propelled Body

The turbulence intensity profiles are plotted in Figs. 22, 23, and 24. These figures show that the profiles are very different from those for the streamlined body both in their distributions and their magnitudes for all representative quantities. The longitudinal turbulence intensity profiles have some peculiar phenomenon near the center of the wake and there are dips near $r/R = 0.25$ at the stations close to the tail ($X/D = 2$ and $X/L = 5$). The radial and tangential turbulence intensity profiles are not smooth in the inner portion of the wake. The reason for this may be related to the character of the air jet. The jet passed screens, converged along the tear-drop shaped center body and then mixed together - which is a complex system, located in the inner portion of the wake. The outer portion of the wake is produced primarily by the main body and is smoother. The

TABLE III
 Representative Turbulent Quantities for the Present Injection Model (Model II) and for Disk Model Studied by Naudascher [12]

X/D	$\left(\frac{\sqrt{u'^2}}{U_e}\right)_{\max}$		$\left(\frac{\sqrt{v'^2}}{U_e}\right)_{\max}$		$\left(\frac{\sqrt{w'^2}}{U_e}\right)_{\max}$		$\left(\frac{u'v'}{U_e}\right)_{\max}$	
	Present	Naudascher	Present	Naudascher	Present	Naudascher	Present	Naudascher
2	0.095*		0.0671*		0.0600*		0.0023	
4		0.246		0.198		0.193		0.0162
5	0.072	0.163	0.0428	0.127	0.0400	0.124	0.0018	0.00656
7		0.110		0.0993		0.0988		0.00307
10	0.0615	0.0745		0.070		0.0335	0.00064	0.00024
15		0.0535		0.0452		0.0446		0.00051
20	0.0539	0.0425	0.0275	0.0355	0.0275	0.0335	0.00064	0.00024
25		0.0330		0.0310		0.0280		0.00014
35		0.0239		0.0232		0.0217		0.000065
40	0.0335		0.0240		0.0221		0.00020	
50		0.170		0.0162		0.0151		

* Second peak of the profile.

Reynolds stress profiles (Figs. 25 and 26) show that there is a very big dip after the first peak but no such dip appears in the streamlined body data. Note that the sign of the shear stress is opposite to that of the streamlined body. It is obvious that installing the air jet can change the whole flow field.

For Model II, the wake is wider than that of the streamlined drag body. The peak turbulence intensities in the longitudinal, radial and tangential directions, and the peak Reynolds stress decrease, as the wake moves downstream. The turbulence intensity in the longitudinal direction is higher than that in either of the other two directions (see Figs. 22-24).

Since there are no published experimental data on a slender, streamlined body with momentumless wake available, the work used for comparison here is a study of a circular disk with air injection, which is neither slender nor streamlined (Naudascher, Ref. 12). Table III and Fig. 27 show that the peak turbulence intensity and Reynolds stress for Model II are lower than for Naudascher's models. The longitudinal turbulence intensities are higher than the radial and tangential ones, but the peak radial and tangential turbulence intensities measured here are close to the peak axial turbulence intensities for Naudascher's model. The decay rates of the turbulence intensity of Model II are much slower than in Naudascher's experiments. The distribution of longitudinal turbulence intensities and the shape of Reynolds stress profiles are sufficiently similar to each other. It is noticed that the dip is higher than the peak in the Reynolds stress profiles for this model but the reverse is true for Naudascher's model. The differences may be due to

the basic differences in the model geometries and, hence, wakes produced by Model II and Naudascher's model.

The self-similarity profiles for axial turbulence intensities and radial shear stress are shown in Figs. 28 and 29. The axial turbulence intensity distributions can form a definite curve in the outside portion of the wake although there is some scatter at the station $X/D = 40$. The reason for the scatter at this station is that its turbulence intensity is very low as compared with that at other stations, and the experimental error is amplified by the factor $(\sqrt{u'^2})_{\max}$. The scatter in the inner portion of the wake is caused by the characteristics of the air jet. It is seen that the radial shear stress distribution does not form a good definite curve in the outside portion of the wake. It seems as if they form two curves - one for stations $X/D = 2$ and 5, and the other for $X/D = 10, 20,$ and 40. The reason for the observed irregularities may be that the air jet has a larger influence over near stations than the free stream; at the farther stations, the air jet and the free stream flow mix more and both are important to the outside portion of the wake.

Model III: Propeller-Driven Body

The turbulence intensity profiles in the longitudinal, radial and tangential directions are plotted in Figs. 30-32. The radius of the wake is much wider than that for the other two models. The longitudinal turbulence intensity profiles have more than one peak at stations $X/D = 2, 5,$ and 10. The radial and tangential turbulence

TABLE IV
 Representative Turbulent Quantities for the Present Propeller-Driven Body (Model III) and for
 the Model Studied by Gran [14]

X/D	$\left(\frac{\sqrt{u'^2}}{U_e}\right)_{\max}$		$\left(\frac{u'v'}{U_e}\right)_{\max}$	
	Present	Gran	Present	Gran
2	0.0648*		0.00243	
4		0.086		
5	0.0483	0.072	0.0017	
6		0.066		0.00205
8		0.058		0.00129
10	0.0357	0.045	0.00085	0.00065
15		0.032		0.0003
20	0.0173		0.00012	
40	0.0100	0.024	0.00002	

* First peak of the profile.

intensity profiles each have a second peak after the first one and the second peaks are lower at downstream stations. Moreover, the height of the first peak decreases as the wake moves downstream. Another significant point to be noticed is that the turbulence intensity profiles are quite flat and widely spread after $X/D = 10$. The Reynolds stress profiles (Fig. 33) in the radial direction each have a peak and then dip, opposite to that observed for the second model (see Figs. 25 and 33). The magnitude of the peak is bigger than that of the dip but all of them decay very rapidly downstream after the station $X/D = 5$. Downstream of $X/D = 10$, there is no dip, the profiles become very flat and the values are very low as compared with those at stations near the body. Reynolds stress values in the tangential direction (Fig. 34) are bigger than for the other two models. We observed an even higher tangential shear stress than that in the radial direction at the stations near the tail of the body. This is due to the presence of more swirling and non-negligible tangential velocity in the flowfield due to the propeller. In addition, the decay rates of peak turbulence intensities and Reynolds stress for this model are much higher than the corresponding values for the other two models (Figs. 36-40), and the longitudinal turbulence intensities (Figs. 36-38, and 31-33) are lower than those in the other two directions for this model, while for the other two models the longitudinal turbulence intensity is higher than that in the other two directions. It is noted that there is some peculiar behavior (Fig. 34) near the center of the wake, possibly due to the effect of the tail of the body and

the hub of the propeller. It can be concluded that all the turbulence characteristics of the wake of Model III are very different from the wake turbulence characteristics of Models I and II both in magnitude and profile distributions of turbulence intensity and shear stress.

The turbulence data for Model III will be compared with the results obtained by Gran [14]. Only $(\sqrt{u'^2}/U_e)_{\max}$ and $(\overline{u'v'}/U_e^2)_{\max}$ are listed in Table IV and plotted in Fig. 35, because Gran measured only axial turbulence intensity and radial shear stress. This comparison shows that, in terms of the order of magnitude of the turbulence intensity and the radial shear stress, our experimental results are generally in rough agreement with those of Gran. Here the axial turbulence intensity of Model III exhibits more than one peak at the stations near the body ($X/D = 2$ and 5), and the corresponding profiles are very flat at the stations further downstream ($X/D = 10, 20,$ and 40). The axial turbulence intensity profiles obtained by Gran did not have a second peak but they did have some small ripples. It is seen from Fig. 35 that the peak radial shear stresses for the two models are close in order of magnitude but the axial turbulence intensity for Gran's model is higher than that for Model III although the decay rates are similar. The differences shown might be caused by the different characteristics and performance of the propellers.

Comparison of the Results for Models I, II, and III

When the maximum values of axial turbulence intensities are compared for the three models (Fig. 36), it can be seen that the air injection model has the highest value. The propeller-driven model

produces higher axial turbulence intensity than the drag body at the nearest station, but the axial turbulence intensity for Model III decreases very fast after station $X/D = 10$ while this quantity for Model I increases a little up to station $X/D = 10$ and then decreases at a similar rate as for Model II. Therefore, the propeller-driven body generates the lowest axial turbulence intensity after station $X/D = 10$.

From Figs. 37 and 38, it is seen that the propeller-driven body produces the highest radial and tangential turbulence intensities and their rate of decrease is faster than for the drag body. Consequently, the turbulence intensities in radial and tangential directions are close for these two models at stations $X/D = 20$ and 40 . The radial and tangential turbulence intensities for Model II at near stations ($X/D = 2$ and 5) have values in between those for two other two models but they decrease slowly.

From Fig. 39, it is seen that for the self-propelled bodies the initial magnitude of the radial shear stress is higher than for the drag body. For the propeller-driven body the radial shear stress decreases very fast, so that, at downstream locations, it becomes even lower than that for the drag body. The radial shear stress for the air-injection body decreases somewhat faster than that for Model I, but is still higher than that for Model I up to the station $X/D = 40$.

From Fig. 40, it can be seen that tangential shear stresses in the wakes of Models I and II are low but not negligible. This may

be related to some degree of non-uniformity and imperfect symmetry in the flow field behind these models. The decay rates of the tangential shear stresses for the three models are similar at stations downstream of $X/D = 10$.

In Fig. 41, \bar{R} is the distance from the center of the wake to the location where the axial turbulence approaches free stream turbulence. This figure shows that the propeller-driven body produces the widest wake throughout the five measurement stations, and the width of the wake of the streamlined drag body is the smallest one except for the locations $X/D > 20$.

The Figs. 36 through 40 suggest that air injection increases the turbulence intensities in all directions; it also increases the radial and tangential shear stresses. The propeller decreases the axial turbulence intensity, but increases the turbulence intensity in the radial and tangential directions and the tangential shear stress.

Momentum Analysis

In order to document the wake conditions and obtain an insight into the flow structure and the mechanism of momentum and energy transformation, momentum and energy balance analyses of the data are presented. The momentum analysis can be used as a measure to determine whether the experimental wake is the desired wake for the models tested. A useful form of the momentum equation is derived by integrating the first equations of Reynolds over a cylindrical control surface and

neglecting the viscous stress $2\pi r \mu du/dx$ under the assumptions of high Reynolds numbers. The resulting momentum equation for the axial direction is reduced by Rouse [25] to:

$$-\frac{C_D}{2} = 2 \left[\int_0^r \left[\left(\frac{u}{U_e} \right)^2 - 1 \right] \frac{r}{R} d \frac{r}{R} \right] + 2 \int_0^r \left(1 - \frac{u}{U_e} \right) \frac{r}{R} d \frac{r}{R} \\ + \int_0^r \frac{\bar{p}_A}{P_0} \frac{r}{R} d \frac{r}{R} + 2 \int_0^r \frac{\overline{u'^2}}{U_e^2} \frac{r}{R} d \frac{r}{R} \quad (5)$$

The first term on the right side of Eq. (5) represents the difference in the mean momentum flux between the final and initial sections; the second term represents the net flux of momentum through the periphery of the region under consideration and the third term represents the effect of the pressure difference between two sections; the last term represents the difference in the turbulence momentum flux.

We define $U_d = U_e - u$; then Eq. (5) becomes

$$-\frac{C_D}{2} = 2 \int \left(\frac{U_d}{U_e} \right)^2 \frac{r}{R} d \frac{r}{R} - 2 \int \frac{U_d}{U_e} \frac{r}{R} d \frac{r}{R} + \int \frac{\bar{p}_A}{P_0} \frac{r}{R} d \frac{r}{R} \\ + \int \frac{\overline{u'^2}}{U_e^2} \frac{r}{R} d \frac{r}{R} \quad (6)$$

for convenience, we introduce

$$I_n = \int \left(\frac{U_d}{U_e} \right)^n \frac{r}{R} d \frac{r}{R}; \quad n = 1, 2 \\ I_p = \int \frac{\bar{p}_A}{P_0} \frac{r}{R} d \frac{r}{R} \\ I_t = \int \frac{\overline{u'^2}}{U_e^2} \frac{r}{R} d \frac{r}{R}$$

Hence

$$-C_D = 4 (I_2 - I_1 + I_t) + 2I_p$$

The values of integrals are tabulated in Tables V-VII and plotted in Figs. 42-44.

i) Model I: Streamlined Drag Body

The results are shown in Table V and Fig. 42. Theoretically, the drag coefficient at various stations should be exactly equal, but in these experiments there are deviations up to 15% from the final drag coefficient, $C_D = 0.104$. However, it can be seen that the drag approaches a constant value for the downstream stations. The non-negligible tangential force may be, at least in part, responsible for discrepancies at the near stations.

ii) Model II: Jet-Propelled Body

The results are shown in Table VI and Fig. 43. For a zero momentum wake, the drag should be zero. At stations other than $X/D = 2$, the drag coefficient is very close to zero while at station $X/D = 2$ it has a value of 0.005. Such discrepancy may be related to a complicated flow-field near the tail of the body, and difficulty of measurements at this station.

iii) Model III: Propeller-Driven Body

The results are shown in Table VII and Fig. 44. From Table VII, it is seen that the drag coefficient is close to zero except for the station $X/D = 2$, where $C_D = 0.021$. Such discrepancy at $X/D = 2$ may be caused by the large tangential velocities in the flow field near the tail of the body and again difficulties of measurements at this station.

From Tables V-VII, it can be seen that the turbulence momentum and

TABLE V

Momentum Integrals: Model I

X/D	I_1	I_2	I_T	I_p	$C_D = 4(I_1 - I_2 - I_T) - 2I_p$
2	0.0299	0.00725	0.00034	0.000152	0.0869
5	0.0252	0.00508	0.000352	0.000547	0.07798
10	0.0275	0.00416	0.000576	0.0023	0.08644
20	0.0309	0.00263	0.000875	0.0027	0.1042
40	0.0288	0.00111	0.000908	0.0015	0.1040

TABLE VI

Momentum Integrals: Model II

X/D	I_1	I_2	I_T	I_p	$C_D = 4(I_1 - I_2 - I_T) - 2I_p$
2	0.00585	0.00186	0.0024	0.000712	0.0049
5	0.00333	0.001327	0.00149	0.000896	0.00026
10	0.00254	0.00302	0.00102	0.002712	0.00108
20	0.00265	0.000115	0.00129	0.002240	0.00137
40	0.00017	0.000002	0.0004615	0.000235	0.001644

TABLE VII

Momentum Integrals: Model III

X/D	I_1	I_2	I_T	I_p	$C_D = 4(I_1 - I_2 - I_T) - 2I_p$
2	0.00387	0.00425	0.001174	0.00748	-0.02117
5	0.00511	0.00152	0.0089	0.00636	-0.00192
10	0.00478	0.000408	0.000885	0.00807	-0.002192
20	0.00470	0.00007	0.00032	0.00763	0.00254
40	0.00382	0.000003	0.00009	0.00585	0.0032

pressure contribution cannot be neglected, and that the air-jet speed in the second model and the rpm of the propeller in the third model are sufficient to create nearly momentumless wake. From Figs. 42-44, it is seen that there are changes in all values of momentum integrals near the tail of the three bodies. This indicates the direct contribution of the body itself. The values of the momentum integrals approach constant values far downstream, except for some deviations for the case of Model II. The drag coefficients for Model II and Model III are fairly close to zero. The momentum change due to the mean flow plays an important role in the momentum analysis (see Fig. 42-44), so that the accuracy of mean flow measurements can be assessed by the momentum analysis.

Energy Balance Analysis

Assuming that the Reynolds number is sufficiently high so that the work done by viscous stresses is negligible, one can write the energy equation for a steady, axisymmetric mean flow of an incompressible fluid without a spiral component [26]:

$$\begin{aligned}
 & 2 \int \left[\frac{u}{U_e} \left(\frac{u^2 + v^2}{U_e^2} \right) - 1 \right] \frac{r}{R} d \frac{r}{R} + 2 \int \frac{u}{U_e} \frac{\bar{P}_A}{P_o} \frac{r}{R} d \frac{r}{R} \\
 & + 4 \int \left(\frac{u}{U_e} \frac{\overline{u'^2}}{U_e^2} + \frac{v}{U_e} \frac{\overline{u'v'}}{U_e^2} \right) \frac{r}{R} d \frac{r}{R} + 2 \int \left(1 - \frac{u}{U_e} \right) \frac{r}{R} d \frac{r}{R} \\
 & + 4 \iint \left[\frac{\overline{u'v'}}{U_e^2} \left(\frac{\partial u/U_e}{\partial r/R} + \frac{\partial v/U_e}{\partial x/R} \right) + \frac{\overline{u'^2}}{U_e^2} \frac{\partial u/U_e}{\partial x/R} \right. \\
 & \left. + \frac{\overline{v'^2}}{U_e^2} \frac{\partial v/U_e}{\partial r/R} + \frac{\overline{w'^2}}{U_e^2} \frac{v/U_e}{r/R} \right] \frac{r}{R} d \frac{r}{R} d \frac{x}{R} = 0 \quad (7)
 \end{aligned}$$

The first and fourth terms come from the energy equation of mean motion. The second, third and fifth terms represent the energy contributions due to pressure differences, turbulence and shear stresses.

For convenience, the following symbols are used:

$$S_1 \equiv \int \left[\frac{u}{U_e} \left(\frac{u^2 + v^2}{U_e^2} \right) \right] \frac{r}{R} d \frac{r}{R}$$

$$S_2 \equiv \int \frac{u}{U_e} \frac{\overline{u'^2}}{U_e^2} \frac{r}{R} d \frac{r}{R}$$

$$S_3 \equiv \int \frac{u}{U_e} \frac{r}{R} d \frac{r}{R}$$

$$S_4 \equiv \iint \frac{\overline{u'v'}}{U_e^2} \frac{\partial u/U_e}{\partial r/R} \frac{r}{R} d \frac{r}{R} d \frac{x}{R}$$

$$S_5 \equiv \iint \frac{\overline{u'^2}}{U_e^2} \frac{\partial u/U_e}{\partial x/R} \frac{r}{R} d \frac{r}{R} d \frac{x}{R} \equiv \int S_6 d \frac{x}{R}$$

$$S_7 \equiv \int \frac{v}{U_e} \frac{\overline{u'v'}}{U_e^2} \frac{r}{R} d \frac{r}{R}$$

$$S_8 \equiv \iint \frac{\overline{u'v'}}{U_e^2} \frac{\partial v/U_e}{\partial x/R} \frac{r}{R} d \frac{r}{R} d \frac{x}{R}$$

$$S_9 \equiv \iint \frac{\overline{v'^2}}{U_e^2} \frac{\partial v/U_e}{\partial r/R} \frac{r}{R} d \frac{r}{R} d \frac{x}{R}$$

$$S_{10} \equiv \iint \frac{\overline{w'^2}}{U_e^2} \frac{v/U_e}{r/R} \frac{r}{R} d \frac{r}{R} d \frac{x}{R}$$

$$S_{11} \equiv \int \frac{u}{U_e} \frac{\bar{P}_A}{P_o} \frac{r}{R} d \frac{r}{R}$$

Eqn. (7) can be expressed as

$$4S_{10} + 2S_{11} + 2S_1 + 4S_2 + 4S_7 - 2S_3 + 4S_4 + 4S_8 + 4S_5 + 4S_9 = 0 \quad (8)$$

The values of energy integrals are tabulated in Table X-XII and plotted in Figs. 45-47 (Δ is the deviation of the sum of integrals in Eqn. (7) from zero).

i) Model I: Streamlined Drag Body

For the streamlined body, the radial velocity v is assumed to be negligible as compared with the axial velocity at the stations $X/D = 2$ through 40; therefore, only six terms are considered ($S_1, S_2, S_3, S_4, S_5,$ and S_{11}). Table VIII shows that there is only a small deviation (Δ) of the experimental result as compared with the energy balance equation. Moreover, it shows that the turbulence contribution is very small as compared to the mean velocity contribution, and the energy balance in this case is not sensitive enough to detect errors in turbulence measurements.

ii) Model II: Jet-Propelled Body

Since the flow field of the air-injection model is more complicated than that of the streamlined body, the radial velocity may have to be taken into account. However, the radial velocity was not obtained from the measurements and, therefore, some estimates are needed. By the continuity equation in the cylindrical coordinate

TABLE VIII

Energy Integrals: Model I

X/D	$2S_{11}$	S_3	S_1	S_5	S_2	S_4	Δ
2	0.00315	0.47583	0.44215	-0.796×10^{-5}	0.00030	-0.000192	-0.06042
5	-0.00225	0.86841	0.83812	-0.188×10^{-4}	0.00038	-0.00055	-0.06576
10	0.0009	0.86573	0.82882	-0.319×10^{-4}	0.00051	-0.00115	-0.07458
20	0.00145	1.0973	1.0485	-0.719×10^{-4}	0.00083	-0.00146	-0.09867
40	0.0035	1.3622	1.3365	-0.135×10^{-3}	0.00066	-0.00211	-0.0502

TABLE IX

Radial Velocity of Estimates for Model II

\bar{v}/U_e r/R \ X/D	2	5	10	20	40
0.1	0.00115	0.000165	0.00	-0.000056	-0.000032
0.2	0.000542	-0.000110	-0.000165	-0.000052	-0.000062
0.3	0.000251	-0.000108	-0.00030	-0.000078	-0.000085
0.4	-0.000347	-0.000615	-0.000325	-0.000087	-0.000082
0.5	-0.000642	-0.00070	-0.000355	-0.000091	-0.000076
0.6	-0.000415	-0.000515	-0.000265	-0.000058	-0.000067
0.7	0.000201	-0.000214	-0.000097	-0.000002	-0.000061
0.8	0.000738	-0.000055	0.00001	0.0000475	-0.000051
0.9	0.00080	0.0001825	0.0001411	0.0000918	-0.000043
1.0	0.0007817	0.0002117	0.0001269	0.0000826	0.0000387

TABLE X

Energy Integrals: Model II

X/D	S_{11}	S_1	S_2	S_4	S_3	Δ
2	0.345×10^{-4}	0.78963	0.00218	-0.000932	0.78353	0.0192
5	0.15×10^{-4}	1.4030	0.0017298	-0.00195	1.3922	0.0204
10	0.25×10^{-3}	1.3974	0.001362	-0.00263	1.3914	0.0064
20	0.678×10^{-3}	2.0028	0.001854	-0.00288	2.00844	0.00721
40	0.410×10^{-3}	2.0005	0.000569	-0.00308	2.0002	0.0086

system written in the nondimensional form:

$$\frac{\partial u/U_e}{\partial x/D} = - \frac{2}{r/R} \frac{\partial}{\partial r/R} \left(\frac{v}{U_e} \frac{r}{R} \right)$$

$$\frac{v}{U_e} = \frac{1}{r/R} \frac{1}{2} \int_0^r \frac{\partial u/\partial x}{\partial x/D} \frac{r}{R} d \frac{r}{R} \quad (9)$$

the radial velocity v can be determined. This is done by plotting the axial mean velocity vs x/D at a fixed r/R and calculating and then integrating it. The results are listed in Table IX. This table shows that the radial mean velocity is very small as compared with the axial velocity. Therefore, all the terms involving v/U_e in the energy balance equation can be neglected so that only six terms ($S_1, S_2, S_3, S_4, S_5, S_{11}$) are considered. Of these, S_5 is roughly two orders of magnitude smaller than the remaining terms and, therefore, it can be neglected. The value of energy integrals for Model II are listed in Table X and plotted in Fig. 46. From Table X, it is seen that the deviation of the energy balance equation is even smaller than the deviation shown for Model I. Also, the turbulence contributions are larger while the pressure contributions are smaller than those for Model I.

iii) Model III: Propeller-Driven Body

The flow field of this model is not simple, hence all the terms of equation (7) should be evaluated as for Model II. The radial mean velocity was estimated by the same method as for Model II, since the

degree of swirling is not high (the yaw angle is less than seven degrees at the station $X/D = 2$) [19]. The radial velocity estimated as above is listed in Table XI. From this table, it is seen that the radial velocity is larger than that in the air-injection case. However, the values are still very low as compared with the axial velocity, therefore, it is still safe to neglect all the terms including \bar{v}/u_e in the energy balance equation. The term

$$\iint \frac{\overline{u'^2}}{u_e^2} \frac{u/U_e}{r/R} \frac{r}{R} d\frac{r}{R} d\frac{x}{R}$$

is negligible also. The values of energy integrals for Model III are listed in Table XII and plotted in Fig. 4'. Table XII shows that the deviations of experimental results are small as compared to those for Model I but they are slightly larger than or equal to the deviations estimated for Model II. The pressure and turbulence contributions are larger than those for Model I. The deviation Δ is the largest at station $X/D = 2$ where swirl is the largest.

TABLE XI

Radial Velocity Estimates for Model III

\bar{v}/U_e r/R	X/D	2	5
0.1		0.001415	0.00095
0.2		0.002245	0.0016675
0.3		0.00312	0.0018575
0.4		0.00343	0.0017425
0.5		0.002822	0.001443
0.6		0.002822	0.0011566
0.7		0.0021128	0.000666
0.8		0.0015299	0.0002455
0.9		0.0010	

TABLE XII

Energy Integrals: Model III

X/D	S_{11}	S_3	S_1	S_2	S_4	Λ
2	-0.0052	2.27261	2.7460	0.00127	-0.00088	-0.03096
5	-0.0036	2.0051	2.0198	0.00189	-0.00195	0.022
10	0.0016	2.0048	2.0156	0.00169	-0.00277	-0.02048
20	0.00351	3.5508	3.5416	0.00045	-0.00307	-0.0218
40	0.0039	3.5517	3.5442	0.00027	-0.00308	-0.01844

VII. CONCLUSIONS

In this work, the turbulence properties were measured in the wake behind three separate, but related bodies: Streamlined Drag Body, Jet-Propelled Body and Propeller-Driven Body; all with the same fore-body shape. The wake produced by the latter two models was momentumless. The turbulence properties included the axial, radial, and tangential turbulence intensities and the radial and tangential shear stresses, and the measurements were made at five stations: $X/D = 2, 5, 10, 20$ and 40 . After comparing the present results of the three models with each other and with the experimental results by other researchers, general conclusions may be drawn.

First, since the flow fields behind the tested bodies are very different, the turbulent characteristics of the wake of the three models are very different from one another. The size of the wake and the rates at which they decay are different. The wake of Model I is narrower than that of Model II which in turn is narrower than that of Model III. The axial turbulence intensity profiles measured in the radial direction are smooth curves with a single peak for Model I. Curves with some irregular distributions in the inner portion of the wake and a single smooth peak in the outer portion of the wake occur for Model II. For Model III curves with double peaks and a dip were obtained. The height of the peaks decreases in the downstream direction except at near stations for Model I. All the peaks disappear far downstream, and the rate of decay for Model III is the fastest among the three models. The magnitude of the axial turbulence intensity in

the wake of Model I is relatively lower than that for Model III which is lower than that for Model II. The radial and tangential turbulence intensity profiles have extra ripples after the first peak for Model I and very rough distributions for Model II. For Model III they have a higher peak after the first peak and a dip in between two peaks at near stations. The maximum value of these quantities decreases downstream for the three models, Model III has the highest value, and Model I has the lowest value among the three models. The radial shear stress profiles are smooth curves with a single peak for Model I and curves with a peak then a big dip for Model III. The absolute magnitude for Model II is higher than that of Model III. Because the decay rate of these quantities for Model III is much faster than for the other two models, the magnitude of these values for Model III are even lower than for the drag body at farther stations ($X/D = 20$, and 40). The tangential shear stress profiles show a high peak and a big dip for Model III. The magnitude of the tangential shear stress is relatively low for Models I and II as compared to Model III which exhibits the highest value at near stations but it also has the highest rate of decay.

Second, for the cases presented here, the momentum analysis suggests that the turbulence and pressure terms are of non-negligible magnitude, and so they have to be evaluated in order to have the drag coefficient exactly zero. This is especially necessary for the stations where the turbulence intensity is high (Model II) and the static pressure variations are large (Model III). According to the results presented in Section "RESULTS AND DISCUSSION," Model II and

Model III have very reasonable results, although the pressure and turbulence terms were not taken into account in evaluating the momentum analysis. The energy analysis suggests that the results presented are good in general, but the analysis cannot serve as a sensitive detection of the accuracy of turbulence measurements. Nevertheless, such analysis gives an insight into the overall flow structure and the mechanism of energy transformation.

Third, the wake characteristics of the blunt-tailed, semi-streamlined body studied by Chevray are similar to the wake characteristics of the present streamlined, drag body (Model I) though there remain some differences. The complex vortex system near the tail of a drag body has a significant influence on the turbulence characteristics at the stations near the body.

Fourth, the wake development of the blunt-body (disk) which was driven by a high-speed central jet to yield a zero momentum wake as studied by Naudascher is significantly different from the momentumless wake development of a slender, streamlined body driven by a peripheral jet.

Fifth, the accuracy of the measurements in this work is within takeable experimental errors according to the check of the momentum and energy balance analyses.

Finally, since there are few available results regarding momentumless wakes and this type of wake provides some basis for the analysis of submarine detection, further development and study in this area are still meaningful and practical. Therefore, it is recommended that the following experiments be undertaken:

1) Examine the effect of different diameter propellers and propellers with different pitch angles. Also, it is worthwhile to employ and compare a dual-propeller case.

2) A swirling, air injection model should be developed.

REFERENCES

1. Schlichting, H. (1930) Über das ebene Windschattenproblem, Ing. Arch. 1, 533-571.
2. Fage, A. and Falker, V. M. (1932) Appendix to a paper by G.I. Taylor. Proc. R. Soc. A135, 702.
3. Hall, A. A. and Hishop, G. S. (1938) velocity and temperature distributions in the turbulent wake behind a heated body of revolutions in the turbulent wake behind a heated body of revolution. Proc. Camb. Phil. Soc. 34, 345.
4. Hill, P. G., Schaub, U. S. and Senoo, T. (1963) Turbulent wakes in pressure gradients. J. Appl. Mech. 30, 518.
5. Townsend, A. A. (1956) The Structure of Turbulent Shear Flow. Cambridge Univ. Press.
6. Cooper, R. D. and Lutzky, M. (1955) Exploratory investigation of the turbulent wakes behind bluff bodies. DTMB R & D Rept. No. 953, October.
7. Carmody, T. (1964) Establishment of a wake behind a disk, J. Bas. Engng. 87, 869-882.
8. Buchinskaya, E. K. and Pochkina, K. A. (1966) Investigation of a vortex wake behind a body of revolution. Prom. Aerodinamika No. 27, 121-144.
9. Gartshore, I. (1967) Two-dimensional turbulent wakes, J. Fluid Mech., 30, 547-560.
10. Chevray, R. (1968) The turbulent wake of a body of revolution. J. Bas. Engng., 90, 275-284.
11. Bukreev, V. A., Kostomakha and Lytkin, Yu. M. (1972), Axisymmetric turbulent wake behind a streamlined body. Siberskoe Otdelenie An SSSR, Institute Gidrodinamiki, Dinamika Sploshnoi Sredy.
12. Naudascher, E. (1965) Flow in the wake of a self-propelled bodies and related sources of turbulence. J. Fluid Mech. Vol. 22, part 4, 625-656.
13. Ginevski, A. S., Pochkina, K. A. and Ukhanova, L. N. (1966) Propagation of turbulent jet flow with zero momentum. Fluid Dynamics Academy of Sciences USSR, Vol. 1, No. 6, Nov. - Dec., Faraday Press, Inc.

14. Gran, R. L. (1973) An experiment on the wake of a slender propeller-driven body. TRW Rept. 20086-6006-RU-00.
15. Reichardt, H. (1951) Gesetzmässigkeiten der freien Turbulent. VDI-Forsch., 414.
16. Ilizarova, L. I. and Pochkina, K. A. (1962) Experimental study of a wake behind a body of revolution. Prom. Aerodynamika No. 23.
17. Bradbury, L. J. S. (1965) The structure of a self-preserving turbulent plane jet. J. Fluid Mech. Vol. 1, part , 31-64.
18. Hokenson, G. J., Schetz, J. A. (1972) Free Turbulent Mixing in Axial Pressure Gradients. J. of Applied Mechanics.
19. Swanson, R. C. (1974) Ph.D. Thesis, Aerospace and Ocean Engrg. Dept., VPI & SU, Oct. 1974, also to be published as VPI-Aero-017 by R. C. Swanson, A. K. Jakubowski, and J. A. Schetz.
20. Kovaszny, L. S. G. (1967) should we still use hot wires. In Advances In Hot-Wire Anemometry (McInik, W. L., Weske, J. R., Eds.) pp. 2-12, Dept. of Aerospace Engrg., Univ. of Maryland, College Park, Maryland.
21. TSI Anemometry. (1973) Thero-Systems Inc.
22. Sandborn, V. A. (1972) Resistance Temperature Transducers Metrology Press, Fort Collins, Colorado.
23. Tieleman, H. W. (1967) Viscous Region of Turbulent Boundary Layer. Colorado State Univ., Tech. Rept. CER67-68HWT21.
24. Corrsin, S. and Uberoi, S. (1949) Further experiments on the flow and heat transfer in a heated turbulent air jet. NACA TN. 1865.
25. Rouse, H. (1959) Advanced Mechanics of Fluids. Ed. Wiley, New York.
26. Rouse, H. (1960) Distribution of energy in regions of separations. La Houille Blanche, No. 3, May, No. 4. Jene.

APPENDIX A
SYMMETRY OF THE WAKE

APPENDIX A

The values listed in the Table A-1 and A-2 are the raw axial turbulence data given in the RMS volt units. Since the RMS value is rather insensitive to the temperature variations (for the probes and constant temperature system applied in these experiments), it can be used to check the symmetry of the wake by measuring the RMS value at points which are at the same distance from the center of the wake but in different directions (horizontal left, horizontal right, and vertical downward).

TABLE A-1

RMS values (in volts) recorded by straight hot-wire at the same r but different directions: (Model I)

X/D	$r = 1$ in.			$r = 2$ in.			$r = 3$ in.		
	Left	Down	Right	Left	Down	Right	Left	Down	Right
2	0.0295	0.0298	0.0263	0.0076	0.0070	0.0085	0.0028	0.0019	0.0019
10	0.0282	0.0277	0.0247	0.0223	0.0182	0.0209	0.0025	0.0058	0.0017
20	0.0197	0.0190	0.0182	0.0169	0.0178	0.0162	0.0055	0.0079	0.0064
40	0.0127	0.0115	0.0115	0.0120	0.0119	0.0115	0.0099	0.0115	0.0101

TABLE A-2

RMS values (in volts) recorded by straight hot-wire at the same r but different directions: (Model II)

X/D	$r = 1$ in.			$r = 2$ in.			$r = 3$ in.		
	Left	Down	Right	Left	Down	Right	Left	Down	Right
2	0.0397	0.0186	0.0288	0.0186	0.0382	0.0401	0.0036	0.0061	0.0211
5	0.0330	0.0256	0.0344	0.0316	0.0385	0.0387	0.0065	0.0140	0.0140
10	0.0250	0.0272	0.0293	0.0250	0.0254	0.0260	0.0098	0.0088	0.0155
20	0.0250	0.0209	0.0236	0.0273	0.0227	0.0255	0.0198	0.0175	0.0222
40	0.0130	0.0158	0.0118	0.0142	0.0150	0.0118	0.0138	0.0104	0.0102

APPENDIX B
TABULATED DATA

TABLE B-1
Axial Turbulence Intensity for Model I

$$\frac{\sqrt{u'^2}}{U_e}$$

Radial Pos. (in.)	X/D = 2	5	10	20	40
0.00	0.0262	0.0278	0.0383	0.0385	0.0259
0.25	0.0323	0.0329	0.0443	0.0398	0.0266
0.50	0.0387	0.0492	0.0489	0.0412	0.0266
0.75	0.0511	0.0545	0.0542	0.0428	0.0268
1.00	0.0496	0.0577	0.0591	0.0450	0.0272
1.25	0.0487	0.0478	0.0578	0.0457	0.0270
1.50	0.0406	0.0332	0.0552	0.0475	0.0277
1.75	0.0315	0.0187	0.0468	0.0483	0.0280
2.00	0.0163	0.0066	0.0322	0.0470	0.0282
2.25	0.0061	0.0047	0.0161	0.0437	0.0282
2.50	0.0056	0.0022	0.0076	0.0398	0.0278
2.75	-----	-----	0.0054	0.0322	0.0282
3.00	0.0054	0.0043	0.0049	0.0247	0.0271
3.25	-----	-----	-----	0.0179	0.0264
3.50	-----	-----	-----	0.0116	0.0238
3.75	-----	-----	-----	0.0073	0.0215
4.00	0.0054	0.0043	0.0042	0.0057	0.0192
4.25	-----	-----	-----	-----	0.0164
4.50	-----	-----	0.0040	0.0042	0.0139
4.75	-----	-----	-----	-----	0.0111
5.00	-----	-----	-----	0.0035	0.0090

TABLE B-2
Radial Turbulence Intensity for Model I

$$\frac{\sqrt{v'^2}}{U_e}$$

Radial Pos. (in.)	X/D = 2	5	10	20	40
0.00	0.0214	0.0288	0.0277	0.0242	0.0251
0.25	0.0253	0.0329	0.0280	0.0245	0.0145
0.50	0.0321	0.0309	0.0316	0.0257	0.0143
0.75	0.0268	0.0363	0.0317	0.0259	0.0142
1.00	0.0310	0.0355	0.0267	0.0256	0.0141
1.25	0.0189	0.0212	0.0271	0.0263	0.0143
1.50	0.0154	0.0213	0.0227	0.0237	0.0132
1.75	0.0029	0.0147	0.0180	0.0200	0.0131
2.00	0.0026	0.0106	0.0139	0.0183	0.0129
2.25	0.0033	0.0079	0.0122	0.0194	0.0121
2.50	0.0012	0.0052	0.0075	0.0183	0.0129
2.75	-----	0.0061	0.0054	0.0169	0.0079
3.00	0.0012	0.0050	0.0037	0.0139	0.0087
3.25	-----	-----	-----	0.0105	0.0075
3.50	-----	-----	-----	0.0086	0.0066
3.75	-----	-----	-----	0.0079	0.0077
4.00	0.0012	0.0053	0.0031	0.0060	0.0064
4.25	-----	-----	-----	-----	-----
4.50	-----	-----	0.0034	0.0044	0.0075
4.75	-----	-----	-----	-----	0.0084
5.00	-----	-----	-----	0.0040	0.0076
5.50	-----	-----	-----	-----	0.0056

TABLE B-3

Tangential Turbulence Intensity for Model I

$$\frac{\sqrt{w'^2}}{U_e}$$

Radial Pos. (in.)	X/D = 2	5	10	20	40
0.00	0.0218	0.0286	0.0277	0.0256	0.0174
0.25	0.0282	0.0320	0.0255	0.0262	0.0164
0.50	0.0354	0.0312	0.0282	0.0271	0.0171
0.75	0.0303	0.0389	0.0340	0.0287	0.0166
1.00	0.0325	0.0421	0.0311	0.0281	0.0164
1.25	0.0215	0.0333	0.0334	0.0287	0.0169
1.50	0.0181	0.0295	0.0308	0.0269	0.0162
1.75	0.0019	0.0226	0.0280	0.0228	0.0158
2.00	0.0067	0.0147	0.0264	0.0209	0.0157
2.25	0.0003	0.0068	0.0155	0.0203	0.0153
2.50	0.0018	0.0053	0.0086	0.0153	0.0151
2.75	-----	0.0063	0.0050	0.0151	0.0100
3.00	0.0012	0.0051	0.0042	0.0068	0.0099
3.25	-----	-----	-----	0.0062	0.0059
3.50	-----	-----	-----	0.0052	0.0078
3.75	-----	-----	-----	0.0059	0.0087
4.00	0.0012	0.0052	0.0036	0.0049	0.0065
4.25	-----	-----	-----	-----	0.0063
4.50	-----	-----	0.0037	0.0044	0.0072
4.75	-----	-----	-----	-----	0.0067
5.00	-----	-----	-----	0.0042	0.0062
5.50	-----	-----	-----	-----	0.0049

TABLE B-4

Radial Shear Stress for Model I

$$-\frac{u'v'}{U^2} \times 10^2$$

Radial Pos. (in.)	X/D = 2	5	10	20	40
0.00	-0.0037	0.0017	0.0121	0.0023	-0.0018
0.25	0.0298	0.0298	0.0366	0.0135	0.0003
0.50	0.0480	0.0554	0.0535	0.0255	0.0025
0.75	0.0592	0.0848	0.0749	0.0319	0.0051
1.00	0.0660	0.0878	0.0747	0.0422	0.0067
1.25	0.0520	0.0683	0.0739	0.0477	0.0084
1.50	0.0332	0.0456	0.0583	0.0505	0.0100
1.75	0.0140	0.0206	0.0402	0.0446	0.0106
2.00	0.0024	0.0057	0.0181	0.0422	0.0117
2.25	0.00013	0.0003	0.0063	0.0370	0.0122
2.50	0.00006	-0.0002	0.0005	0.0303	0.0129
2.75	-----	-0.0004	-0.00008	0.0197	0.0129
3.00	0.00007	-0.0002	-0.0001	0.0118	0.0117
3.25	-----	-----	-----	0.0058	0.0085
3.50	-----	-----	-----	0.0017	0.0070
3.75	-----	-----	-----	0.0007	0.0057
4.00	0.00007	0.00007	-0.0001	0.0002	0.0035
4.25	-----	-----	-----	-----	0.0028
4.50	-----	-----	-----	-0.00009	0.0025
4.75	-----	-----	-----	-----	0.00099
5.00	-----	-----	-----	-0.00006	0.0003
5.50	-----	-----	-----	-----	.00001

TABLE B-5
Tangential Shear Stress for Model I

$$\frac{u'w'}{U_e^2} \times 10^2$$

Radial Pos. (in.)	X/D = 2	5	10	20	40
0.00	0.0131	0.0077	0.0071	0.0133	-0.0034
0.25	0.0142	0.0122	0.0116	0.0158	0.0021
0.50	0.0244	0.0154	0.0096	0.0167	0.0016
0.75	0.0232	0.0299	0.0203	0.0177	0.0018
1.00	0.0264	0.0441	0.0206	0.0172	0.0019
1.25	0.0171	0.0290	0.0179	0.0133	0.0011
1.50	0.0069	0.0187	0.0176	0.0106	-0.00025
1.75	0.0023	0.0073	0.0138	0.0074	-0.00057
2.00	0.0003	0.0032	0.0122	0.0066	-0.0014
2.25	-0.0001	0.0004	0.0045	0.0070	-0.0013
2.50	-0.0001	0.00004	0.0009	0.0078	-0.00079
2.75	-----	0.0001	0.0001	0.0052	0.00070
3.00	-0.0001	0.00005	-0.00002	0.0027	0.0011
3.25	-----	-----	-----	0.0011	0.00028
3.50	-----	-----	-----	0.00035	0.0085
3.75	-----	-----	-----	0.00004	0.0070
4.00	-0.0001	0.0001	-0.00006	0.00007	0.0057
4.25	-----	-----	-----	-----	0.0035
4.50	-----	-----	-----	0.00004	0.0028
4.75	-----	-----	-----	-----	0.0025
5.00	-----	-----	-----	0.00005	0.00099
5.50	-----	-----	-----	-----	0.00030

TABLE B-6
Axial Turbulence Intensity for Moel II

$$\frac{\sqrt{u'^2}}{U_e}$$

Radial Pos. (in.)	X/D = 2	5	10	20	40
0.00	0.1108	0.0511	0.0456	0.0520	0.0429
0.125	0.1108	-----	-----	-----	-----
0.25	0.1041	0.0511	0.0480	0.0526	0.0410
0.50	0.0788	0.0521	0.0512	0.0545	0.0387
0.625	0.0571	-----	-----	-----	-----
0.75	0.0554	0.0507	0.0582	0.0568	0.0376
0.875	0.0516	-----	-----	-----	-----
1.00	0.0533	0.0503	0.0642	0.0586	0.0383
1.25	0.0726	0.0698	0.0680	0.0607	0.0383
1.50	0.0941	0.0748	0.0695	0.0622	0.0383
1.75	0.1063	0.0793	0.0675	0.0636	0.0350
1.875	0.1056	-----	-----	-----	-----
2.00	0.1017	0.0758	0.0599	0.0634	0.0343
2.125	0.0912	-----	-----	-----	-----
2.25	0.0738	0.0649	0.0498	0.0590	0.0312
2.50	0.0523	0.0472	0.0387	0.0531	0.0287
2.75	0.0315	0.0307	0.0275	0.0463	0.0248
3.00	0.0175	0.0274	0.0208	0.0384	0.0216
3.25	0.0123	0.0140	0.0137	0.0319	0.0166
3.75	0.0110	0.0081	0.0089	0.0201	0.0104
4.00	0.0111	0.0077	0.0082	0.0150	0.0082
4.25	0.0109	0.0075	0.0080	0.0124	0.0064
4.50	0.0110	0.0075	0.0080	0.0114	0.0052
4.75	-----	-----	-----	0.0109	-----
5.00	0.0108	0.0075	0.0078	0.0107	0.0050
5.50	-----	-----	0.0087	0.0102	-----

TABLE B-7
Radial Turbulence Intensity for Model II

$$\frac{\sqrt{v'^2}}{U_e}$$

Radial Pos. (in.)	X/D = 2	5	10	20	40
0.00	0.0737	0.0361	0.0275	0.0116	0.0117
0.125	0.0736	-----	-----	-----	-----
0.25	0.0674	0.0364	0.0259	0.0146	0.0200
0.50	0.0142	0.0372	0.0295	0.0145	0.0272
0.625	0.0281	-----	-----	-----	-----
0.75	0.0242	0.0380	0.0291	0.0132	0.0306
0.875	0.0154	-----	-----	-----	-----
1.00	0.0064	0.0503	0.0279	0.0172	0.0313
1.25	0.0307	0.0565	0.0330	0.0220	0.0319
1.50	0.0481	0.0564	0.0343	0.0270	0.0329
1.75	0.0634	0.0513	0.0336	0.0278	0.0342
1.875	0.0706	-----	-----	-----	-----
2.00	0.0674	0.0401	0.0324	0.0310	0.0328
2.125	0.0611	-----	-----	-----	-----
2.25	0.0423	0.0229	0.0295	0.0351	0.0329
2.50	0.0314	0.0225	0.0269	0.0368	0.0303
2.75	0.0122	0.0210	0.0223	0.0375	0.0263
3.00	0.0092	0.0171	0.0189	0.0363	0.0225
3.25	0.0116	0.0157	0.0170	0.0324	0.0208
3.50	0.0118	0.0139	0.0148	0.0273	0.0153
3.75	0.0117	0.0141	0.0142	0.0207	0.0129
4.00	0.0118	0.0138	0.0139	0.0167	0.0113
4.25	0.0118	0.0140	0.0140	0.0131	0.0110
4.50	0.0121	0.0139	0.0139	0.0114	0.0104
5.00	0.0127	0.0139	0.0139	0.0101	0.0101
6.00	-----	-----	0.0137	0.0102	0.0101

TABLE B-8
Tangential Turbulence Intensity for Model II

$$\frac{\sqrt{w'^2}}{U_e}$$

Radial Pos. (in.)	X/D = 2	5	10	20	40
0.0	0.0752	0.0395	0.0280	0.0133	0.0082
0.125	0.0753	-----	-----	-----	-----
0.25	0.0719	0.0392	0.0272	0.0052	0.0167
0.50	0.0279	0.0378	0.0314	0.0124	0.0238
0.625	0.0179	-----	-----	-----	-----
0.75	0.0234	0.0374	0.0301	0.0145	0.0264
0.875	0.0217	-----	-----	-----	-----
1.00	0.0157	0.0460	0.0292	0.0099	0.0279
1.25	0.0291	0.0535	0.0261	0.0050	0.0279
1.50	0.0469	0.0505	0.0241	0.0074	0.0277
1.75	0.0611	0.0455	0.0175	0.0089	0.0300
1.875	0.0700	-----	-----	-----	-----
2.00	0.0681	0.0376	0.0091	0.0136	0.0295
2.125	0.0555	-----	-----	-----	-----
2.25	0.0415	0.0253	0.0106	0.0254	0.0304
2.50	0.0283	0.0158	0.0188	0.0320	0.0281
2.75	0.0190	0.0126	0.0174	0.0325	0.0264
3.00	0.0120	0.0163	0.0155	0.0326	0.0219
3.25	0.0136	0.0151	0.0155	0.0249	0.0189
3.50	0.132	0.0144	0.0137	0.0259	0.0148
3.75	0.0131	0.0146	0.0134	0.0197	0.0130
4.00	0.0130	0.0148	0.0134	0.0158	0.0110
4.25	0.0120	0.0147	0.0133	0.0121	0.0097
4.50	0.0117	0.0146	0.0131	0.0113	0.0091
5.00	0.0119	0.0148	0.0132	0.0098	0.0085
5.50	-----	-----	-----	-----	0.0087

TABLE B-9
Radial Shear Stress for Model II

Radial Pos. (in.)	X/D = 2	5	10	20	40
0.00	-0.0418	-0.00057	0.0057	-0.0109	-0.0147
0.125	-0.00615	-----	-----	-----	-----
0.25	0.0231	0.0356	-0.0178	-0.0162	-0.0175
0.50	0.0831	0.0482	-0.0416	-0.0327	-0.0185
0.625	0.0856	-----	-----	-----	-----
0.75	0.0414	0.0206	-0.0726	-0.0470	-0.0209
0.875	0.0010	-----	-----	-----	-----
1.00	-0.0277	-0.0587	-0.1000	-0.0580	-0.0210
1.25	-0.0955	-0.0133	-0.1176	-0.0622	-0.0212
1.50	-0.1768	-0.1800	-0.1120	-0.0691	-0.0164
1.75	-0.2102	-0.1720	-0.1062	-0.0669	-0.0176
1.875	-0.2308	-----	-----	-----	-----
2.00	-0.2071	-0.1170	-0.0900	-0.0640	-0.0154
2.125	-0.1398	-----	-----	-----	-----
2.25	-0.0878	-0.0680	-0.0611	-0.0599	-0.0142
2.50	-0.0179	-0.0269	-0.0298	-0.0479	-0.0105
2.75	-0.0031	-0.0074	-0.0167	-0.0400	-0.0095
3.00	-0.0019	-0.0026	-0.0072	-0.0289	-0.0071
3.25	-0.0014	-0.00143	-0.0010	-0.0158	-0.0053
3.50	-0.0011	0.000231	0.0011	-0.0131	-0.0040
3.75	-0.00097	0.000313	0.0016	-0.0060	-0.0018
4.00	-0.0012	0.00036	0.0014	-0.0025	-0.0010
4.25	-0.00092	0.00038	0.0018	-0.0013	0.00052
4.50	-0.00095	0.00022	0.0016	-0.00068	-0.00025
5.00	-0.00105	-0.00002	0.0016	-0.0011	-0.00004
5.50	-----	-----	-----	-----	0.0001

TABLE B-10
Tangential Shear Stress for Model II

Radial Pos. (in.)	X/D = 2	$\frac{u'w'}{2Ue} \times 10^2$			
		5	10	20	40
0.00	0.0542	0.0103	-0.0144	-0.0129	-0.0095
0.125	0.0502	-----	-----	-----	-----
0.25	0.0345	0.0115	-0.0124	-0.0048	-0.00145
0.50	0.0414	-0.00265	-0.0229	-0.0117	-0.00224
0.625	0.0399	-----	-----	-----	-----
0.75	0.0171	0.00068	-0.0195	-0.0118	-0.00051
0.875	0.00991	-----	-----	-----	-----
1.00	-0.00023	-0.0219	-0.0269	-0.0107	-0.00072
1.25	0.0134	-0.0373	-0.0316	-0.01327	0.000139
1.50	0.0040	-0.0413	-0.0191	-0.0086	-0.00077
1.75	-0.0550	-0.0158	-0.0200	-0.0117	0.0027
1.875	-0.107	-----	-----	-----	-----
2.00	-0.1200	0.0109	-0.0222	-0.0043	-0.000046
2.125	-0.0948	-----	-----	-----	-----
2.25	-0.0643	0.0220	-0.0116	-0.0066	+0.00465
2.50	-0.0214	0.0095	-0.0070	0.00086	0.00236
2.75	-0.0042	0.0023	-0.0047	0.0051	0.00184
3.00	0.0012	0.0020	-0.0012	0.0074	0.00245
3.25	0.0026	0.0015	-0.000061	-0.0076	0.00291
3.50	0.0023	0.0016	-0.0010	0.0035	0.00221
3.75	0.0020	0.0013	-0.00073	0.0011	0.00124
4.00	0.0021	0.0015	-0.00043	-0.00058	0.00178
4.25	0.0007	0.0016	-0.00026	-0.00055	0.00107
4.50	0.0012	0.0014	-0.00032	-0.00050	0.00173
5.00	0.0011	0.0016	-0.000055	-0.00078	0.00124
5.50	-----	-----	-----	-----	0.00107

TABLE B-11
Axial Turbulence Intensity for Model III

$$\frac{\sqrt{u'^2}}{U_e}$$

Radial Pos. (in.)	X/D = 2	5	10	20	40
0.00	0.0505	0.0522	0.0400	0.0200	0.0130
0.25	0.0512	0.0544	0.0400	0.0201	0.0130
0.50	0.0587	0.0586	0.0393	0.0202	0.0129
0.75	0.0654	0.0604	0.0400	0.0205	0.0130
1.00	0.0677	0.0604	0.0416	0.0204	0.0132
1.25	0.0620	0.0600	0.0429	0.0206	0.0134
1.50	0.0540	0.0596	0.0444	0.0207	0.0135
1.75	0.0440	0.0560	0.0444	0.0206	0.0136
2.00	0.0335	0.0466	0.0440	0.0203	0.0136
2.25	0.0329	0.0428	0.0445	0.0201	0.0136
2.50	0.0402	0.0433	0.0407	0.0199	0.0134
2.75	0.0550	0.0483	0.0388	0.0196	0.0130
3.00	0.0447	0.0521	0.0372	0.0192	0.0126
3.25	0.0272	0.0460	0.0347	0.0188	0.0124
3.50	0.0156	0.0333	0.0343	0.0186	0.0121
3.75	0.0106	0.0273	0.0345	0.0177	0.0117
4.00	0.0073	0.0223	0.0321	0.0169	0.0113
4.50	0.0038	0.0245	0.0234	0.0140	0.0099
5.00	0.0033	0.0205	0.0177	0.0117	0.0090
6.00	0.0031	0.0123	0.0105	0.0072	0.0067
7.00	-----	-----	0.0091	0.0040	0.0051

TABLE B-12
Radial Turbulence Intensity for Model III

$$\frac{\sqrt{v'^2}}{U_e}$$

Radial Pos. (in.)	X/D = 2	5	10	20	40
0.00	0.0571	0.0562	0.0450	0.0289	0.0151
0.25	0.0593	0.0551	0.0453	0.0289	0.0150
0.50	0.0646	0.0576	0.0458	0.0287	0.0154
0.75	0.0769	0.0614	0.0470	0.0290	0.0154
1.00	0.0759	0.0658	0.0466	0.0290	0.0154
1.25	0.0655	0.0672	0.0471	0.0292	0.0152
1.50	0.0549	0.0670	0.0466	0.0288	0.0156
1.75	0.0466	0.0622	0.0472	0.0294	0.0155
2.00	0.0378	0.0614	0.0455	0.0292	0.0158
2.25	0.0408	0.0576	0.0438	0.0292	0.0158
2.50	0.0573	0.0681	0.0416	0.0295	0.0156
2.75	0.1023	0.0974	0.0392	0.0295	0.0154
3.00	0.0673	0.0891	0.0384	0.0294	0.0154
3.25	0.0363	0.0734	0.0378	-----	0.0148
3.50	0.0228	0.0419	0.0394	0.0273	0.0145
3.75	0.0154	0.0213	0.0379	0.0265	0.0146
4.00	0.0115	0.0104	0.0370	0.0242	0.0138
4.50	0.0074	0.0168	0.0286	0.0206	0.0123
5.00	0.0070	0.0125	0.0164	0.0175	0.0109
6.00	0.0062	0.0206	0.0077	0.0117	0.0088
8.00	0.0052	-----	0.0051	0.0044	0.0050

TABLE B-13
Tangential Turbulence Intensity for Model III

$$\frac{\sqrt{w'^2}}{U_e}$$

Radial Pos. (in.)	X/D = 2	5	10	20	40
0.00	0.0592	0.0592	0.0438	0.0289	0.0155
0.25	0.0594	0.0572	0.0448	0.0289	0.0156
0.50	0.0649	0.0601	0.0452	0.0287	0.0159
0.75	0.0749	0.0661	0.0459	0.0288	0.0158
1.00	0.0804	0.0683	0.0464	0.0285	0.0157
1.25	0.0745	0.0650	0.0473	0.0283	0.0155
1.50	0.0722	0.0627	0.0466	0.0275	0.0148
1.75	0.0601	0.0607	0.0467	0.0275	0.0151
2.00	0.0435	0.0549	0.0454	0.0268	0.0150
2.25	0.0358	0.0421	0.0459	0.0267	0.0149
2.50	0.0374	0.0418	0.0441	0.0268	0.0145
2.75	0.0674	0.0479	0.0433	0.0265	0.0142
3.00	0.0420	0.0528	0.0432	0.0260	0.0140
3.25	0.0220	0.0370	0.0438	0.0255	0.0137
3.50	0.0138	0.0070	0.0451	0.0244	0.0136
3.75	0.0101	0.0142	0.0421	0.0237	0.0135
4.00	0.0075	0.0139	0.0398	0.0224	0.0129
4.50	0.0058	0.0234	0.0301	0.0196	0.0120
5.00	0.0053	0.0212	0.0169	0.0167	0.0108
6.00	0.0051	0.0078	0.0105	0.0107	0.0088
8.00	0.0053	-----	0.0084	0.0048	0.0049

TABLE B-14
Radial Shear Stress for Model III

$$-\frac{u'v'}{2} \lambda 10^2$$

Radial Pos. (in.)	X/D = 2	5	10	20	40
0.00	-0.0215	-0.0328	-0.0060	0.0021	0.00072
0.25	0.0852	0.0272	0.0066	0.0055	0.0014
0.50	0.152	0.1071	0.0154	0.0086	0.0018
0.75	0.231	0.1344	0.0260	0.0105	0.0020
1.00	0.243	0.1546	0.0385	0.0117	0.0019
1.25	0.192	0.1700	0.0502	0.0106	0.0017
1.50	0.133	0.1667	0.0726	0.0101	0.0020
1.75	0.0692	0.1286	0.0782	0.0083	0.0013
2.00	0.0113	0.0856	0.0841	0.0086	0.0012
2.25	-0.0273	0.0248	0.0859	0.0078	0.00099
2.50	-0.0396	-0.0247	0.0759	0.0067	0.0012
2.75	-0.0092	-0.0710	0.0625	0.0059	0.00097
3.00	-0.0116	-0.0351	0.0481	0.0051	0.0014
3.25	0.0030	0.0088	0.0254	-----	0.0013
3.50	-0.0022	0.0070	0.0163	0.0047	0.0013
3.75	-0.00052	-0.0041	0.0098	0.0050	0.0017
4.00	-0.00039	-0.00068	0.0105	0.0032	0.0018
4.50	-0.00024	0.0025	0.0080	0.0011	0.0017
5.00	-0.00005	0.00077	0.0078	0.0016	0.0012
6.00	-0.00028	-0.000996	-0.000047	-0.00012	0.00013

TABLE B-15
Tangential Shear Stress for Model III

Radial Pos. (in.)	$\frac{u'w'}{Ue} \times 10^2$				
	X.D = 2	5	10	20	40
0.00	0.0401	-0.0349	0.0101	-0.00017	-0.0018
0.25	0.0603	0.0170	0.0155	0.0025	-0.0002
0.50	0.0509	0.0412	0.0198	0.0063	0.00048
0.75	0.0849	0.0645	0.0252	0.0086	0.0010
1.00	0.1879	0.0725	0.0155	0.0100	0.0013
1.25	0.2007	0.0607	0.0184	0.0107	0.0023
1.50	0.1795	0.0688	0.0162	0.0105	0.0029
1.75	0.0806	0.0553	0.0155	0.0104	0.0028
2.00	0.0008	0.0073	0.0155	0.0105	0.0025
2.25	-0.0469	-0.0003	0.0069	0.0096	0.0023
2.50	-0.1129	-0.0638	0.0069	0.0094	0.0018
2.75	-0.1384	-0.0964	0.0025	0.0057	0.0016
3.00	-0.1579	-0.1416	0.0050	0.0045	0.00087
3.25	-0.0437	-0.0767	0.0110	0.0034	0.00055
3.50	-0.0177	-0.0127	0.0108	0.0015	0.00036
3.75	-0.0080	-0.00486	0.0082	0.00086	0.000086
4.00	-0.0031	0.0019	0.0109	0.00082	-0.00031
4.50	-0.00052	-0.0015	-0.0065	0.00049	-0.00059
5.00	-0.00033	0.0020	-0.0043	-0.00024	-0.00050
6.00	-0.00018	-0.0002	0.0020	-0.00028	-0.00038
8.00	-0.00025	-----	0.0018	0.00019	-0.000078

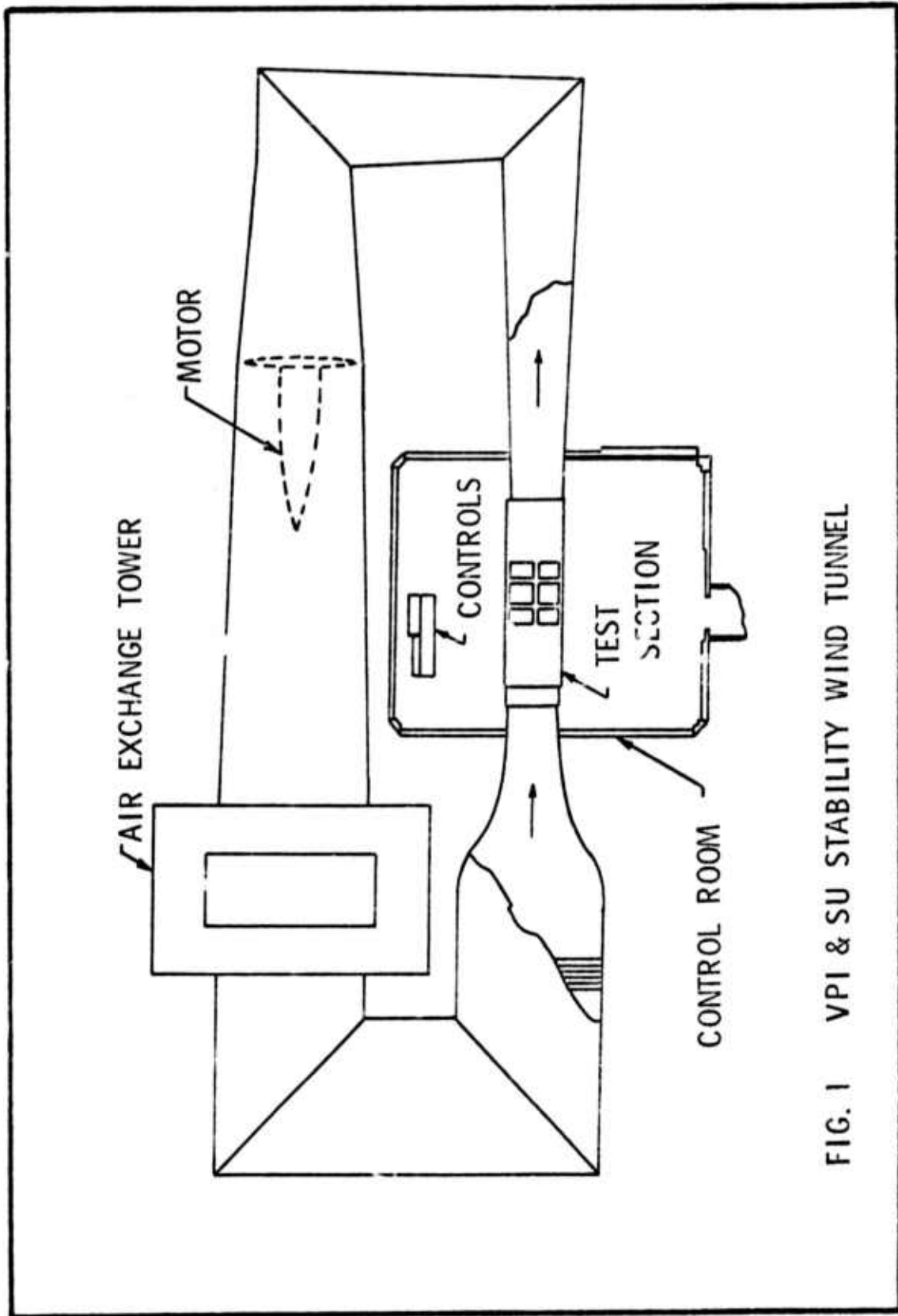


FIG. 1 VPI & SU STABILITY WIND TUNNEL

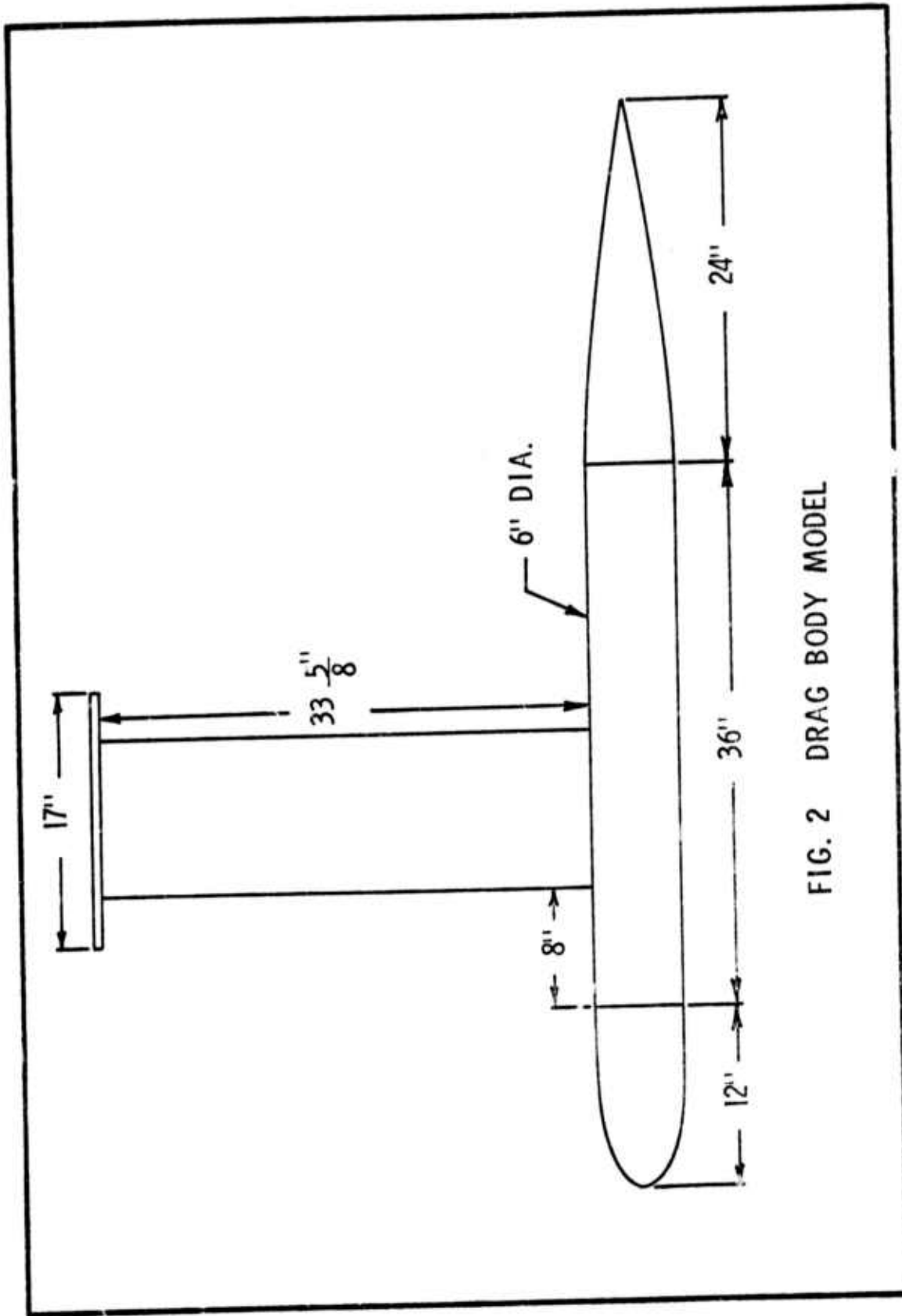


FIG. 2 DRAG BODY MODEL

70

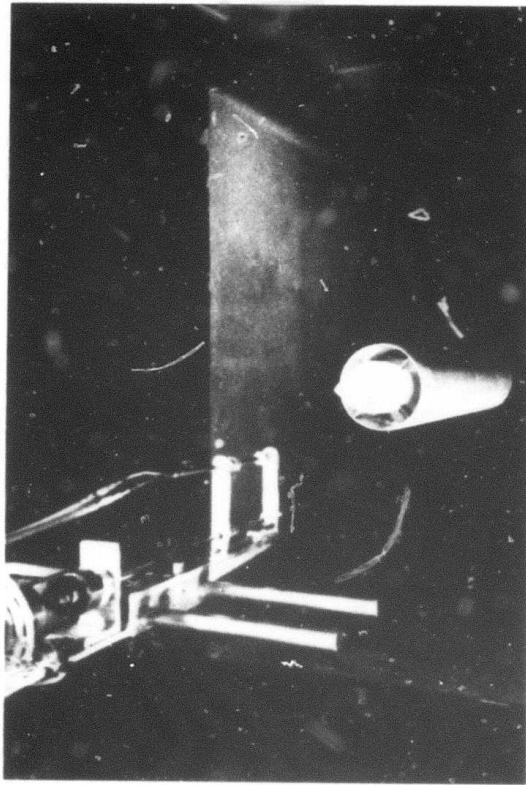


FIG. 3 PHOTOGRAPH OF JET-PROPELLED MODEL

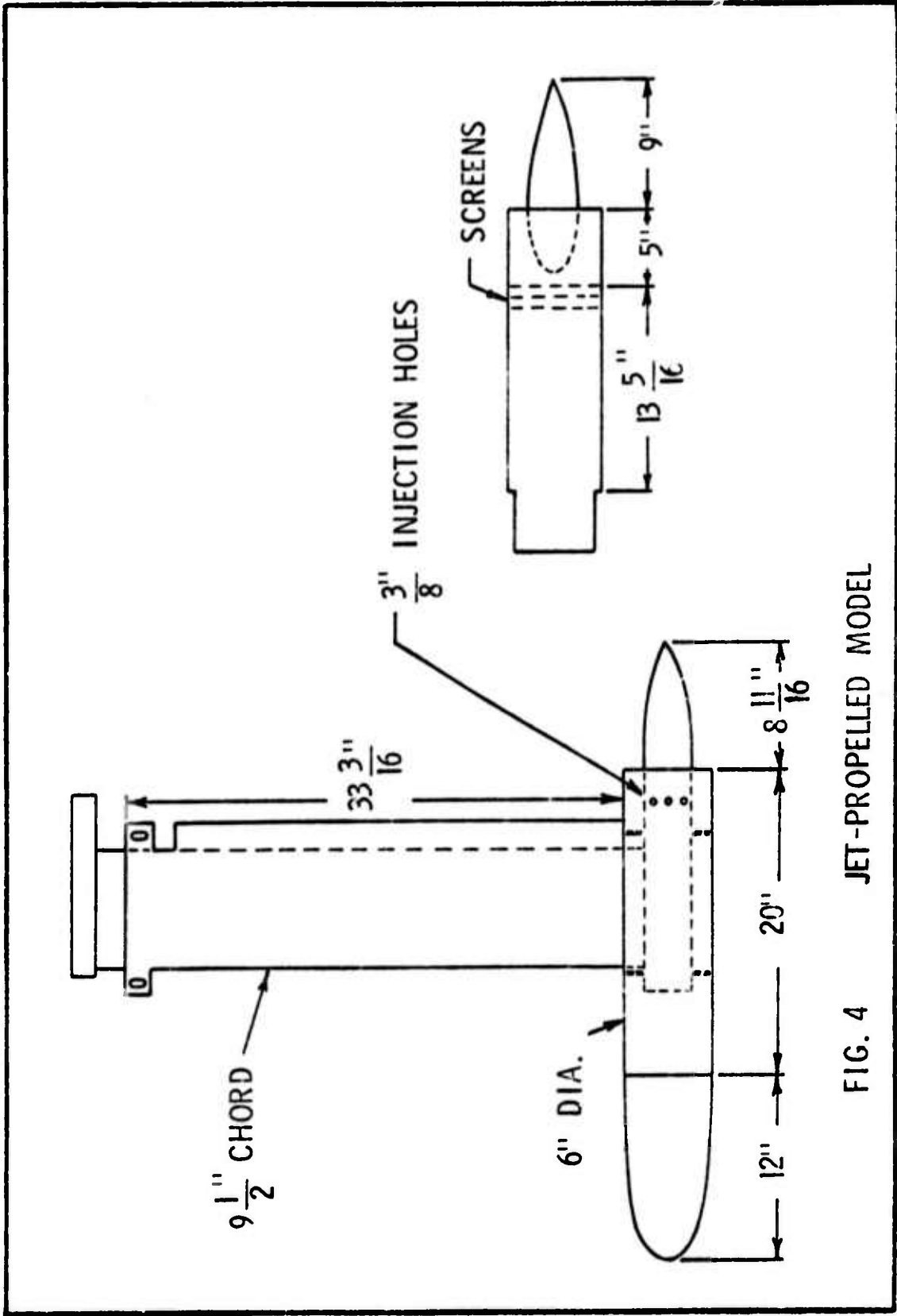


FIG. 4 JET-PROPELLED MODEL

72

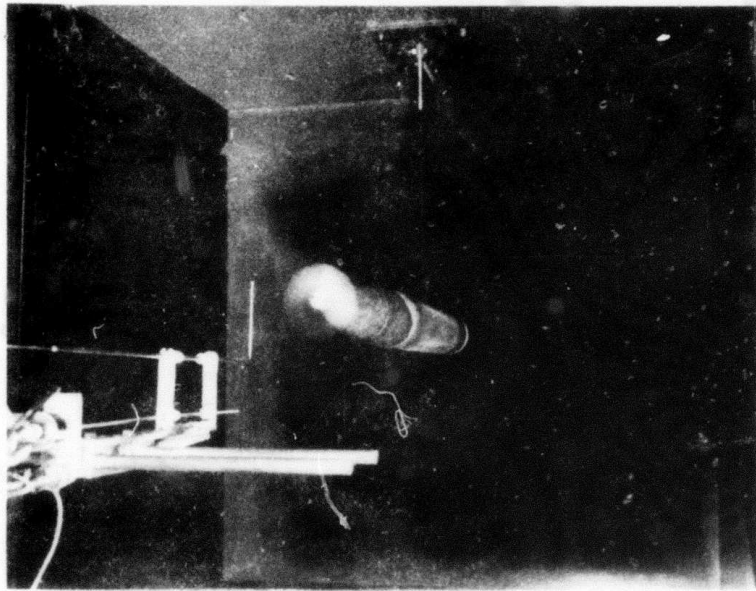


FIG. 5 PHOTOGRAPH OF PROPELLER-DRIVEN MODEL

Model 1210 Standard Straight Probe

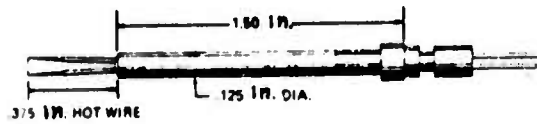


FIG. 6 SINGLE-NORMAL HOT WIRE

HOT WIRE SENSOR

0.00015" Dia.
0.05" Long
Plated Ends



Model 1213 - Sensor 45° to Probe



FIG. 7 SINGLE-YAWED HOT WIRE

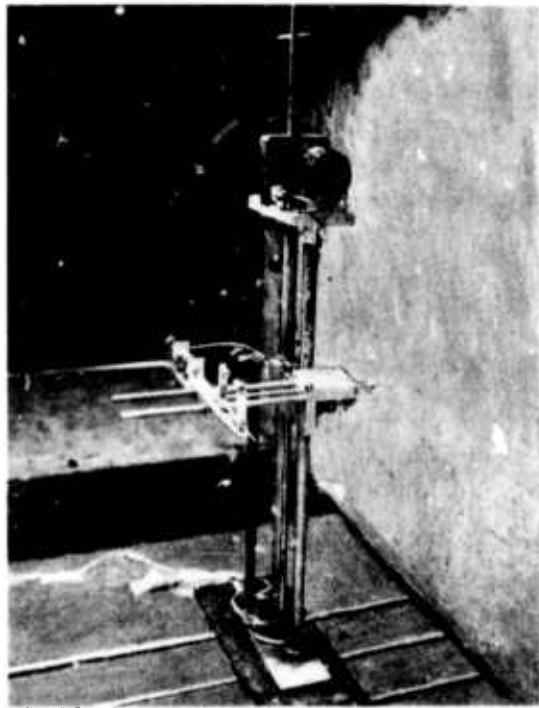


FIG. 8 AUTOMATIC TRAVERSE

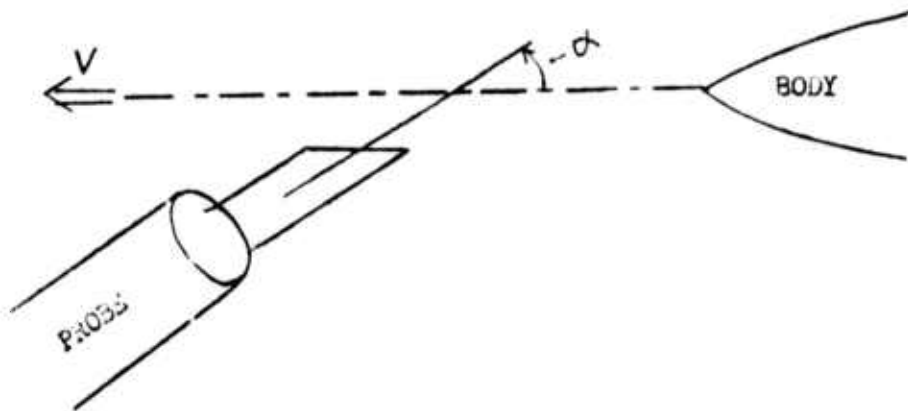


FIG. 9 ANGLE OF ATTACK NOMENCLATURE

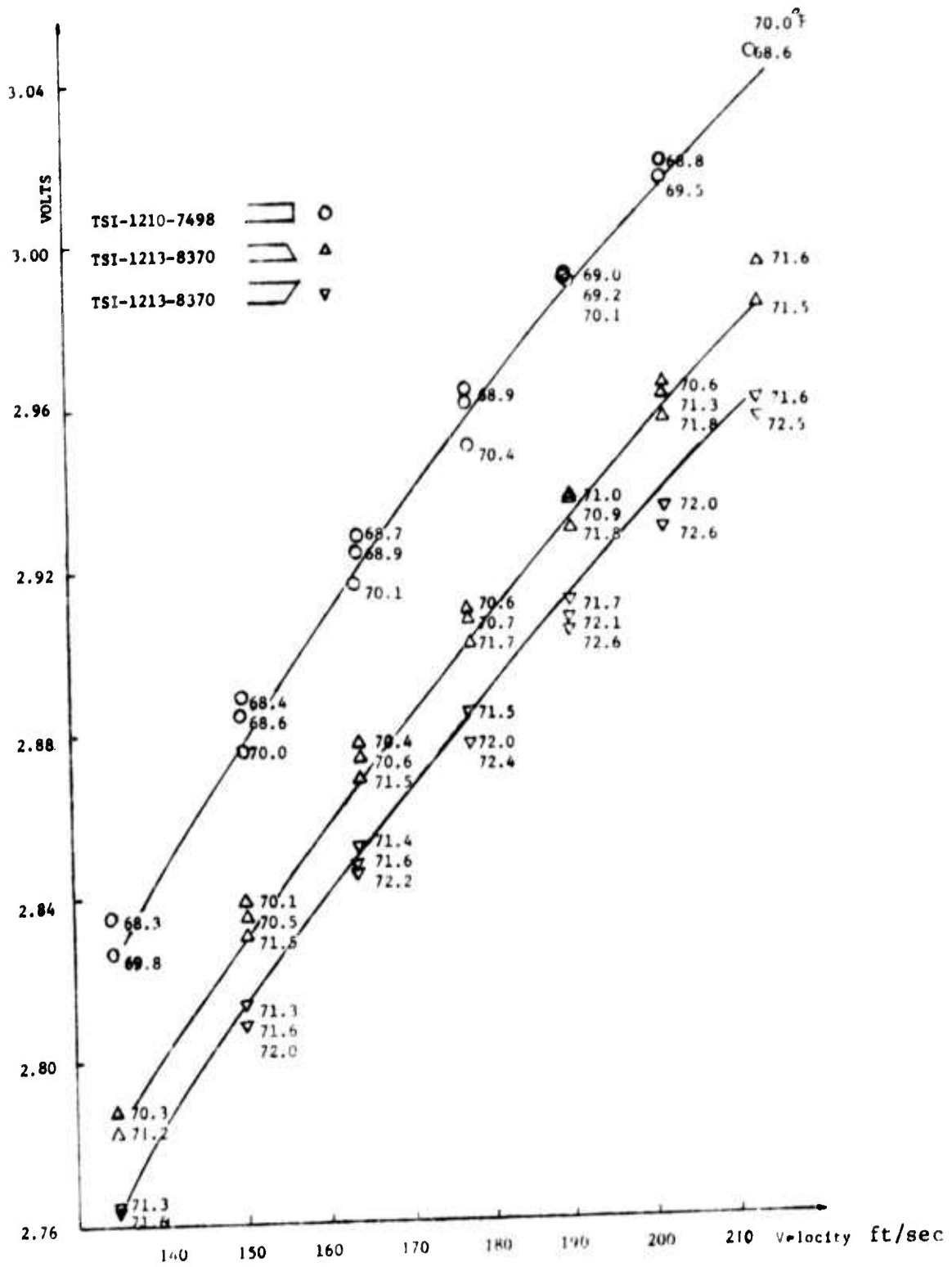


FIG. 10 CALIBRATION CURVE - VELOCITY SENSITIVITY

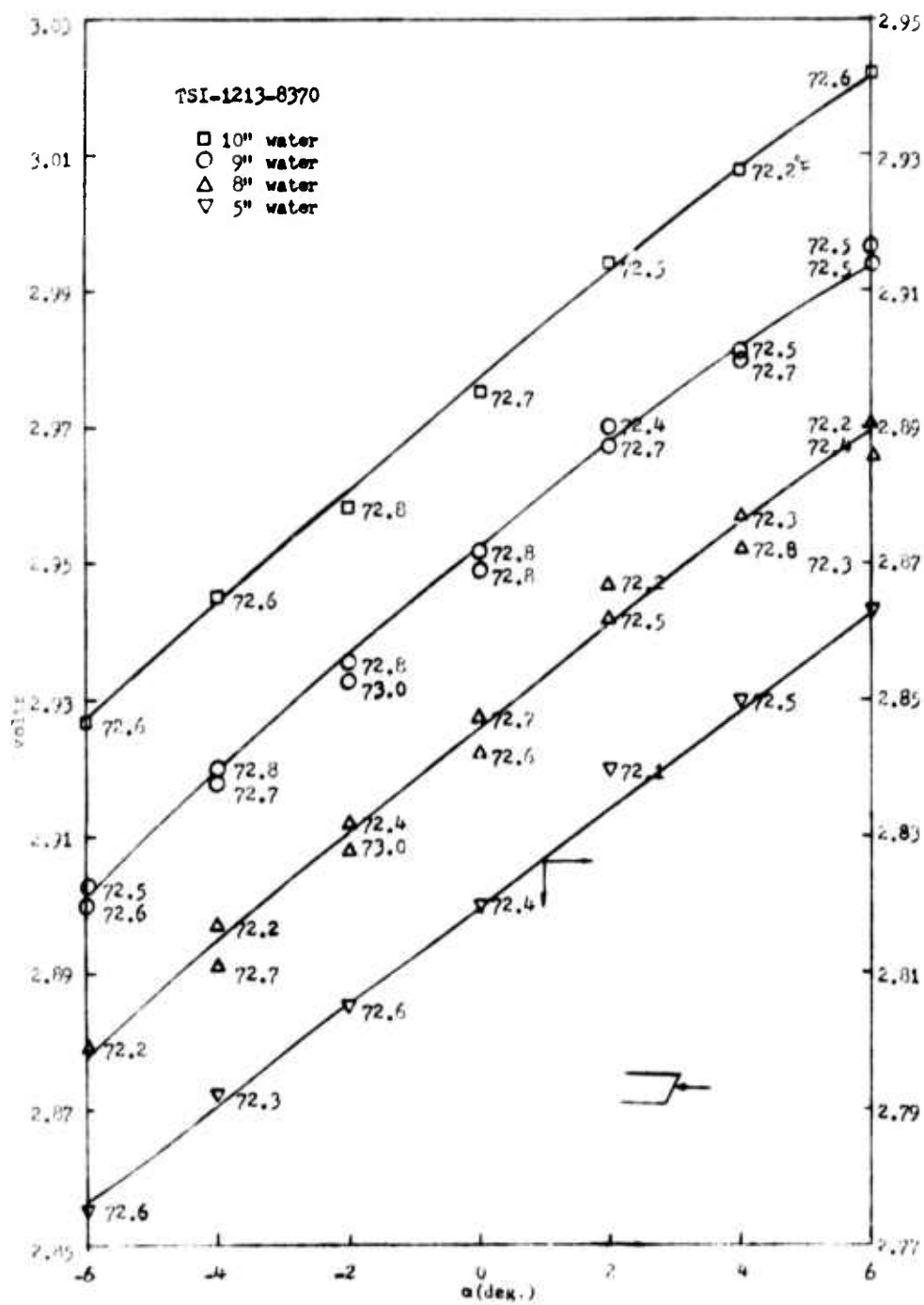


FIG. 11 CALIBRATION CURVE - ANGULAR SENSITIVITY (S_{α})

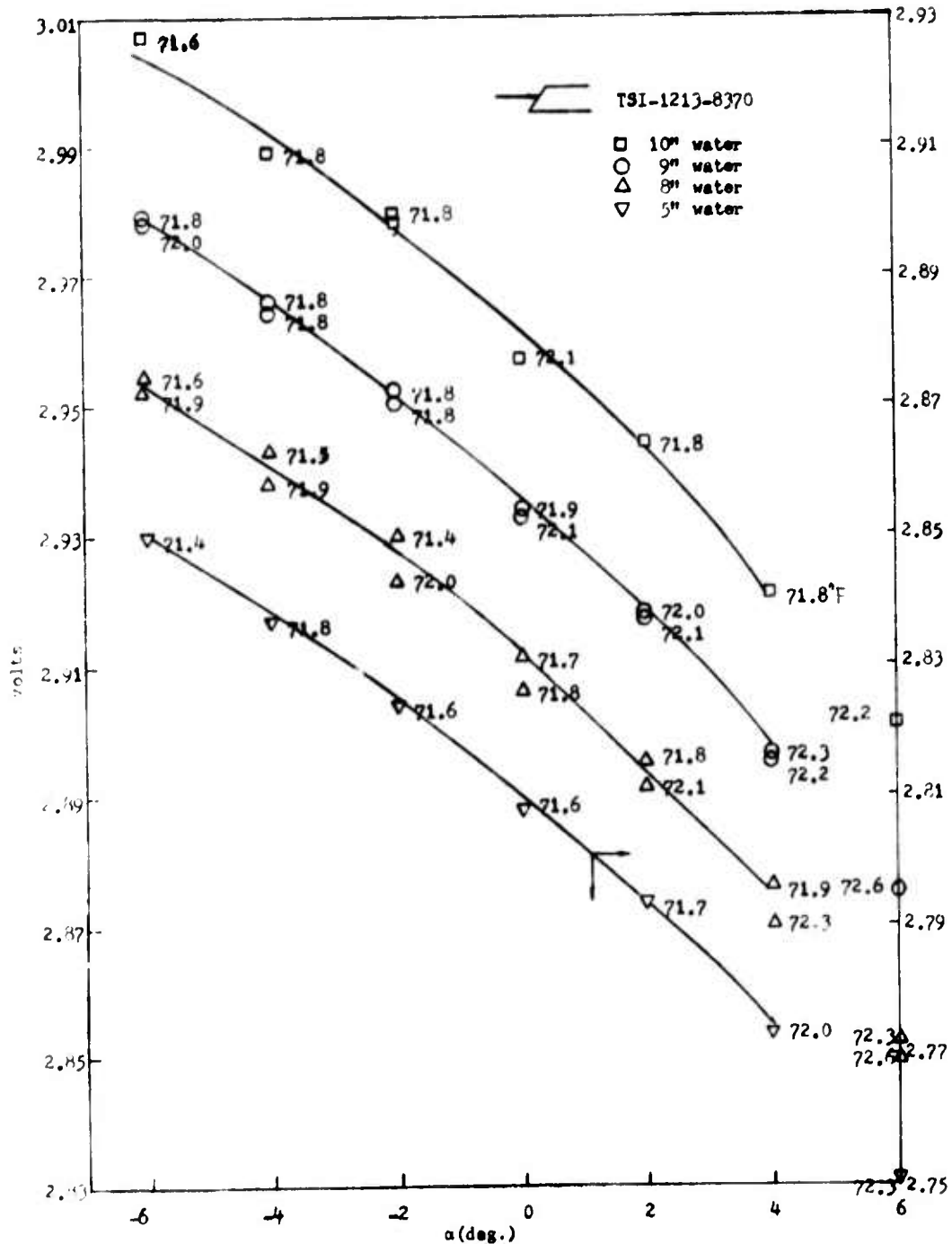


FIG. 12 CALIBRATION CURVE - ANGULAR SENSITIVITY ($S_{v_{\alpha}}$)

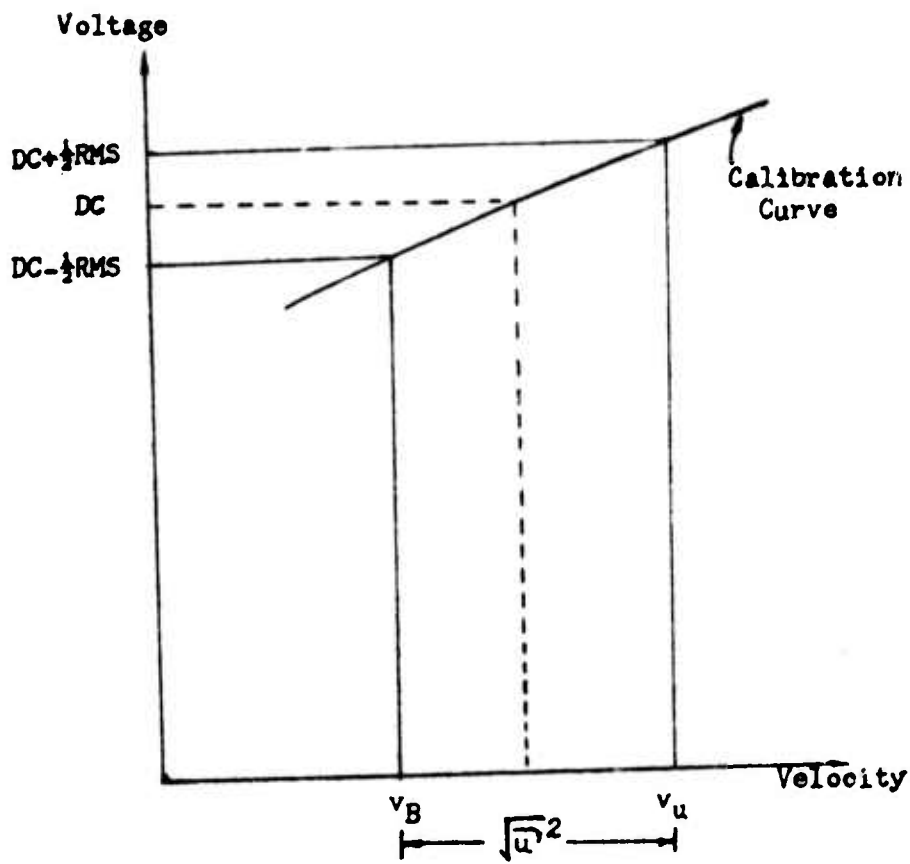


FIG. 13 SCHEMATIC ILLUSTRATION OF EVALUATION OF AXIAL TURBULENCE INTENSITY

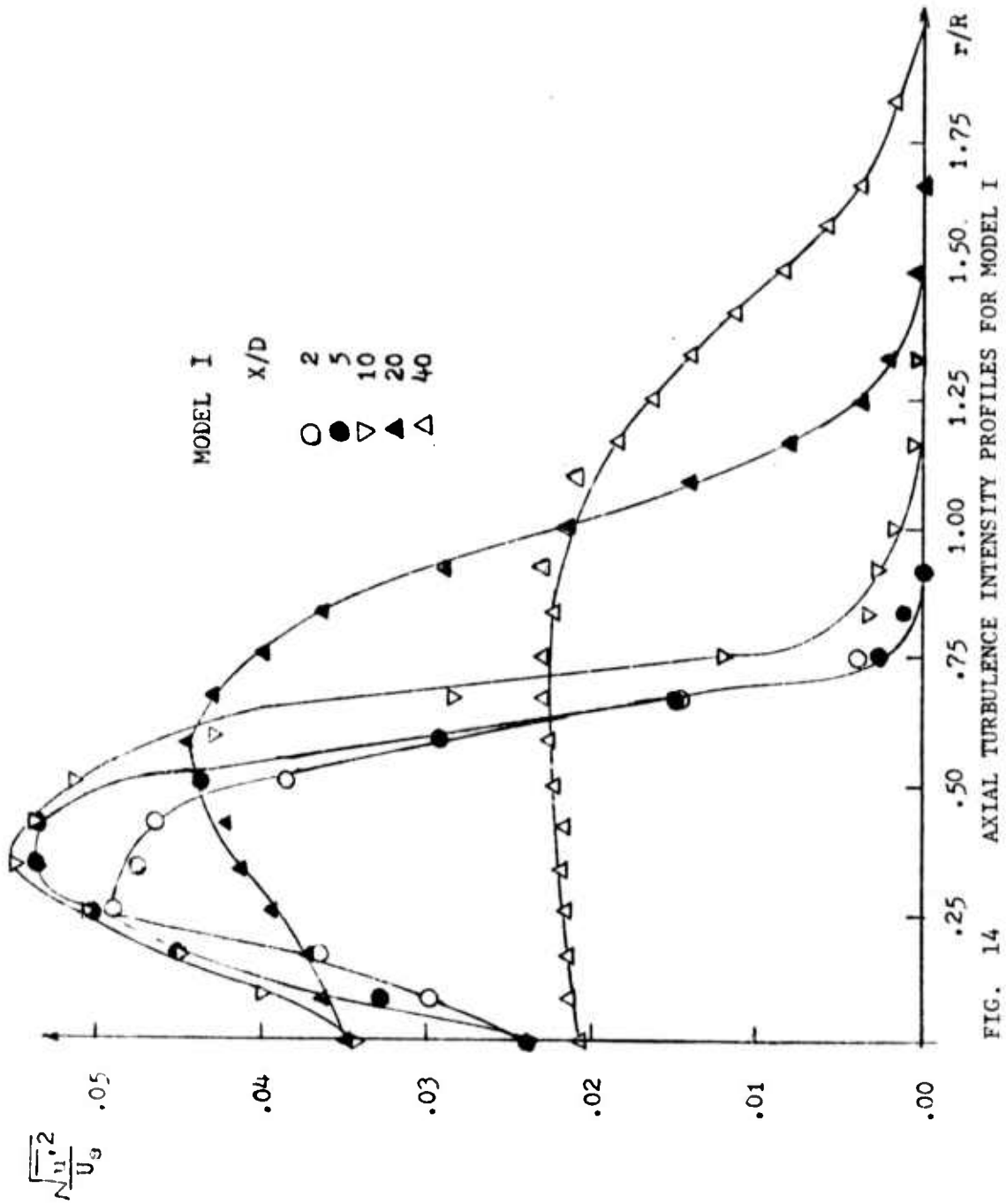
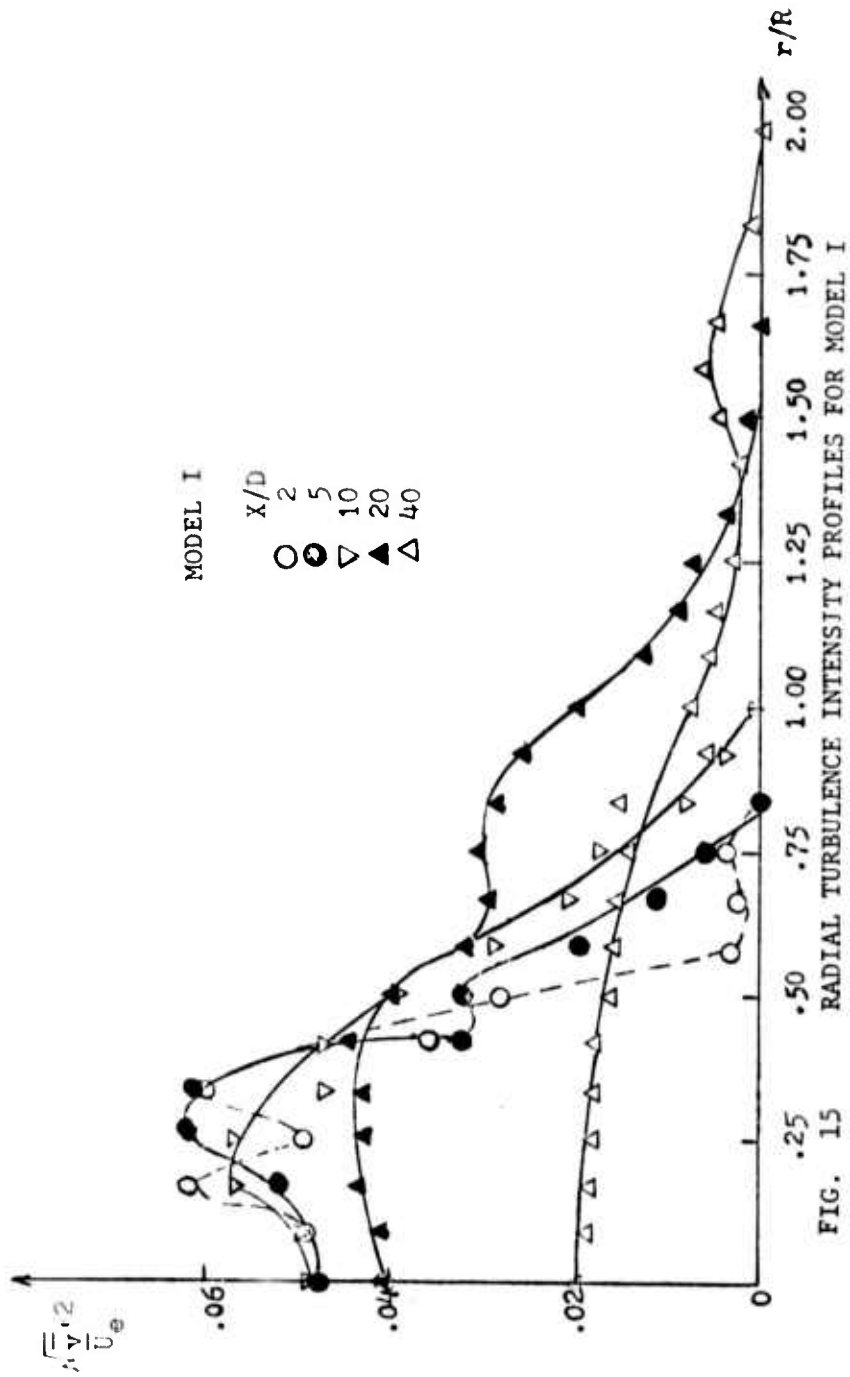


FIG. 14



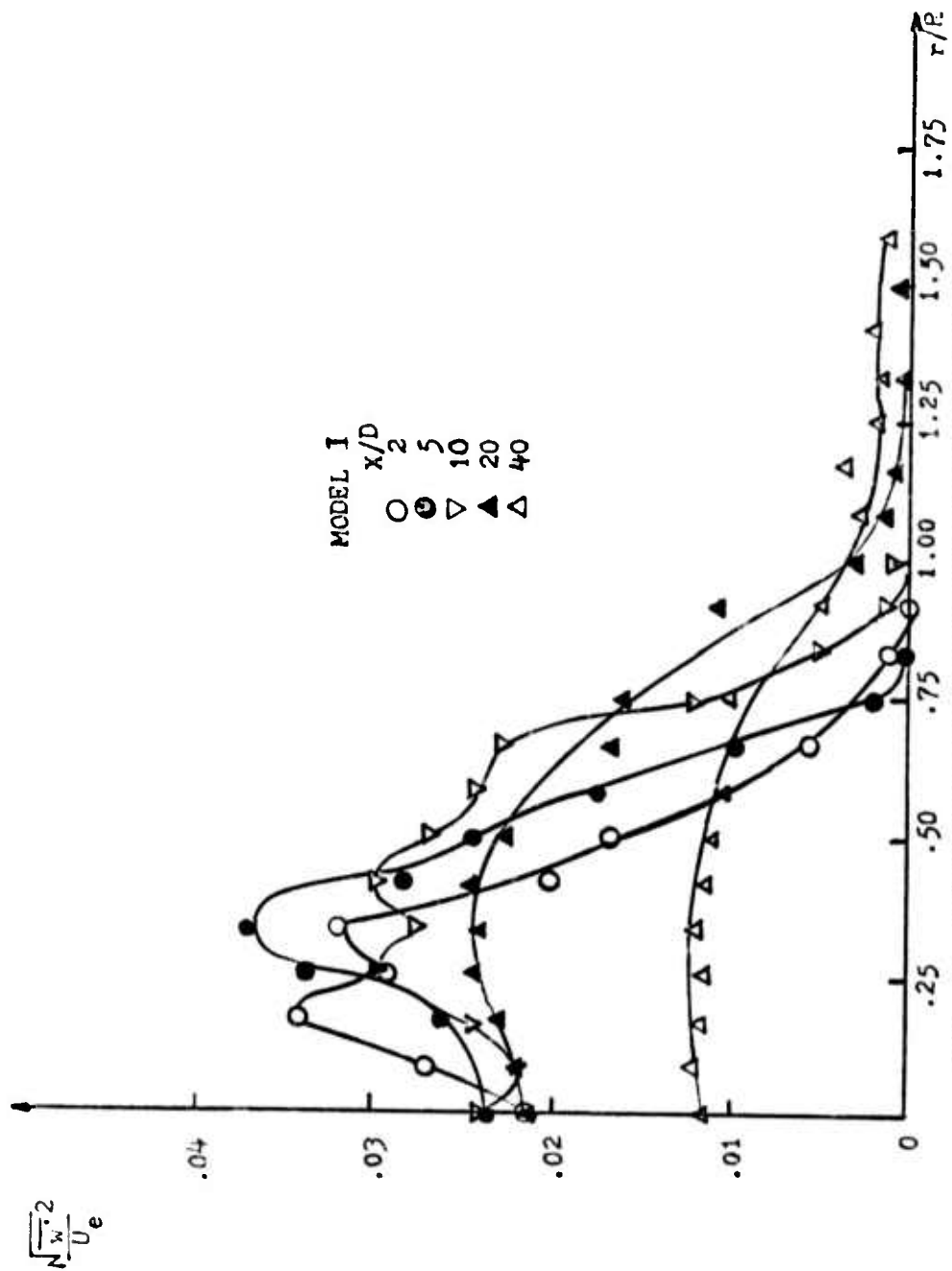


FIG. 16 TANGENTIAL TURBULENCE INTENSITY PROFILES FOR MODEL I

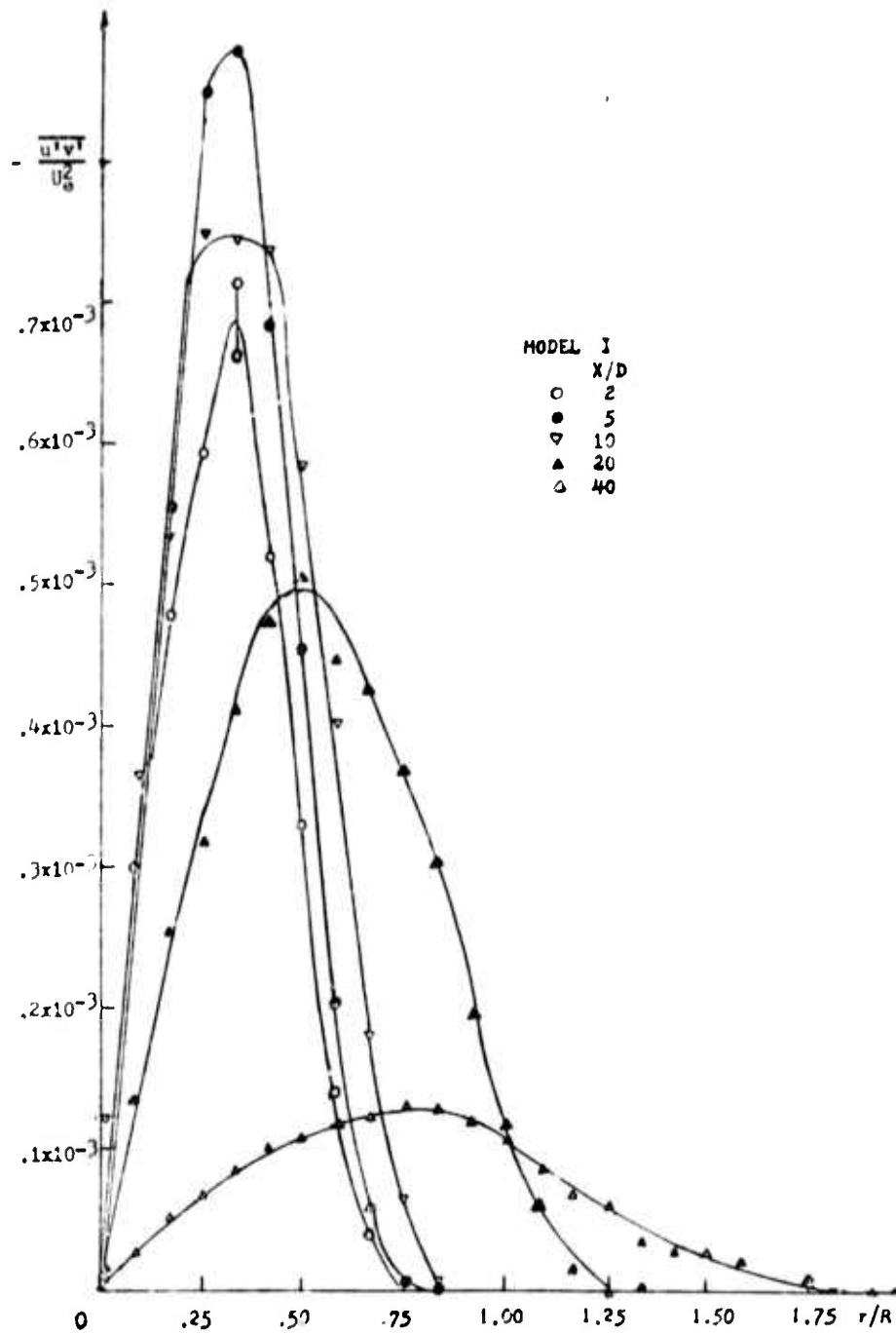


FIG. 17 RADIAL SHEAR STRESS PROFILES FOR MODEL I

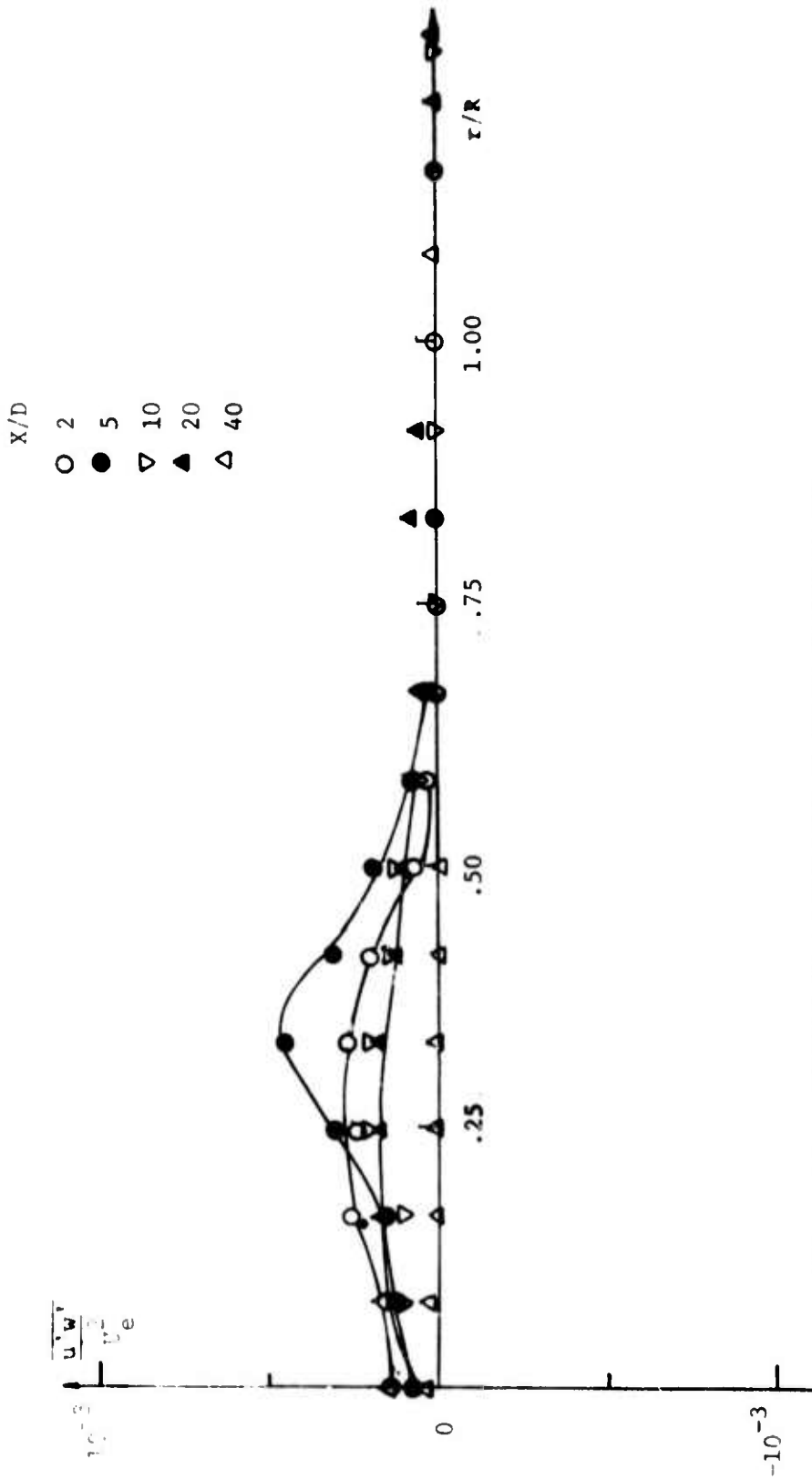


FIG. 18 TANGENTIAL SHEAR STRESS PROFILES FOR MODEL I

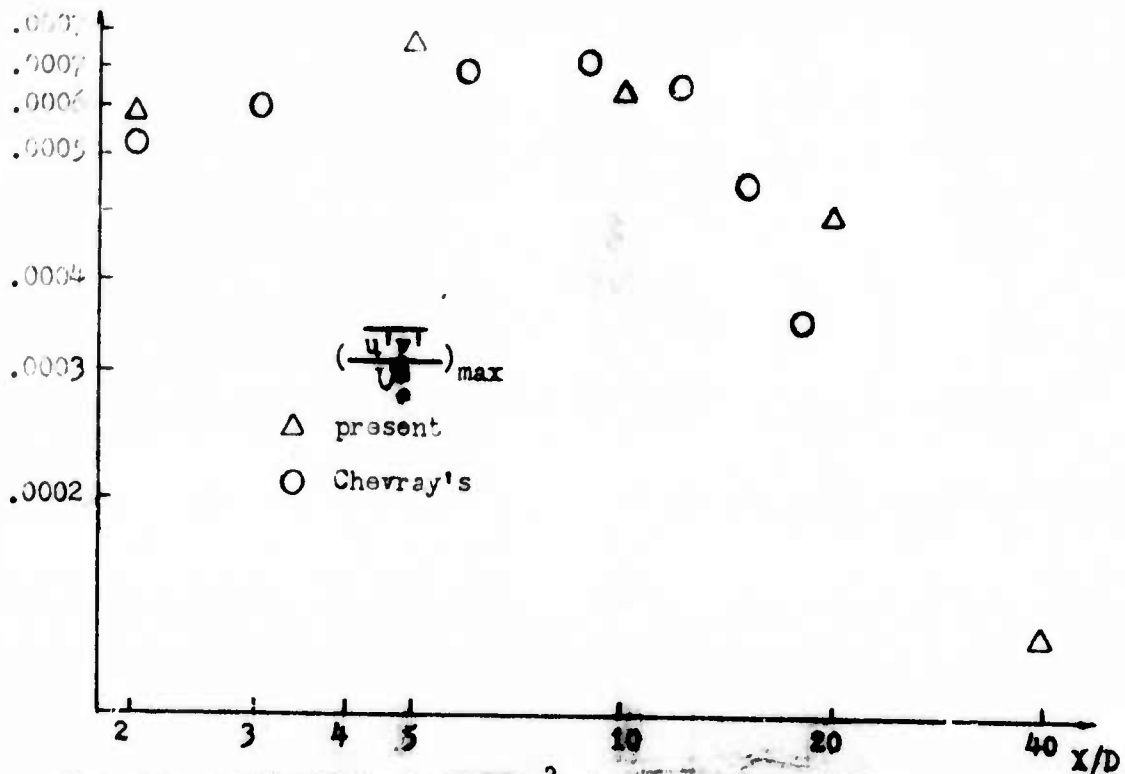


FIG. 19a COMPARISON OF $(\frac{u'v'}{U^2})_{max}$ FOR MODEL B AND CHEVRAY'S MODEL

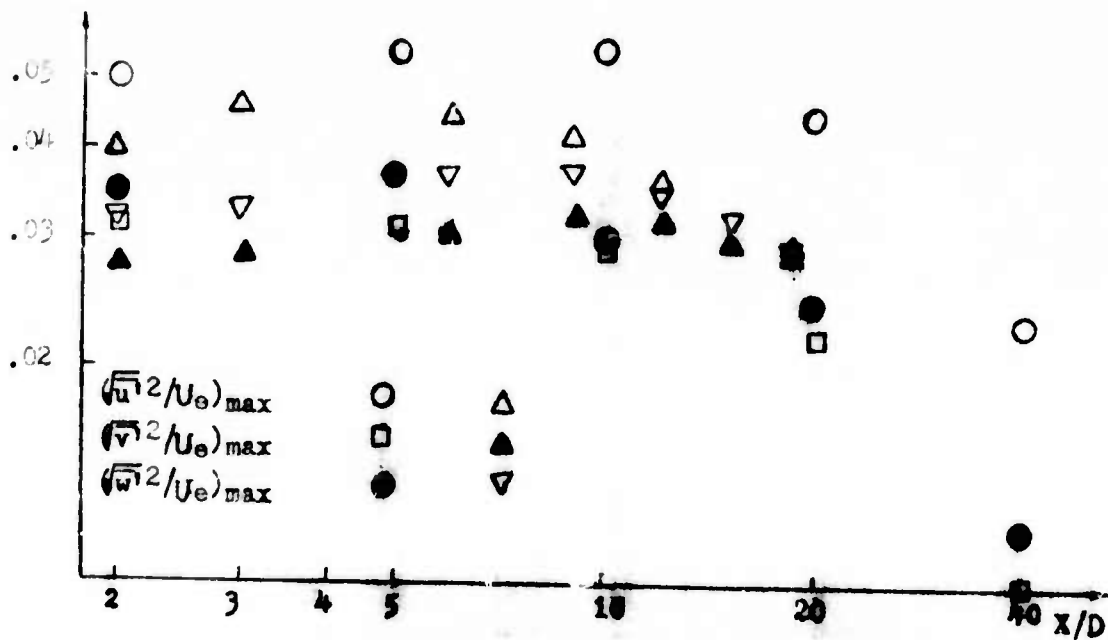


FIG. 19b COMPARISON OF PEAK TURBULENCE INTENSITIES FOR MODEL I AND CHEVRAY'S MODEL

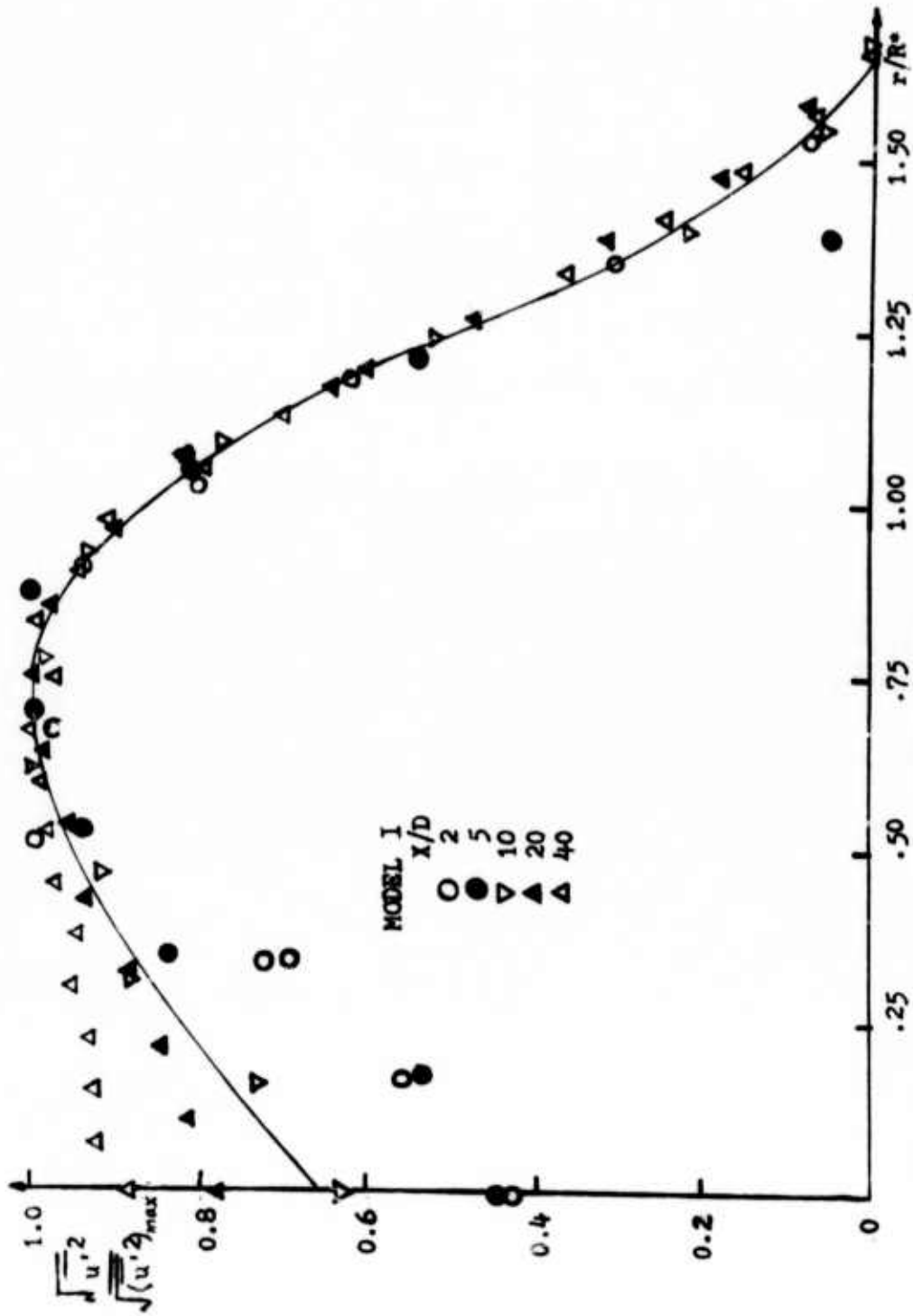
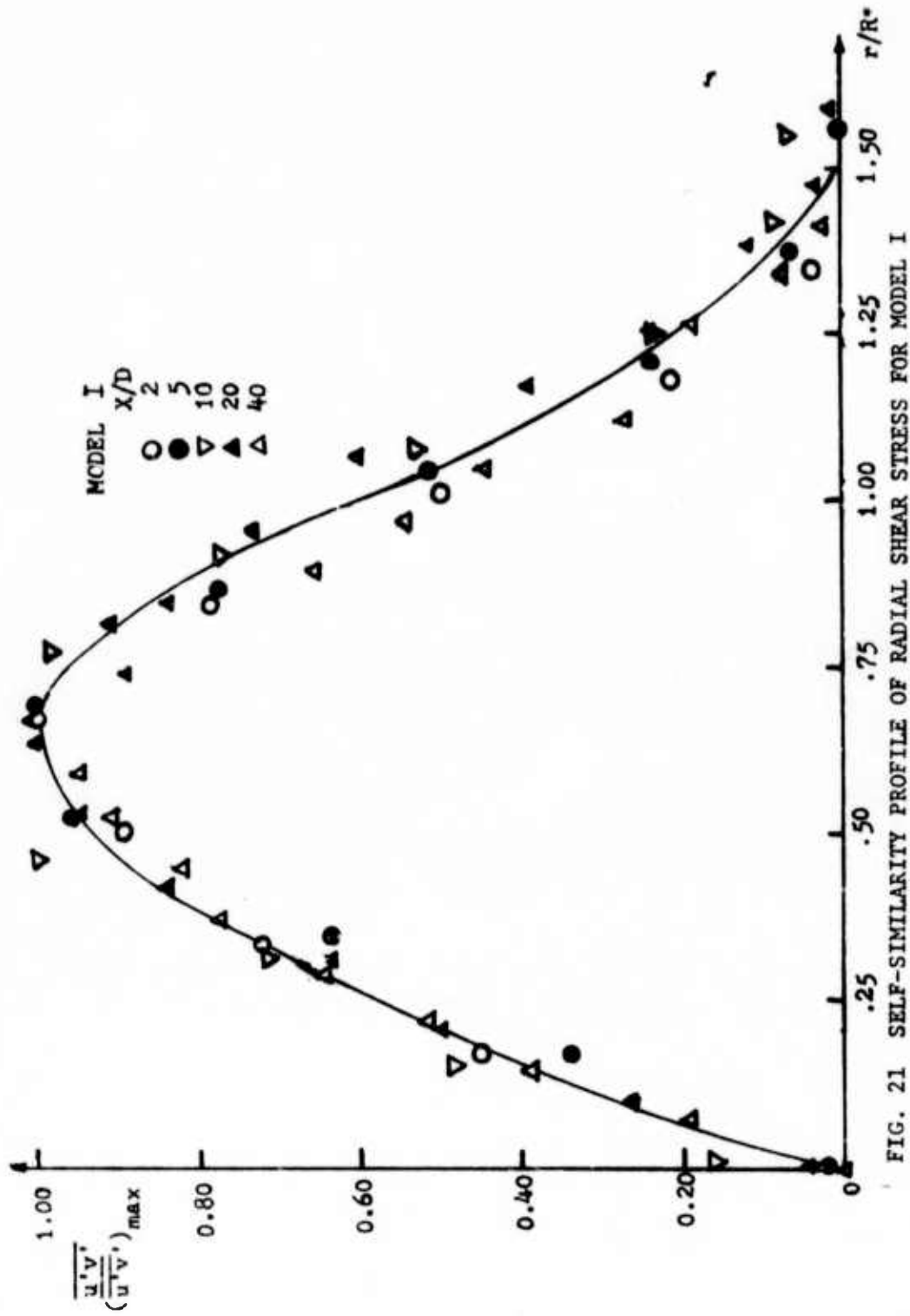


FIG. 20 SELF-SIMILARITY PROFILES OF AXIAL TURBULENCE INTENSITY FOR MODEL I



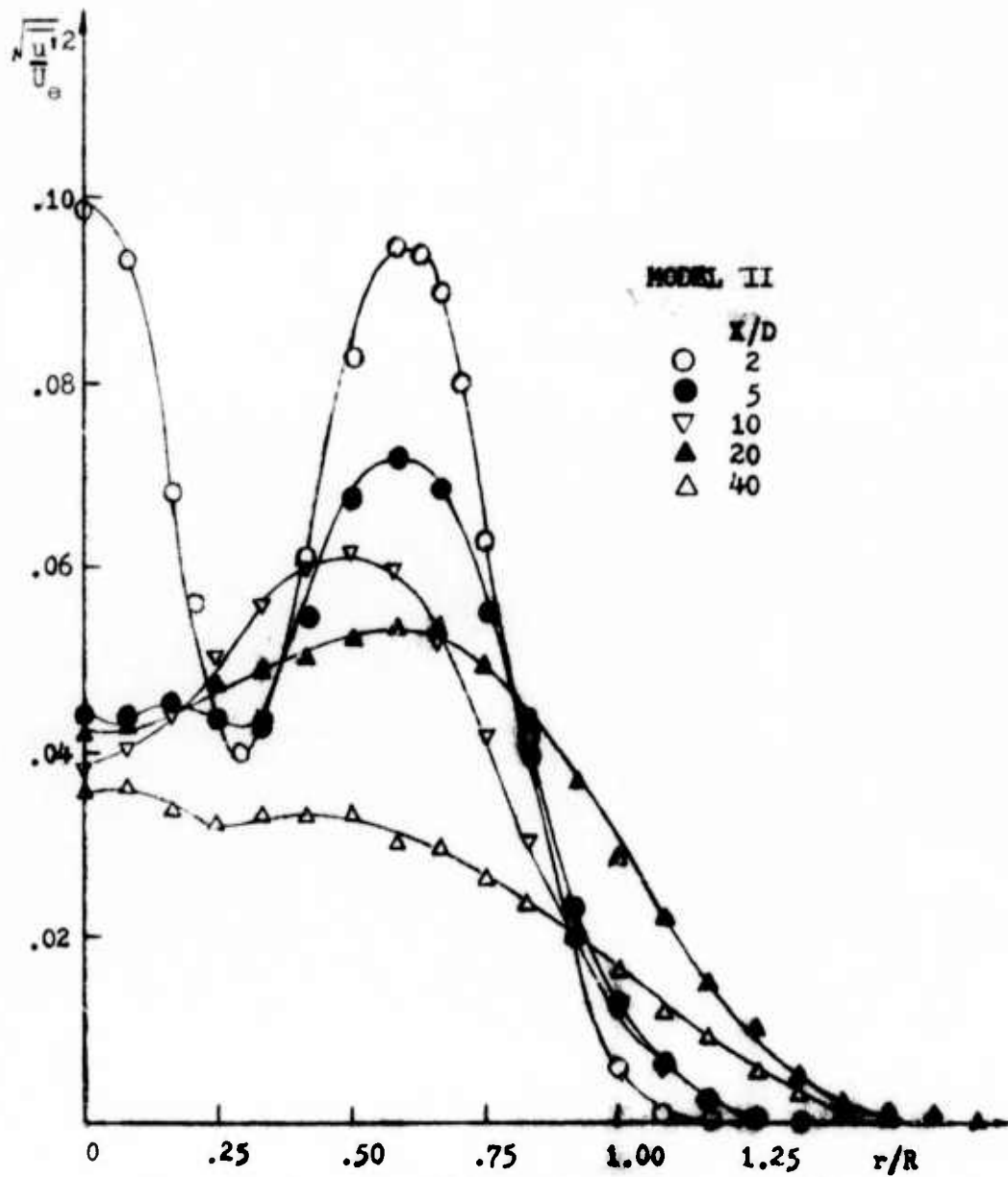


FIG. 22 AXIAL TURBULENCE INTENSITY PROFILES FOR MODEL II

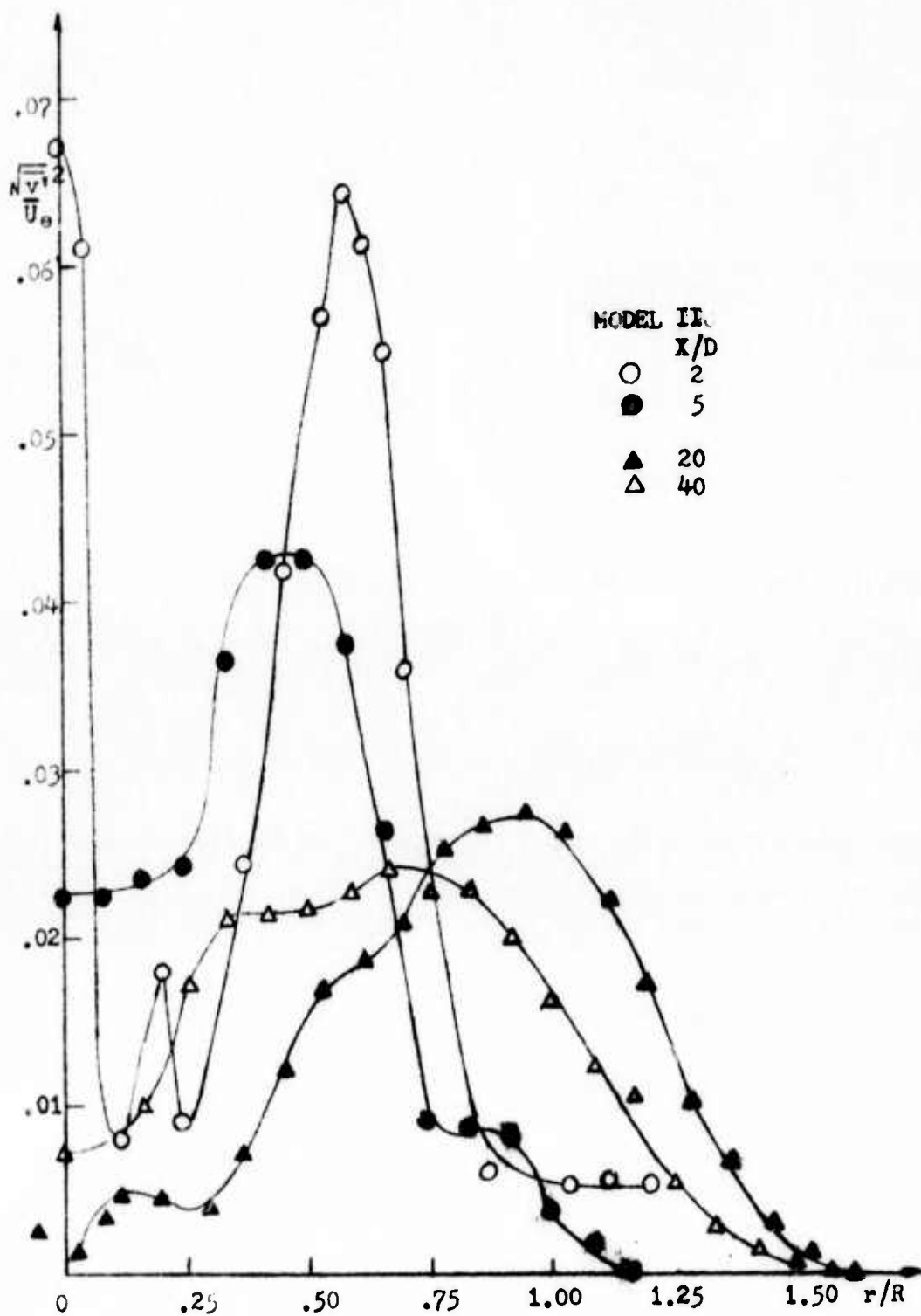


FIG. 23 RADIAL TURBULENCE INTENSITY PROFILES FOR MODEL II

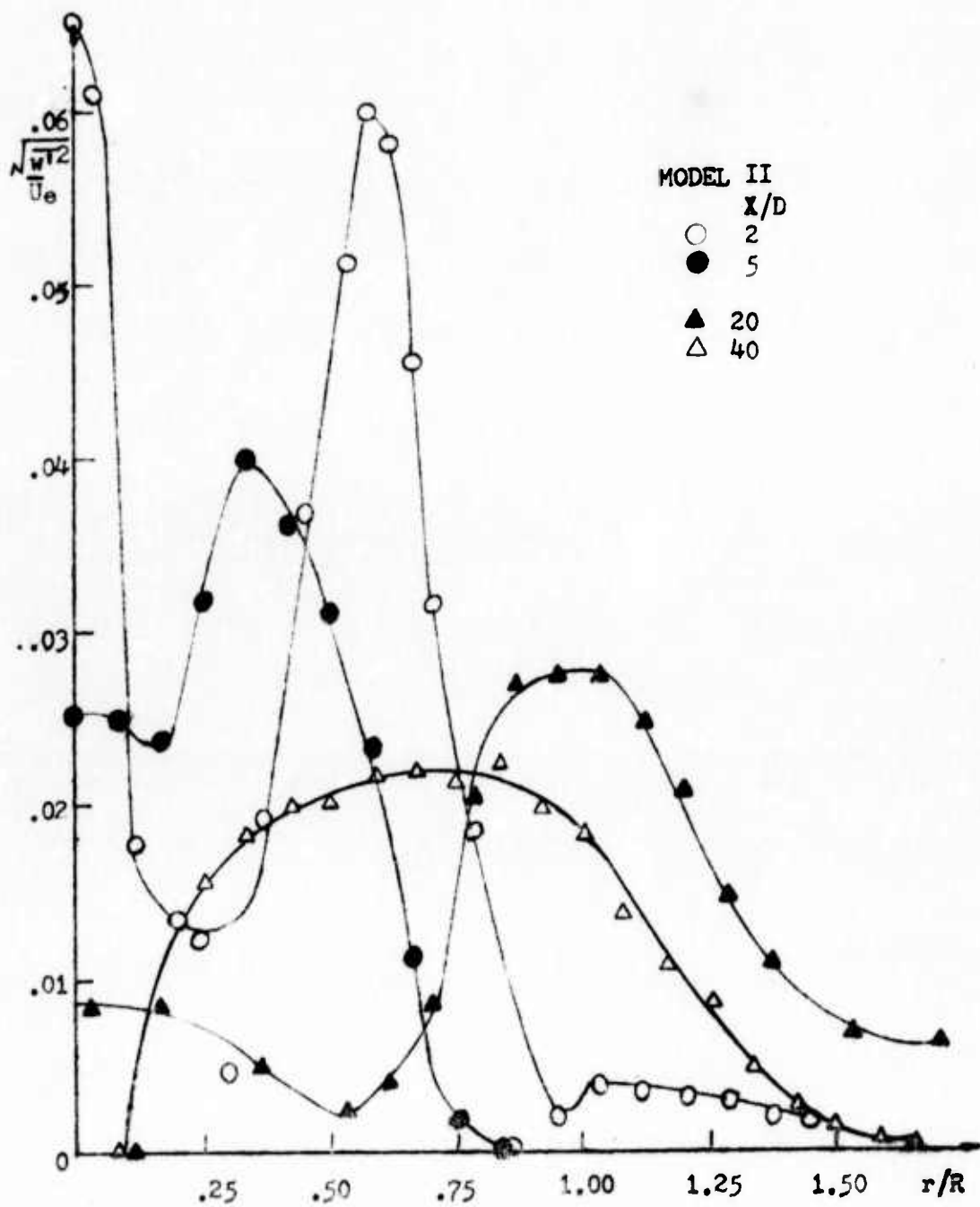


FIG. 24 TANGENTIAL TURBULENCE INTENSITY PROFILES FOR MODEL II

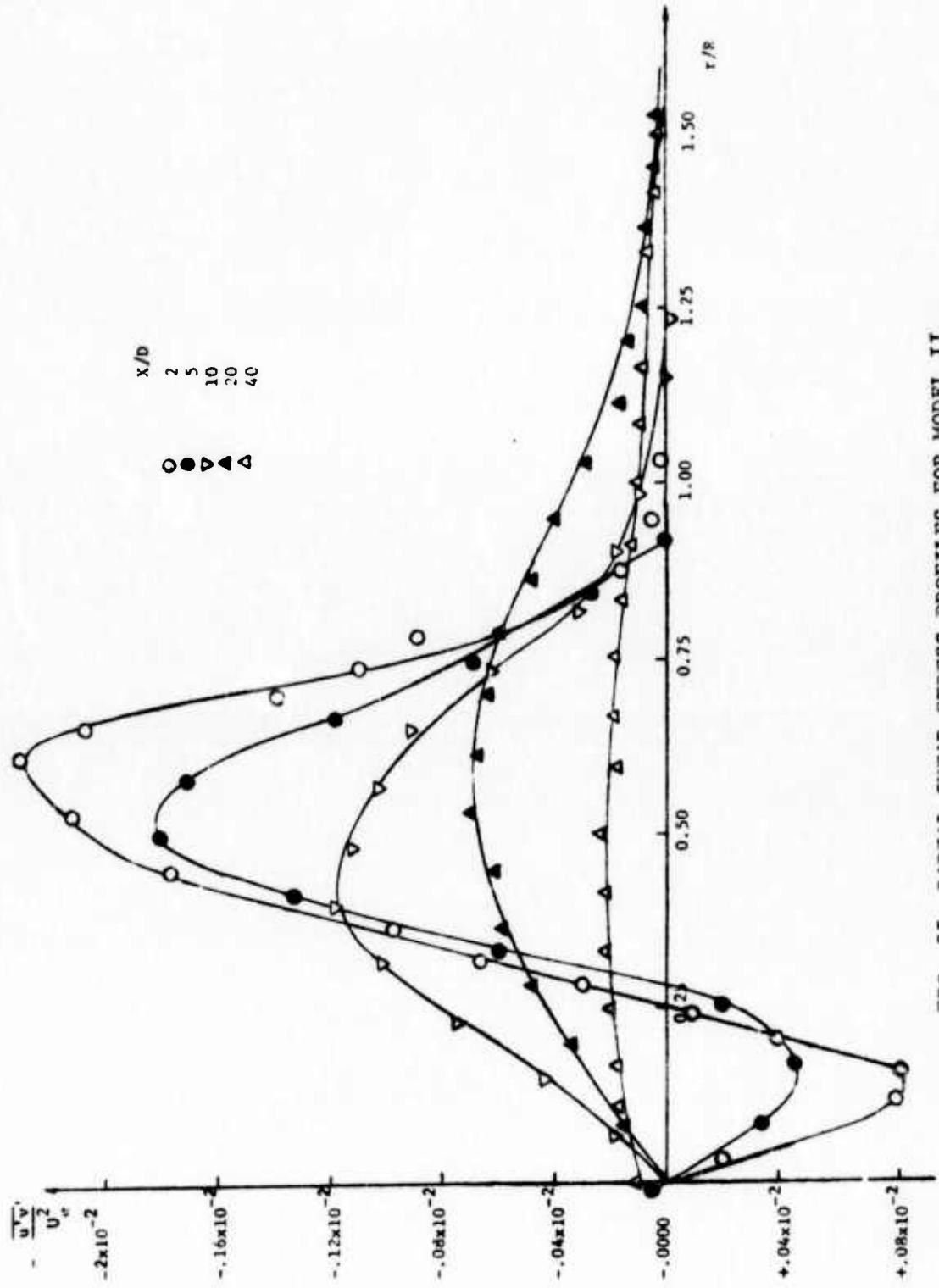


FIG. 25 RADIAL SHEAR STRESS PROFILES FOR MODEL II

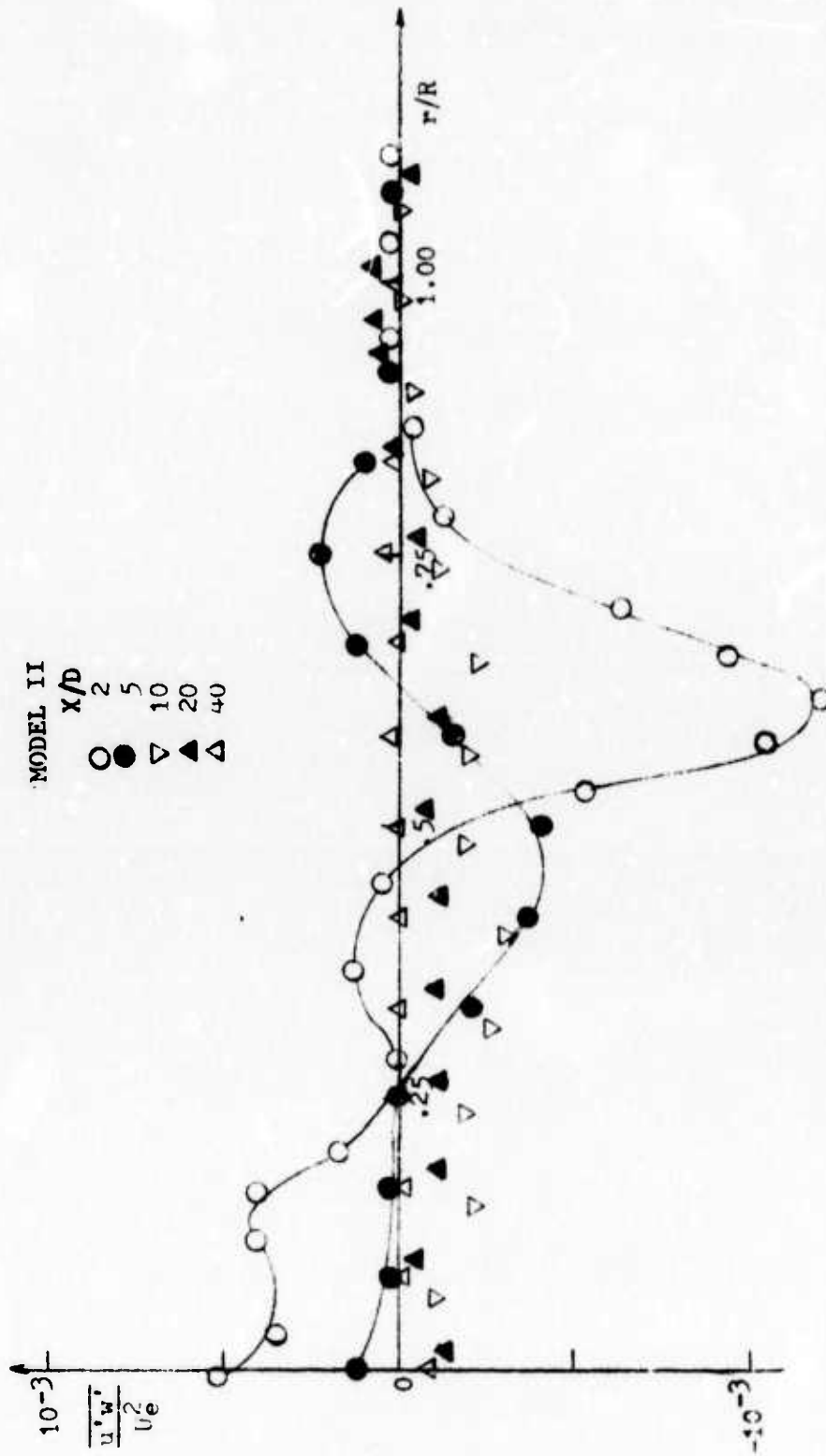


FIG. 26 TANGENTIAL SHEAR STRESS PROFILES FOR MODEL II

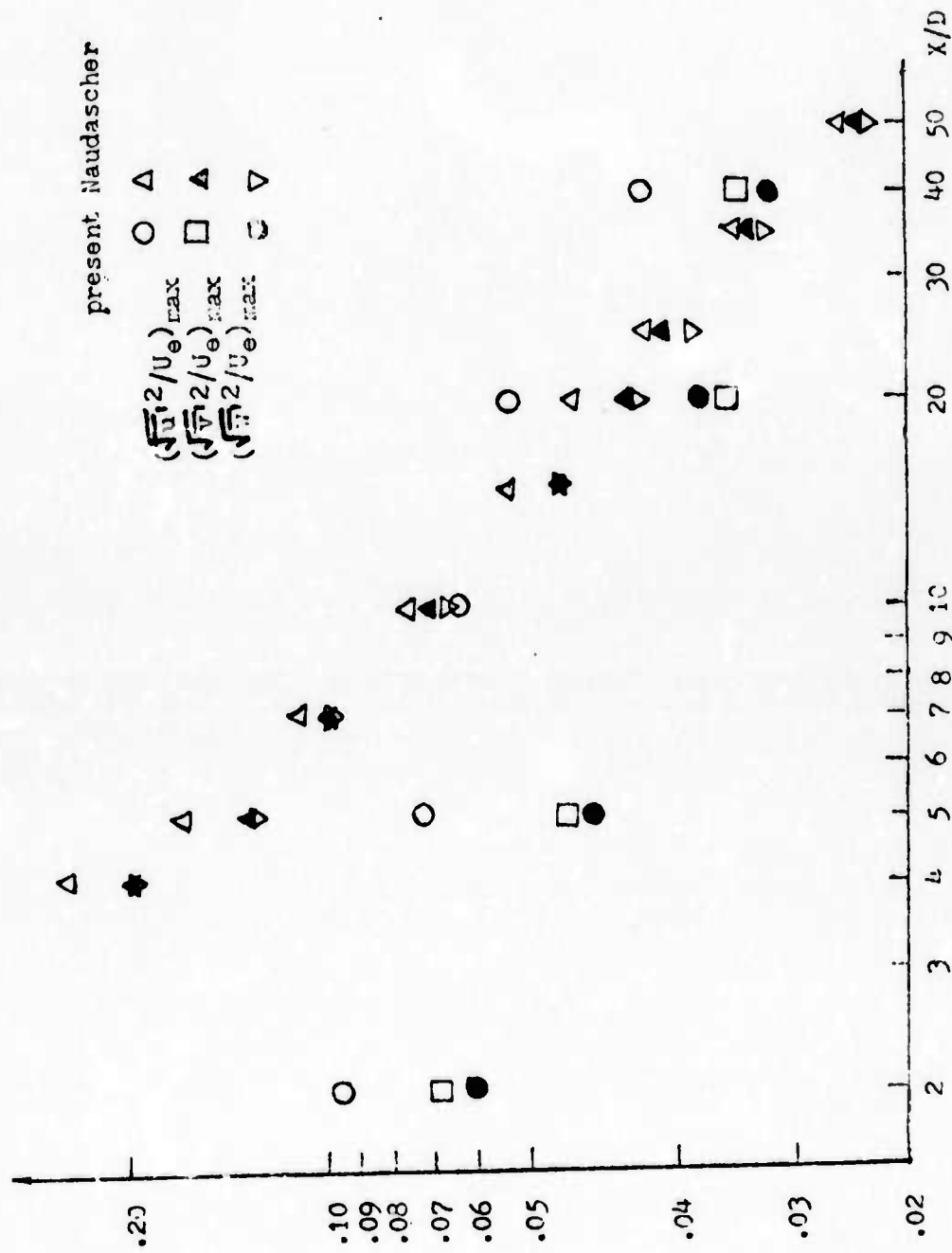


FIG. 27 COMPARISON OF THE RESULTS FOR MODEL II AND NAUDASCHER'S MODEL

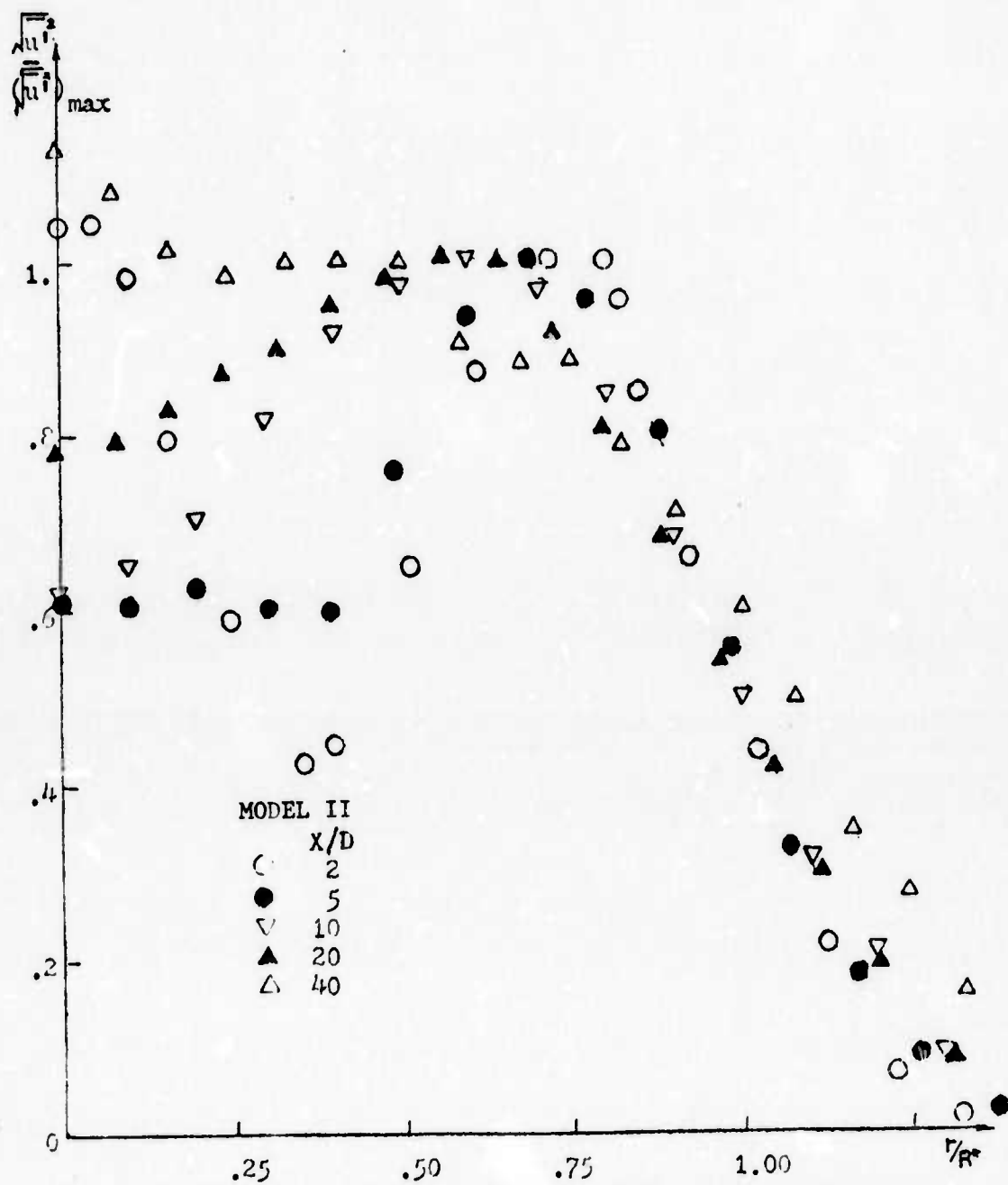


FIG. 28 SELF-SIMILARITY PROFILE OF AXIAL TURBULENCE INTENSITY
FOR MODEL II

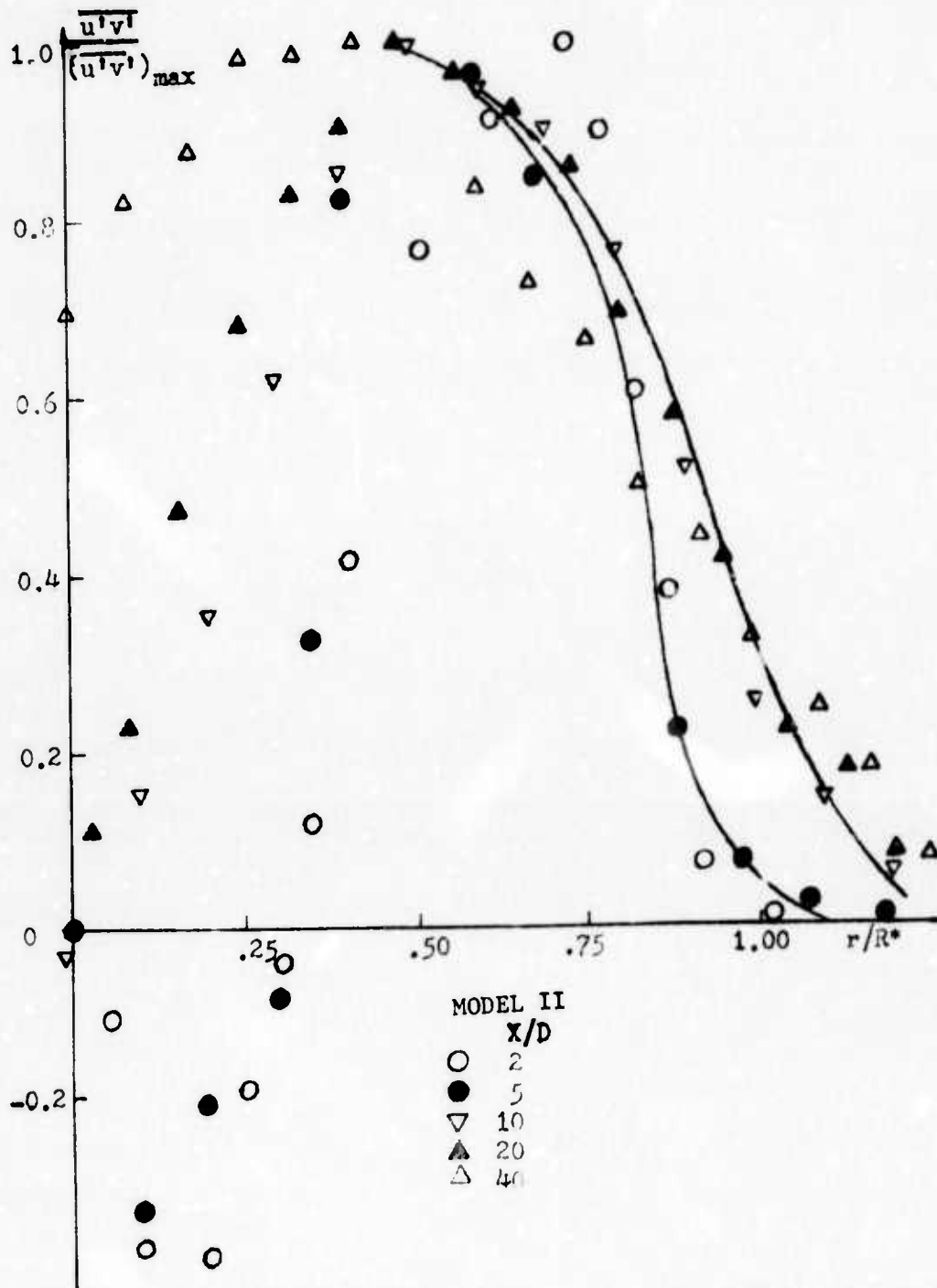


FIG. 29 SELF-SIMILARITY PROFILE OF RADIAL SHEAR STRESS FOR MODEL II

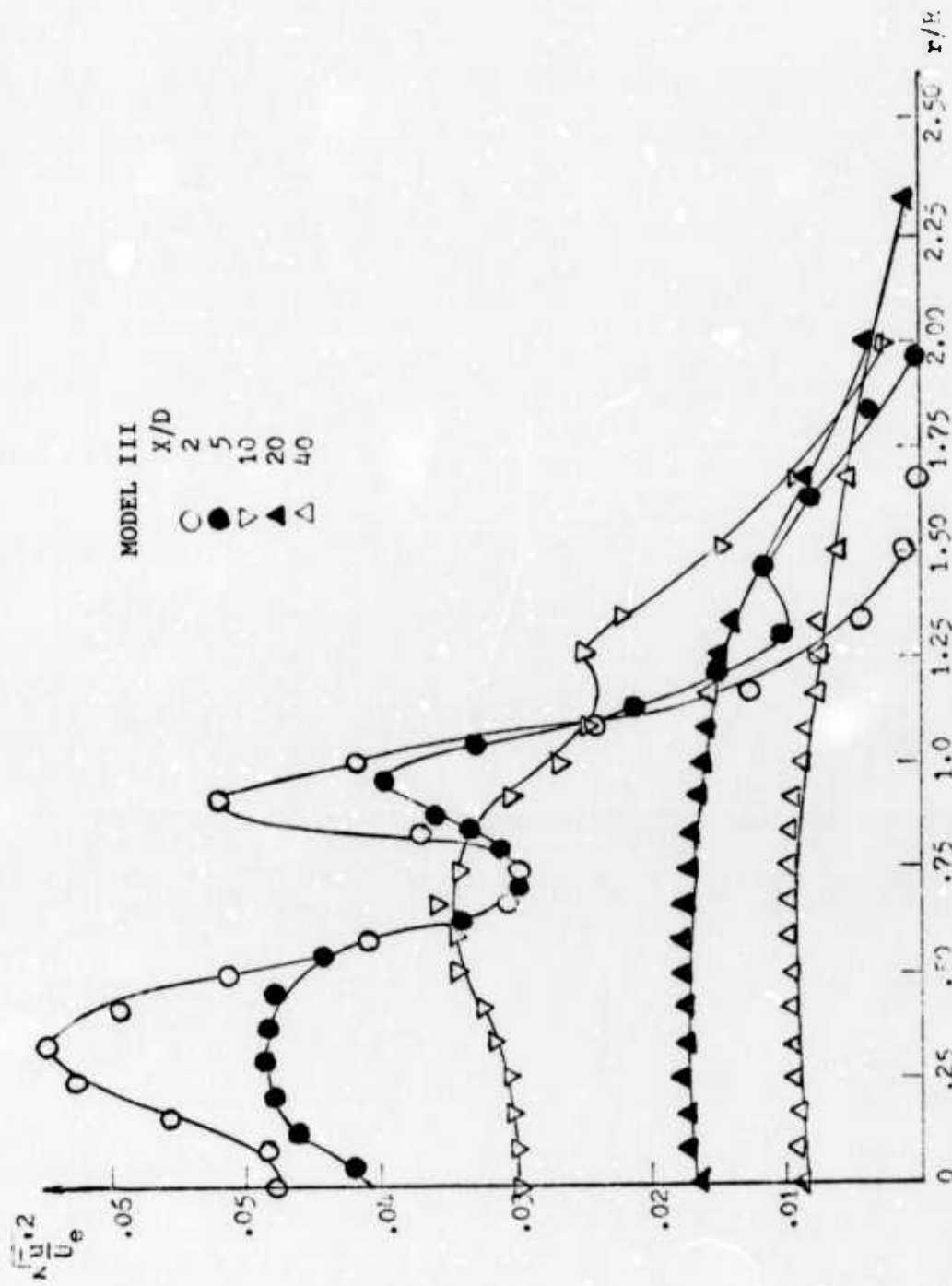


FIG. 30 AXIAL TURBULENCE INTENSITY PROFILES FOR MODEL III

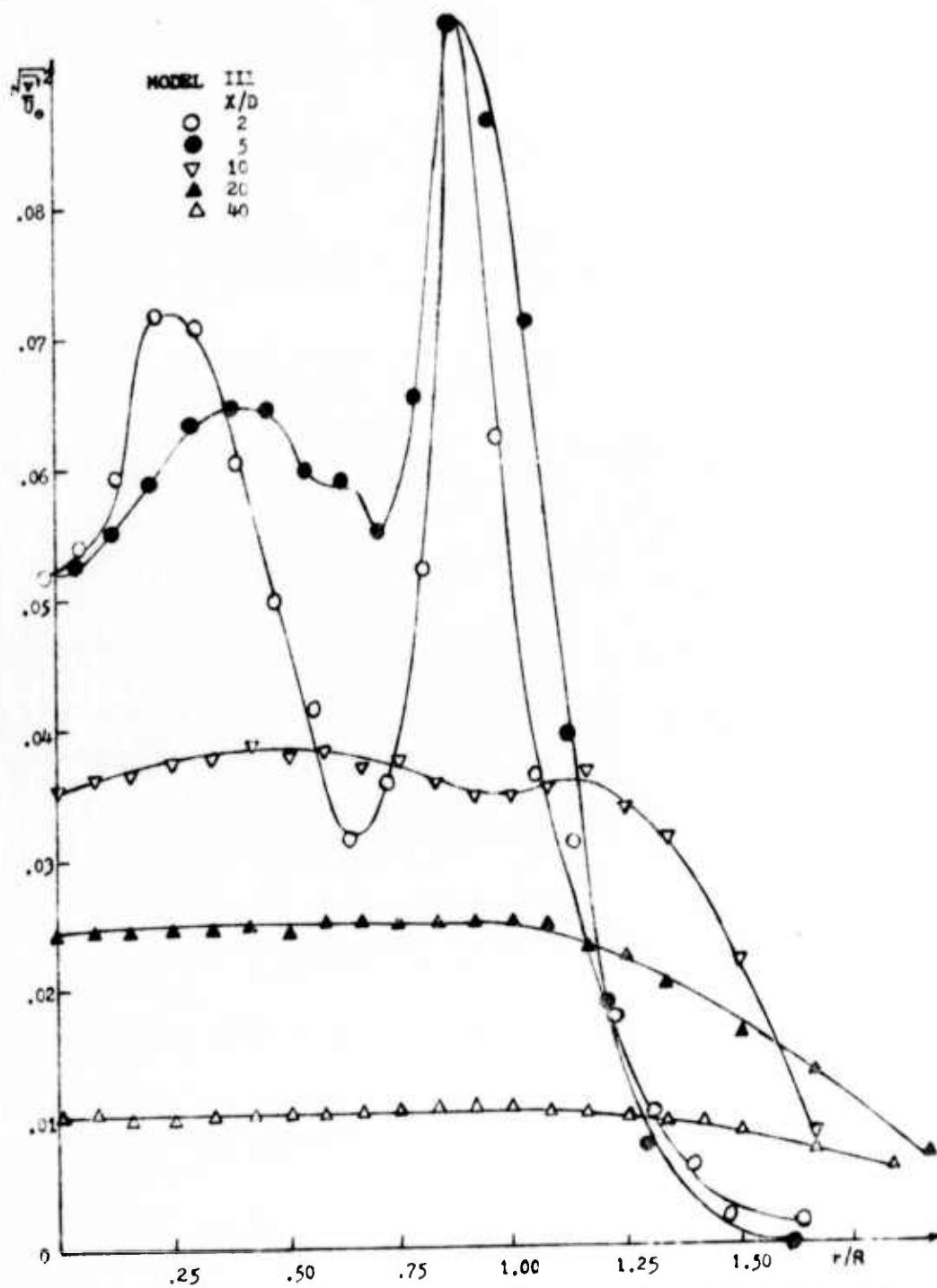


FIG. 31 RADIAL TURBULENCE INTENSITY PROFILES FOR MODEL III

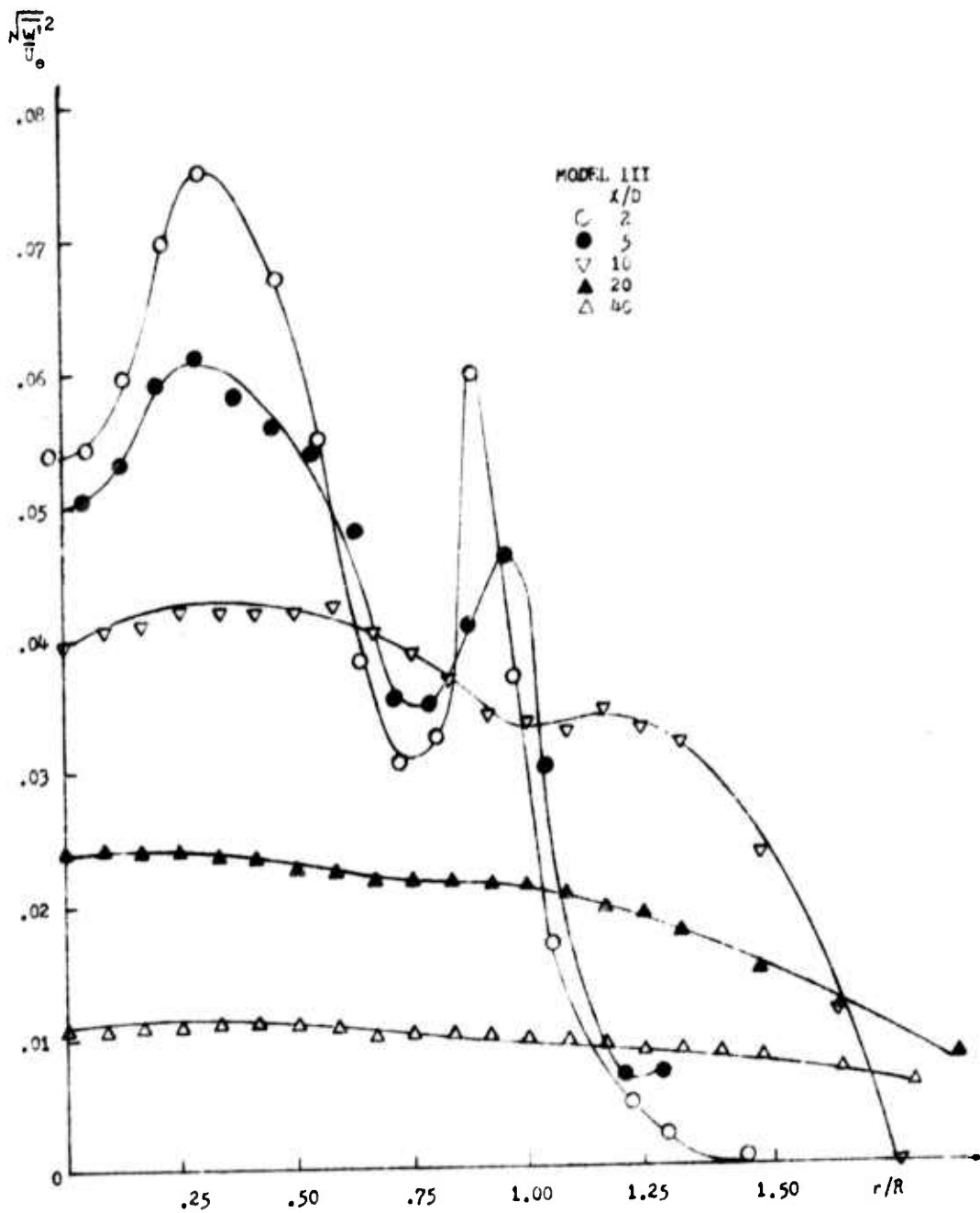


FIG. 32 TANGENTIAL TURBULENCE INTENSITY PROFILES FOR MODEL III

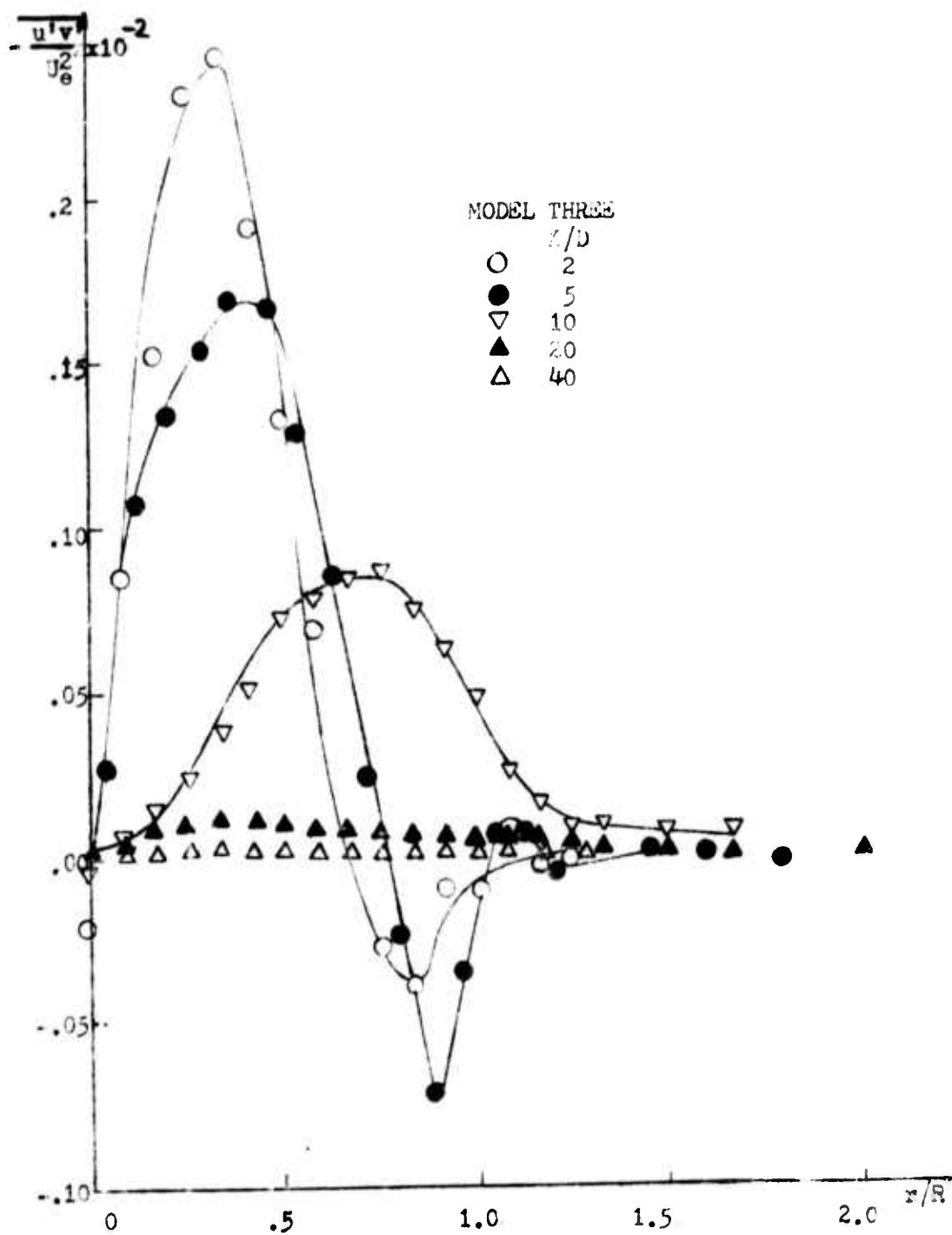


FIG. 33 RADIAL SHEAR STRESS PROFILES FOR MODEL III

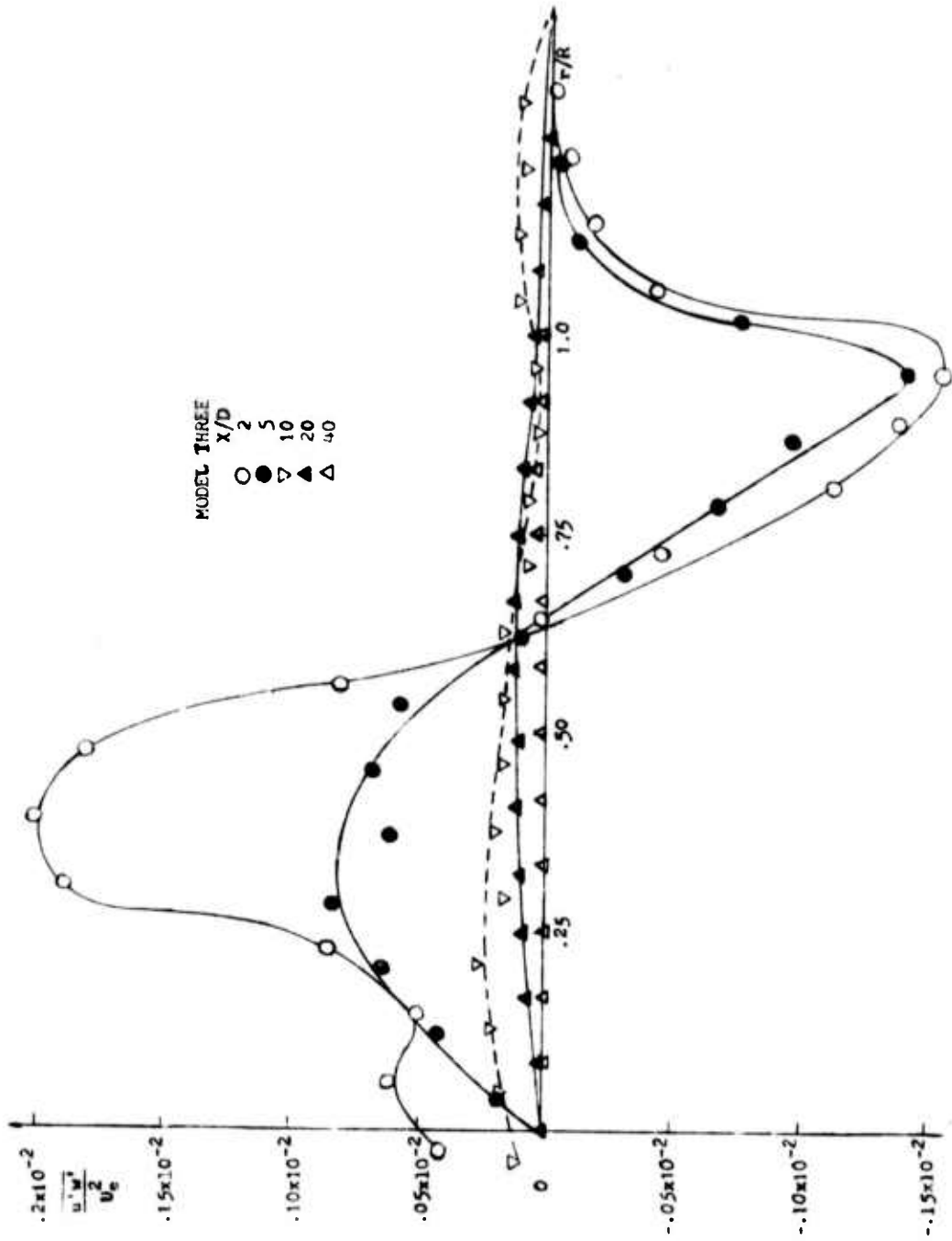


FIG. 34 TANGENTIAL SHEAR STRESS PROFILES FOR MODEL III

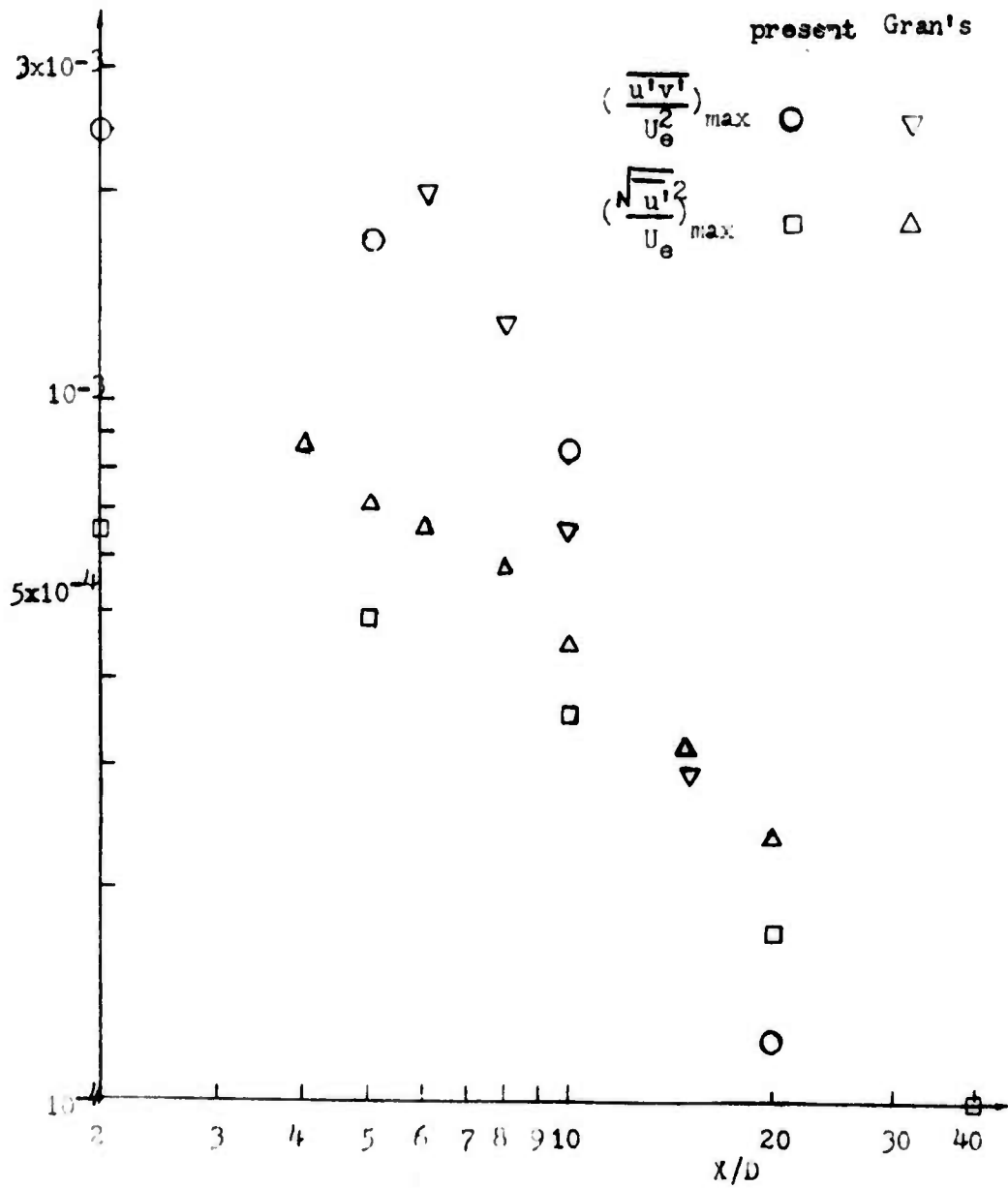


FIG. 35 COMPARISON OF THE RESULTS FOR MODEL III AND GRAN'S MODEL

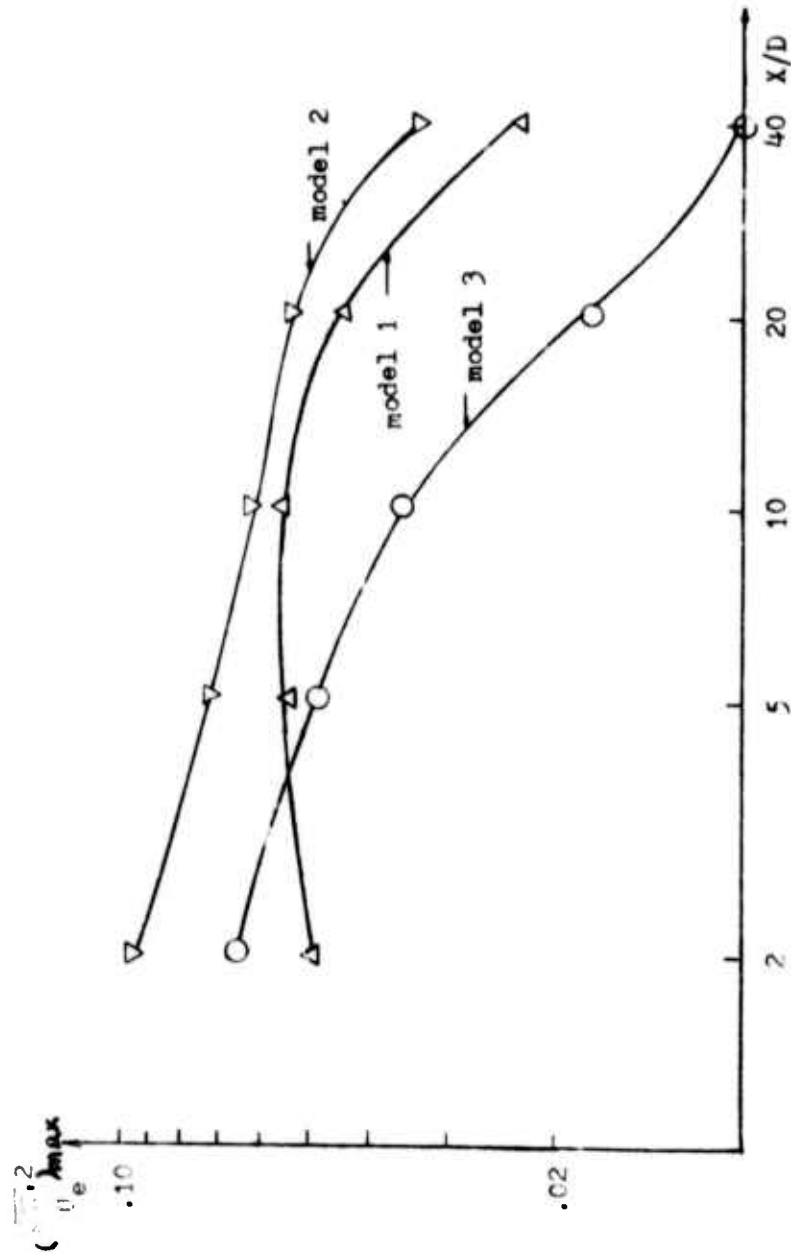


FIG. 36 COMPARISON OF $(\frac{u_e^2}{U_e^2})_{\max}$ FOR MODEL I, II AND III

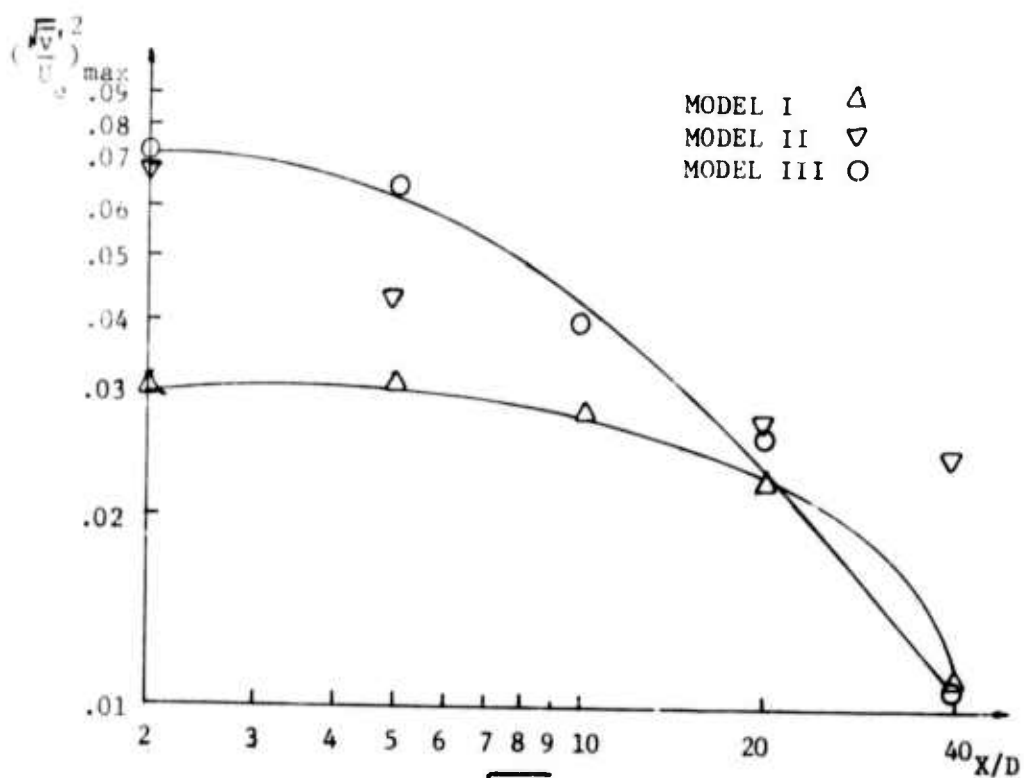


FIG. 37 COMPARISON OF $(\sqrt{v'^2}/U_e)_{\max}$ FOR MODEL I, II AND III

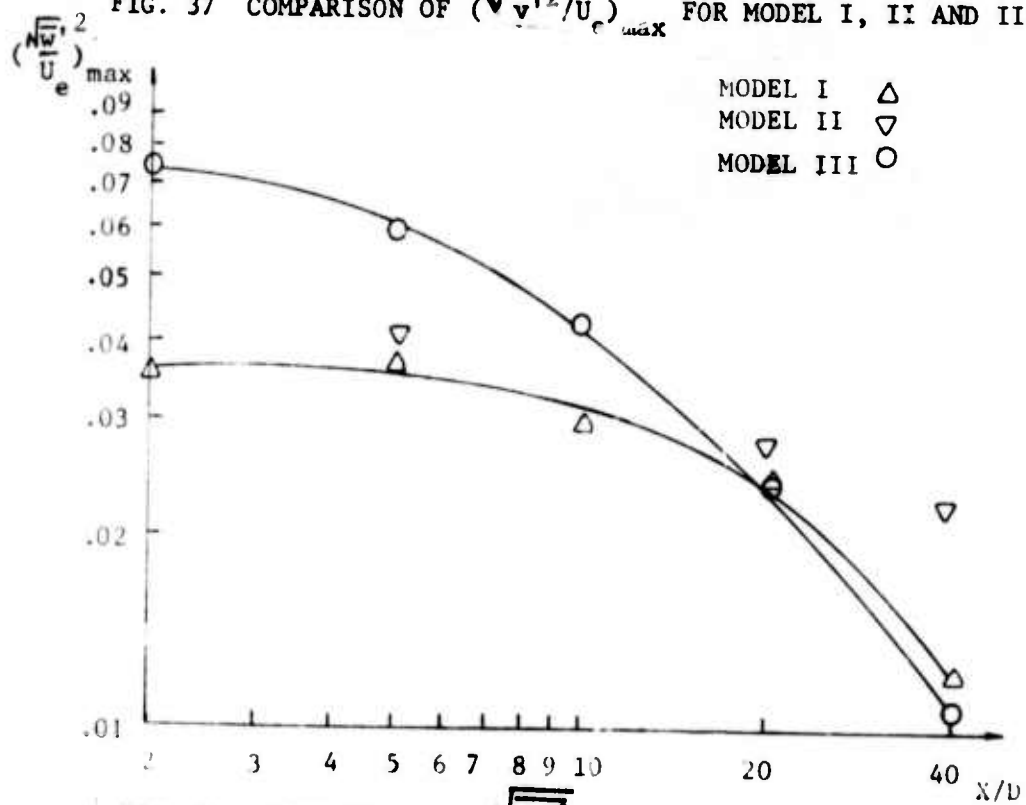


FIG. 38 COMPARISON OF $(\sqrt{w'^2}/U_e)_{\max}$ FOR MODEL I, II AND III

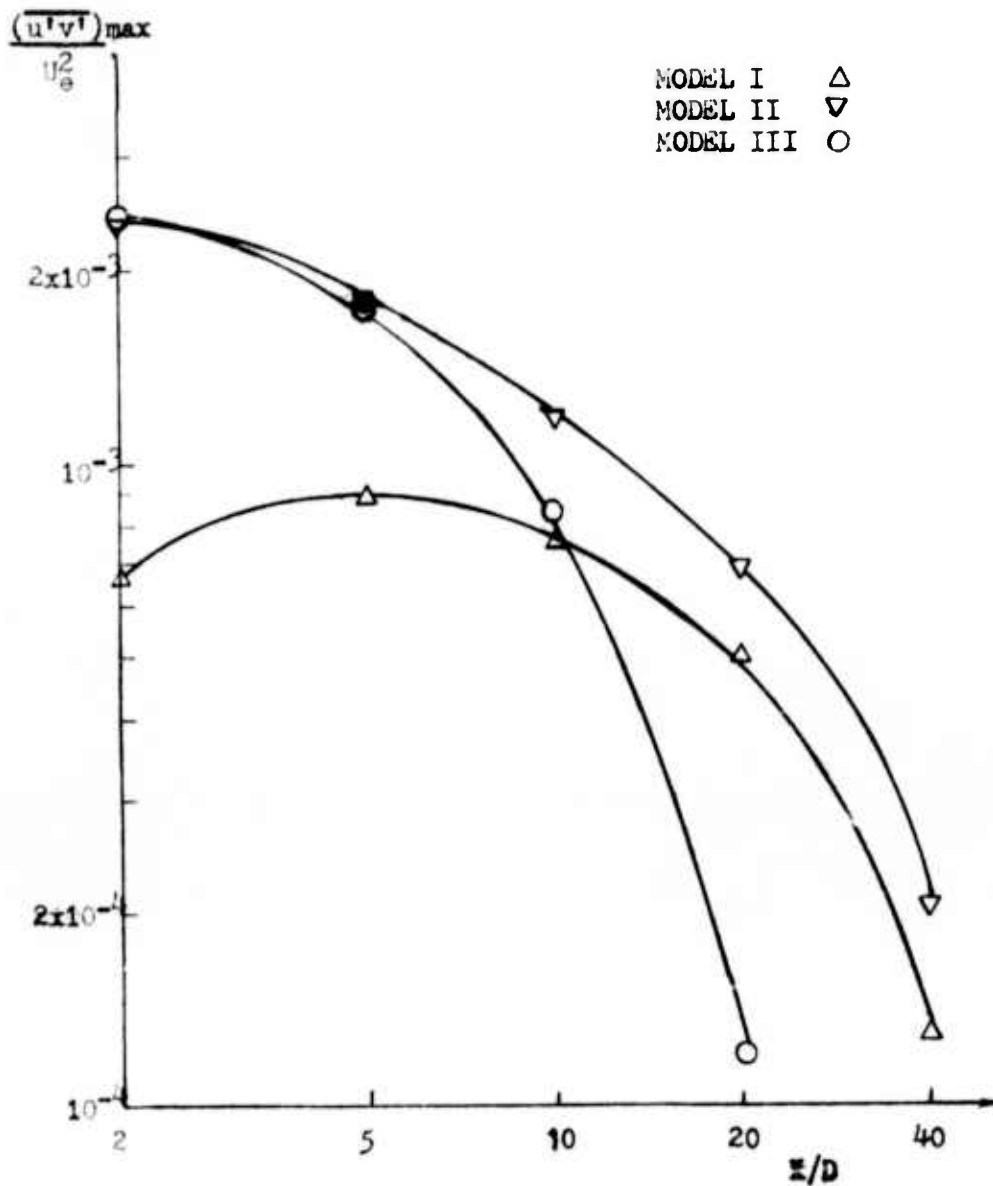


FIG. 39 COMPARISON OF $\frac{(\overline{u'v'})_{\max}}{U_e^2}$ FOR MODEL I, II AND III

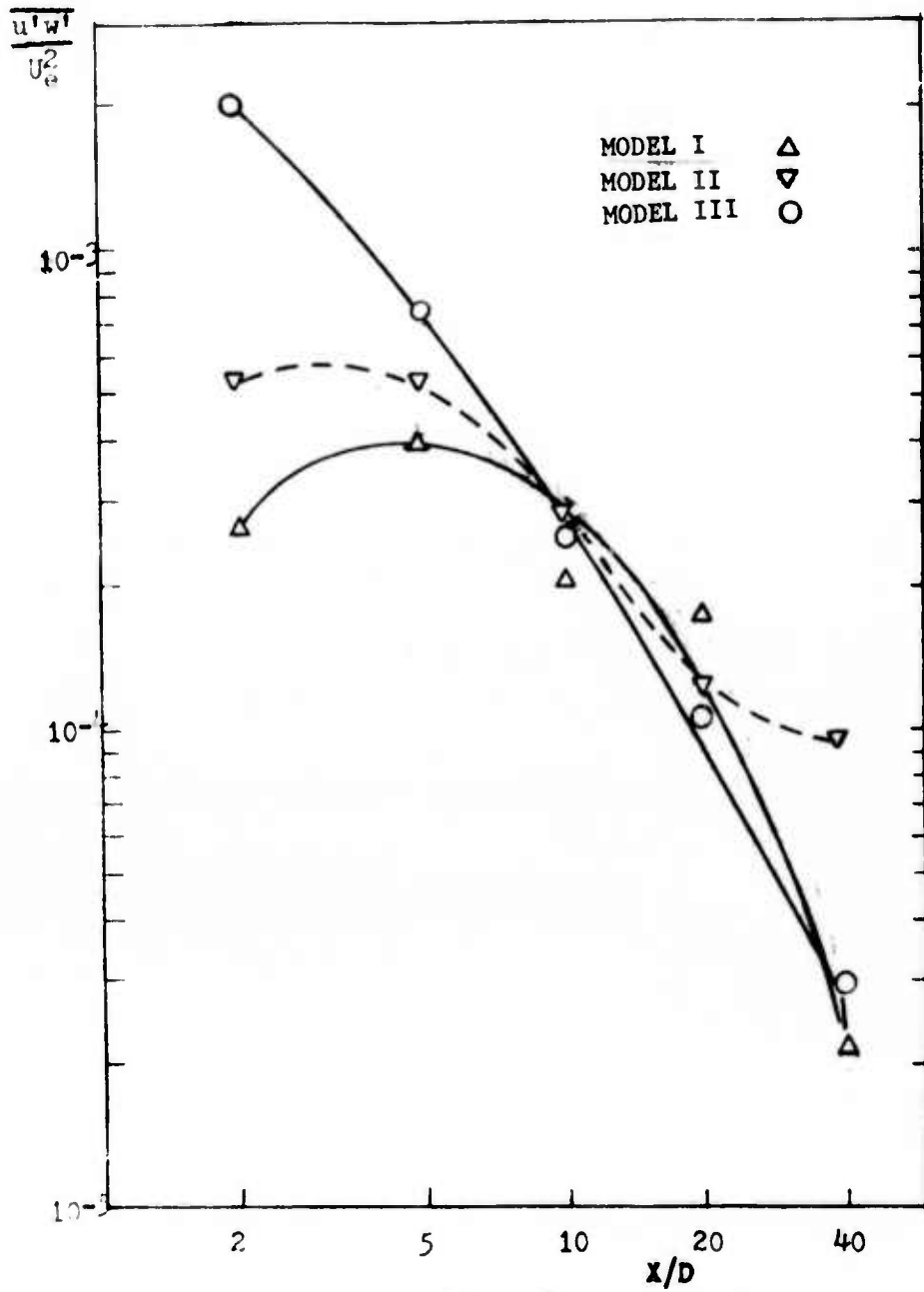


FIG. 40 COMPARISON OF $\frac{u'w'}{U_e^2}$ FOR MODEL I, II AND III

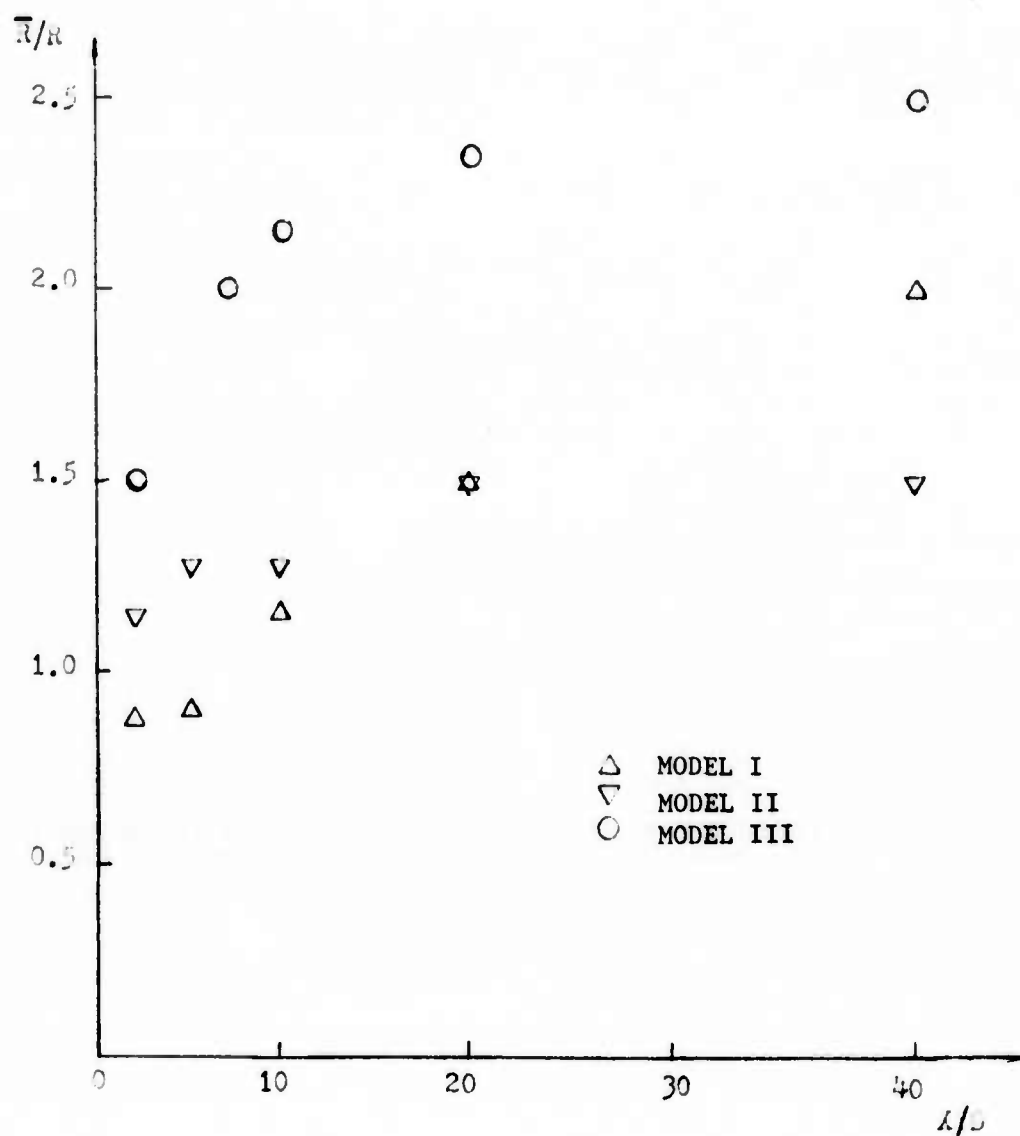


FIG. 41 WAKE WIDTH

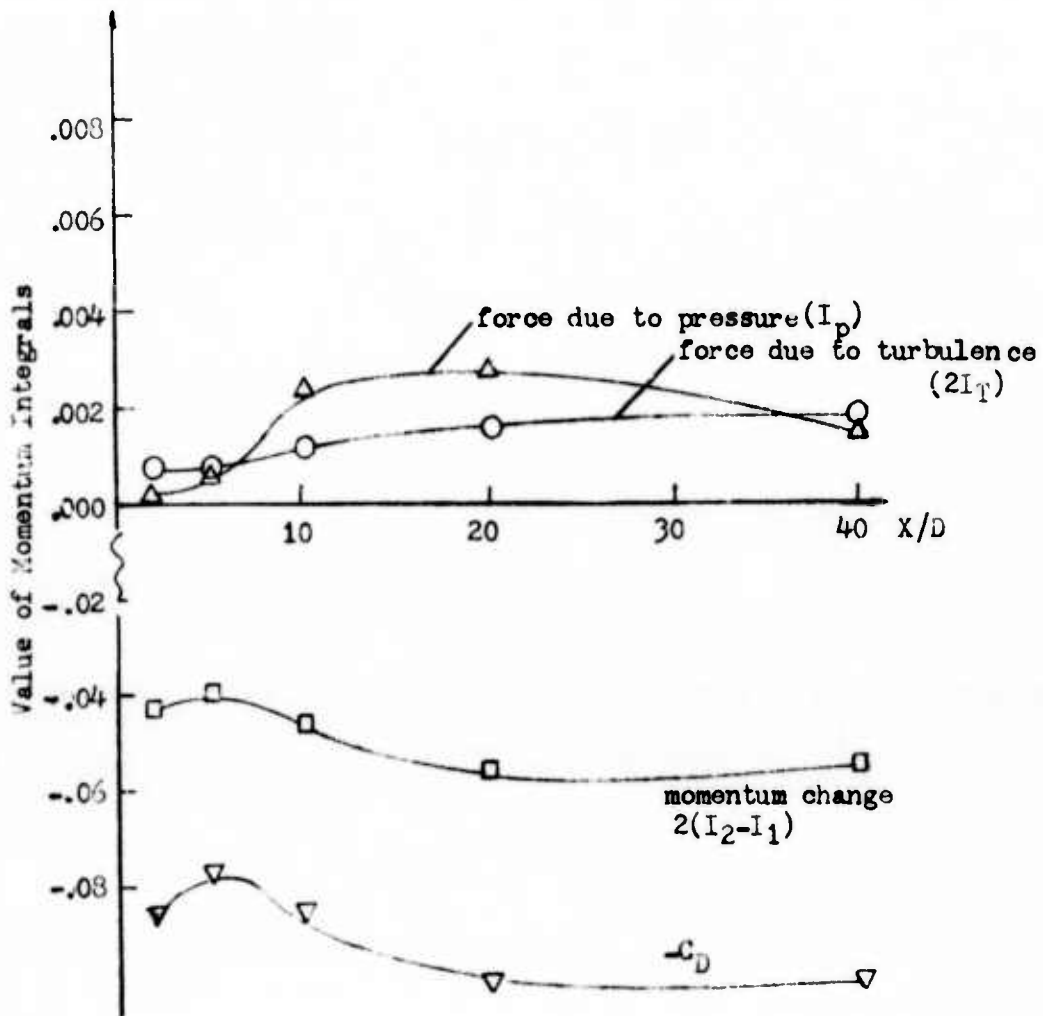


FIG. 42 MOMENTUM INTEGRALS (MODEL I)

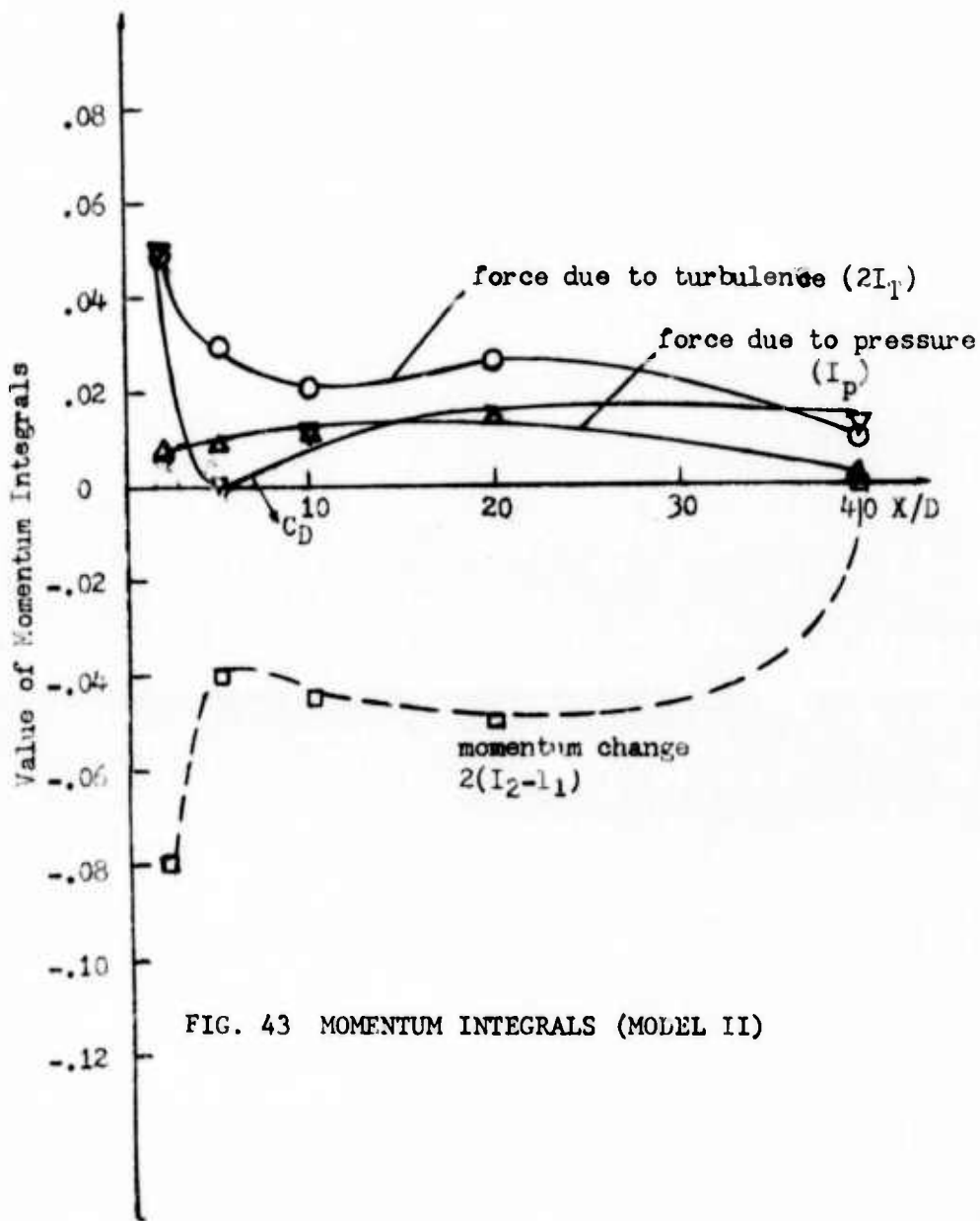


FIG. 43 MOMENTUM INTEGRALS (MODEL II)

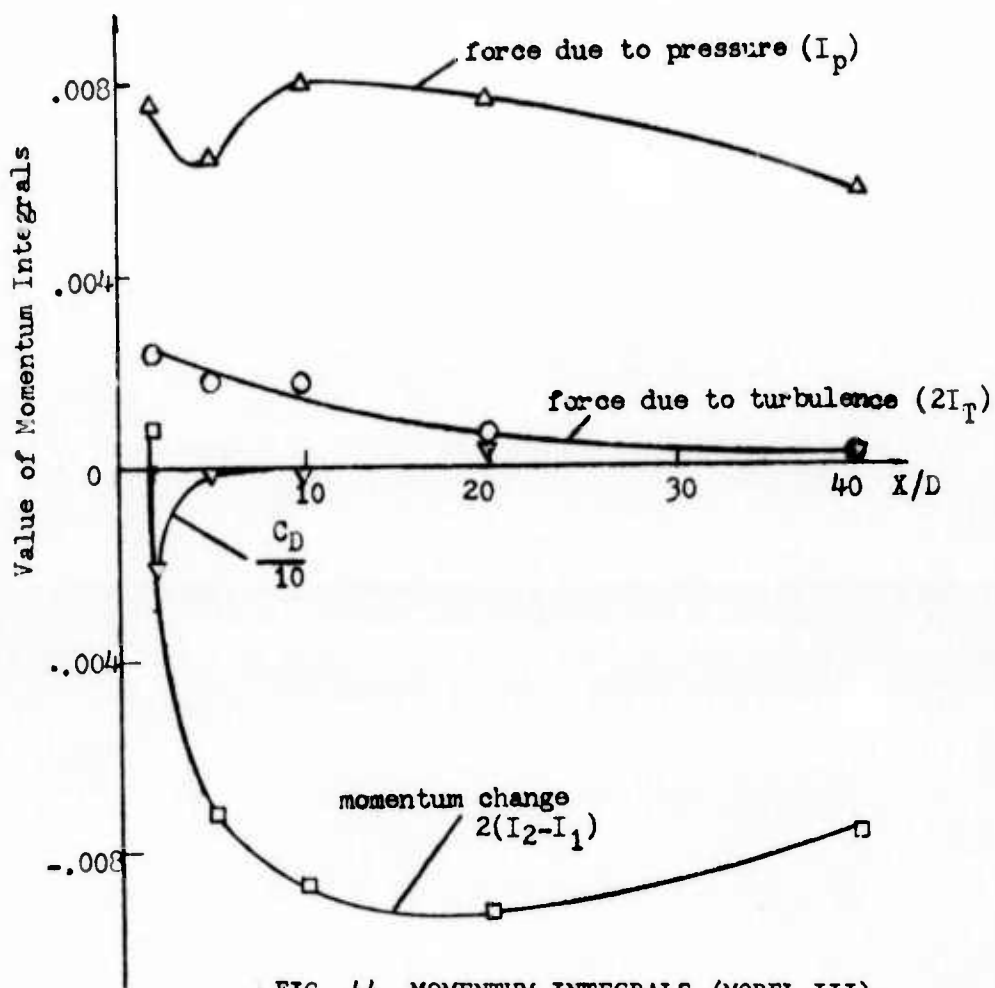


FIG. 44 MOMENTUM INTEGRALS (MODEL III)

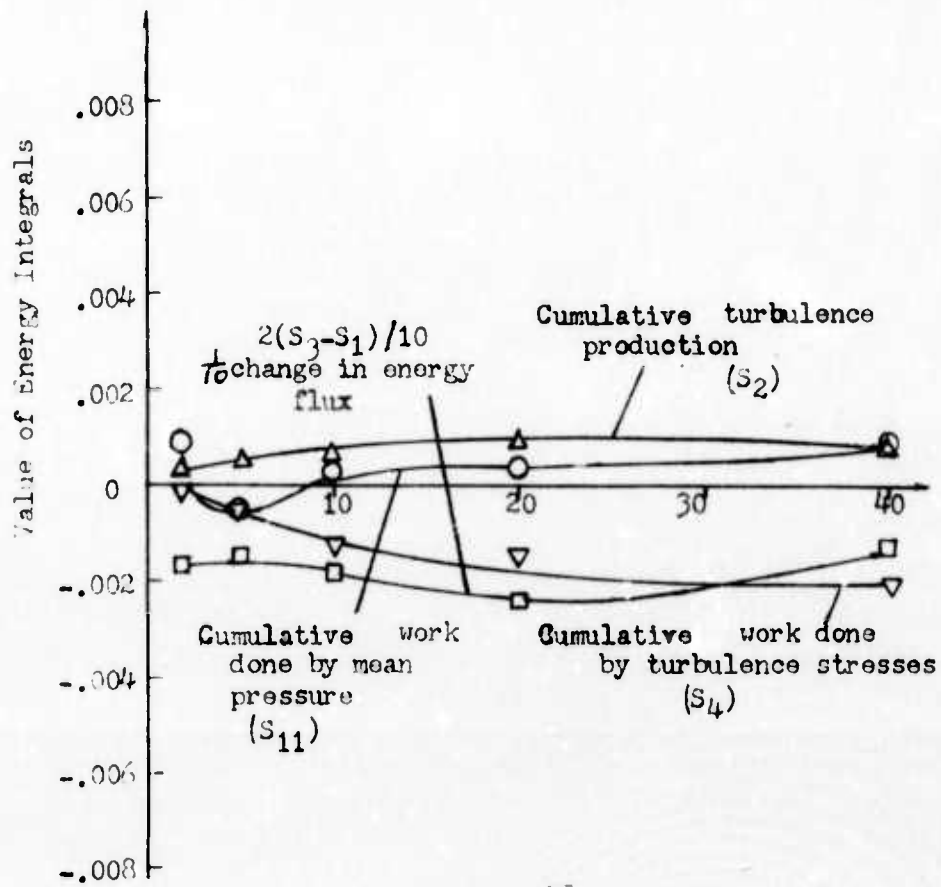
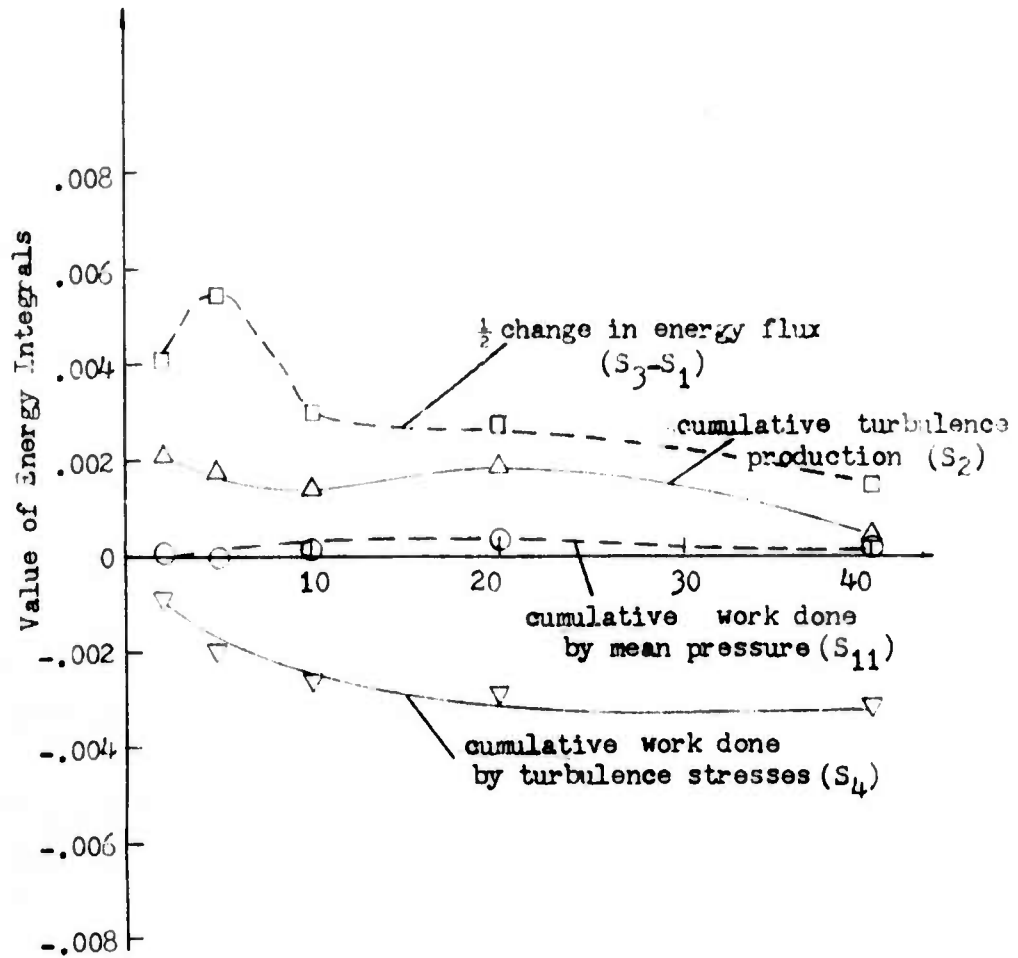


FIG. 45 ENERGY INTEGRALS (MODEL I)



1 FIG. 46 ENERGY INTEGRALS (MODEL II)

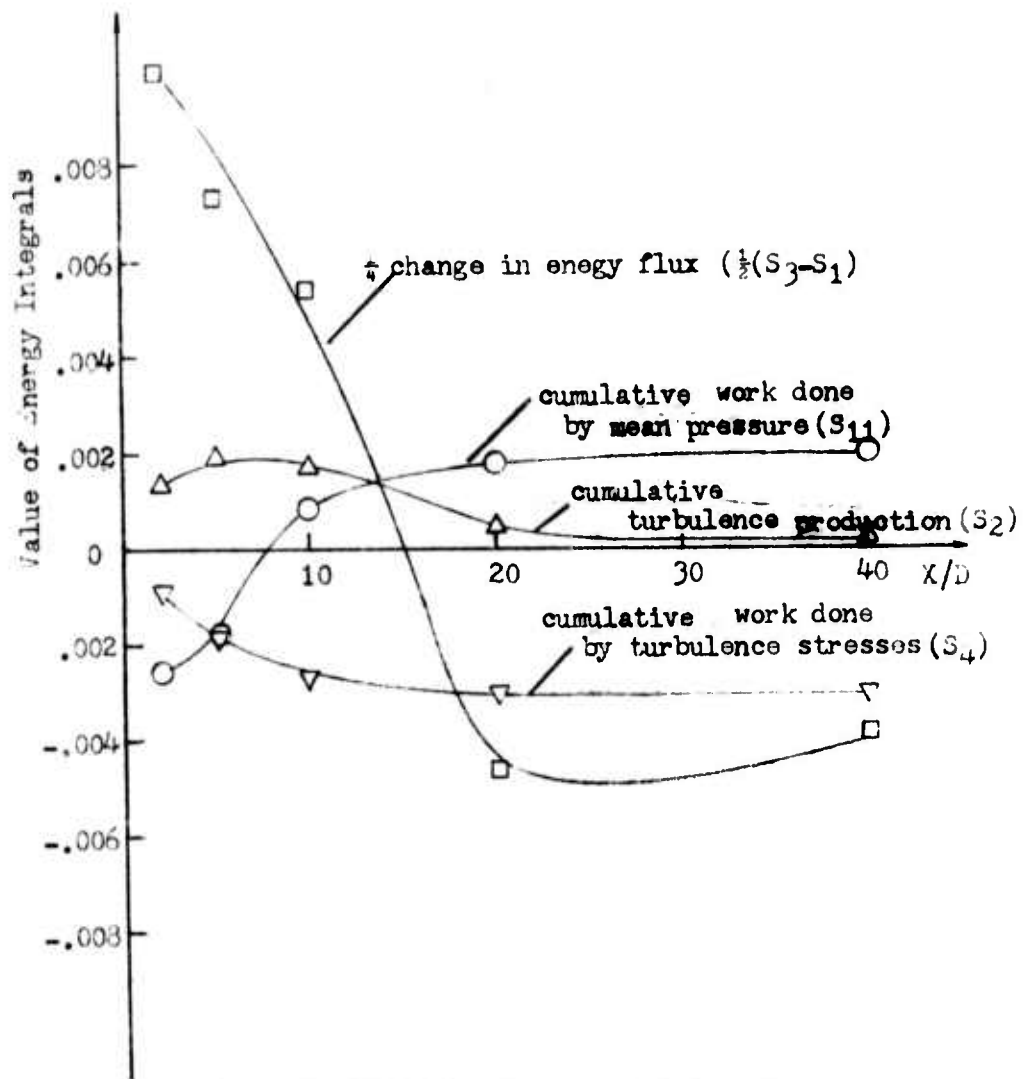


FIG. 47 ENERGY INTEGRALS (MODEL III)